Improving Hall Thruster Plume Simulation through Refined Characterization of Near-field Plasma Properties

by

Tyler D. Huismann

A dissertation submitted in partial fulfillment
of the requirements for the degree of
Doctor of Philosophy
(Aerospace Science)
in The University of Michigan
2011

Doctoral Committee:

Professor Iain D. Boyd, Chair
Professor Alec D. Gallimore
Professor Kenneth Powell
Assistant Professor Alexander G.R. Thomas

To every suchlike wayfarer: *quamdiu inquietum est cor nostrum?*

ACKNOWLEDGEMENTS

First and foremost, thanks to my advisor, Iain Boyd. You gave the right guidance at the right time, in the right way, with the right intent. This is the paradigm for advising graduate students. What can be said after saying that? I loved my time at Michigan, in large part because I much enjoyed working with you. Special thanks also goes to the funding sources that enabled this work, namely the Air Force Office of Scientific Research, and the Air Force Research Laboratory through the Michigan/AFRL Center of Excellence in Electric Propulsion (MACEEP).

Next, I'd like to thank my friends and colleagues, both in Ann Arbor proper and afar, too many to name. I have been so fortunate to know you all: your sound advice and good spirit made getting through it all a lot of fun, whether it was in studying for prelims, starting thought-provoking conversations, or applying collision dynamics at the bowling alley. I'll always remember Ann Arbor because it's where I had such wonderful friends. And I'm sure that you've given me more than I've returned, for which I'll always be thankful.

Finally, I thank my family. My parents have always been supportive and insisted that, among other things, I love my work. I listen to them more than they realize. My brother is always kind and will always talk sports when I want to. My sister gave me a reason to go to the Ann Arbor Hands-On museum, which is awesome. And, most importantly, my wife, Darcy. The other *sine qua non* of who I am today. Now, as ever, thank you.

TABLE OF CONTENTS

LIST OF FIGURES

Figure

LIST OF TABLES

Table

ABSTRACT

Improving Hall Thruster Plume Simulation through Refined Characterization of Near-field Plasma Properties

by

Tyler D. Huismann

Chair: Iain D. Boyd

Due to the rapidly expanding role of electric propulsion (EP) devices, it is important to evaluate their integration with other spacecraft systems. Specifically, EP device plumes can play a major role in spacecraft integration, and as such, accurate characterization of plume structure bears on mission success. This dissertation addresses issues related to accurate prediction of plume structure in a particular type of EP device, a Hall thruster. This is done in two ways: first, by coupling current plume simulation models with current models that simulate a Hall thruster's internal plasma behavior; second, by improving plume simulation models and thereby increasing physical fidelity. These methods are assessed by comparing simulated results to experimental measurements. Assessment indicates the two methods improve plume modeling capabilities significantly: using far-field ion current density as a metric, these approaches used in conjunction improve agreement with measurements by a factor of 2.5, as compared to previous methods.

Based on comparison to experimental measurements, recent computational work on discharge chamber modeling has been largely successful in predicting properties

of internal thruster plasmas. This model can provide detailed information on plasma properties at a variety of locations. Frequently, experimental data is not available at many locations that are of interest regarding computational models. Excepting the presence of experimental data, there are limited alternatives for scientifically determining plasma properties that are necessary as inputs into plume simulations. Therefore, this dissertation focuses on coupling current models that simulate internal thruster plasma behavior with plume simulation models.

Further, recent experimental work on atom-ion interactions has provided a better understanding of particle collisions within plasmas. This experimental work is used to update collision models in a current plume simulation code. Previous versions of the code assume an unknown dependence between particles' pre-collision velocities and post-collision scattering angles. This dissertation focuses on updating several of these types of collisions by assuming a curve fit based on the measurements of atom-ion interactions, such that previously unknown angular dependences are well-characterized.

CHAPTER I

Introduction

This chapter will serve three purposes: 1) to provide motivation and background for the problem under consideration; 2) to summarize the objectives of this dissertation; and 3) to provide an overall outline of the organization of this dissertation.

1.1 Motivation and Background

1.1.1 Motivation

Electric propulsion (EP) systems primarily use electric power to produce thrust, as opposed to traditional chemical-based propulsion systems. Due to their higher overall specific impulse (I_{sp}), EP systems play a crucial role in missions with restricted payload requirements. Despite their low thrust densities when compared to chemical systems, EP technology has been improved to the point that recent missions, such as SMART-1 and DAWN, are able to utilize EP devices as primary propulsion systems [1, 2]. Due to their rapidly expanding role, EP devices in general, and Hall thrusters in particular, must be better understood and characterized so that their application is sound. This is usually achieved through both ground-based experimental diagnostics and numerical simulation. The present work utilizes a recent numerical approach, the so-called hybrid modeling method, to characterize Hall thruster exhaust plumes. This numerical method has been shown to be an effective tool for understanding

these plumes. Additionally, experimental data is used to assess the information that numerical simulation supplies, resulting in a better understanding of exhaust plume structure.

The exhaust plume of a typical EP device is important because of spacecraft integration concerns. For example, the plume of a typical EP device can interact with sensitive spacecraft systems. High-energy ions with large plume divergence angles or back-flowing charge-exchange (CEX) ions can potentially impinge on various spacecraft surfaces, sputtering material away from where it is needed and depositing material where it is unwanted. Additionally, due to their lower thrust densities as compared to traditional chemical-based devices, EP devices frequently must operate for longer durations than chemical systems, increasing the likelihood of accumulated impingement effects. Scientific instrumentation, solar panels, and communications systems can all be impaired due to impingement. Impairment of these systems could lead to subsystem or even complete mission failure; therefore, EP plumes must be thoroughly understood.

Numerically modeling Hall thruster plumes can yield information that is significant to these issues. Numerical modeling can give qualitative information about a broader domain of investigation than experimental measurements can provide, as well as provide quantitative information about fluxes of high-energy and CEX ions. Numerical modeling also clarifies the otherwise complex physical situation typical of EP devices by providing computational predictions of plasma regions that might not be amenable to experimental diagnostics.

1.1.2 Background

1.1.2.1 General Theoretical Background

Spacecraft propulsion in general is based on Newton's Third Law of motion, which can be expressed as:

$$m\frac{dV}{dt} = \dot{m}U_e \tag{1.1}$$

where the left hand side of Eqn. (1.1) represents the spacecraft acceleration and the right hand side represents propellant thrust. Replacing $\dot{m}$ by $\frac{dm}{dt}$ and integrating results in the classical rocket equation for a single stage spacecraft:

$$\frac{m_f}{m_o} = e^{-\frac{\Delta V}{U_e}} \tag{1.2}$$

where the left hand side is the final non-propellant mass fraction of the spacecraft and ΔV represents the mission velocity requirement. Eqn. (1.2) characterizes the relationship between the mission velocity requirement, the mass of the propellant necessary to achieve this velocity, and the performance of the propulsive device. This relationship can be understood thusly: given a constant mission velocity requirement, more efficient propulsion devices will require less mass, and so their $\frac{m_f}{m_o}$ ratio will be closer to unity. Therefore, more efficient devices are described as having a higher exit velocity (U_e).

In order to compare various engine types, exit velocity is typically normalized by the propellant weight flow rate, with the resultant quantity being the specific impulse (I_{sp}) of the device, measured in seconds:

$$I_{sp} = \frac{U_e}{\dot{m}g_o} \tag{1.3}$$

Note that g_o is the gravitational acceleration constant at the Earth's surface, 9.81 $\frac{m}{s^2}$. Specific impulse is a useful metric for comparing engine efficiency for two reasons: first, it is directly proportional to exit velocity, which was shown to relate directly to propulsive efficiency above; second, it allows for direct comparison of engine performance since some differences in performance due to propellant choice are filtered out via normalization.

1.1.2.2 Electric Propulsion Taxonomy

EP devices can be categorized into three principal types: electrothermal, electrostatic, and electromagnetic [3]. Although EP devices all utilize electrical power as their primary energy source, each type of EP device is differentiated via the mechanism used in order to accelerate the exhaust flow:

1. Electrothermal devices. These devices use electric current or electromagnetic radiation to heat the propellant. The resulting thermal energy is converted to directed kinetic energy by expansion through a nozzle. Resistojets and arcjets are both examples of electrothermal devices. Figure 1.1 illustrates the operation of a typical arcjet.

2. Electrostatic devices. These devices accelerate charge-carrying propellant particles (atoms or a molecules) in a static electric field. These devices typically use a static magnetic field that is strong enough to magnetize electrons while sufficiently weak so that ions are not magnetized. Ion engines and Hall thrusters are examples of electrostatic devices. Figure 1.2 illustrates the operation of a typical Hall thruster.

3. Electromagnetic devices. These devices accelerate charge-carrying propellant particles in interacting electric and magnetic fields. The magnetic field strength in these devices is typically high enough to significantly affect both electron and ion trajectories. Pulsed plasma thrusters (PPT) and magnetohydrodynamic thrusters are both examples of electromagnetic devices. Figure 1.3 illustrates the operation of a PPT.

1.1.2.3 Hall Thrusters and Hall Thruster Taxonomy

Hall thrusters originated in the 1950's and 1960's in both the United States and the former Soviet Union. After the first operational use of Hall thrusters by the

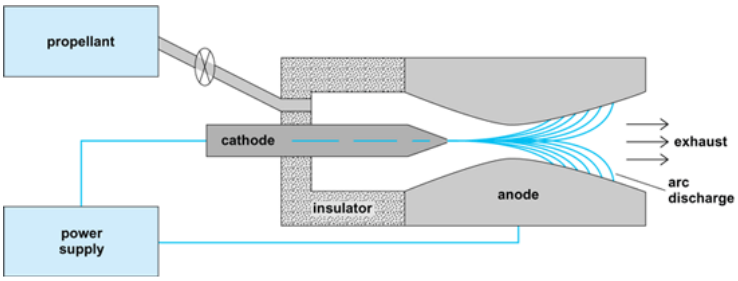

Figure 1.1: Schematic of an arcjet thruster, a type of electrothermal propulsion system. Figure from Ref. [4].

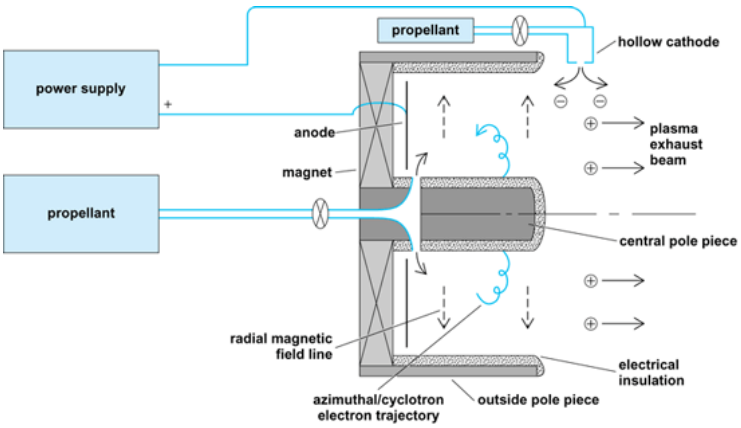

Figure 1.2: Schematic of a Hall thruster, a type of electrostatic propulsion system. Figure from Ref. [4].

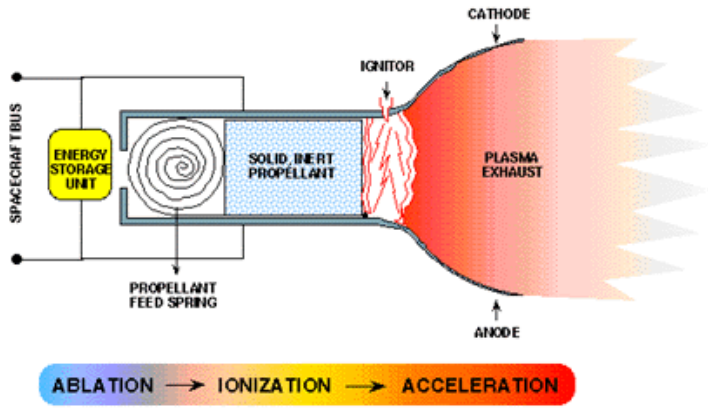

Figure 1.3: Schematic of a pulsed plasma thruster, a type of electromagnetic propulsion system. Figure from Ref. [5].

USSR, over 100 thrusters have been flown on satellites [6]. Figure 1.2 exhibits the typical axisymmetric shape of Hall thrusters: the acceleration channel is an extended annulus with an anode at one end and a cathode at the other. A neutral propellant is normally injected at or near the anode. The propellant is then ionized, forming a plasma, and accelerated out of the chamber via an electric field. Xenon is typically used as the propellant of choice, due to both its high molecular weight and its low ionization potential. At the opposite end of the acceleration channel, a cathode emits electrons into the flow of propellant. A portion of these electrons ensures the quasi-neutrality of the flow, while the rest of the electrons travel upstream toward the anode. Most of the ionization of neutrals occurs in a high-magnetic field region near the exit of the acceleration channel: here, the magnetic field traps electrons, impeding their axial drift. The magnetic field design is the distinguishing characteristic of Hall thrusters. It is designed to be a radial field that is strong enough to trap electrons, but sufficiently weak to leave ions unmagnetized. The electrons which are caught in the magnetic field move in the azimuthal direction, forming a Hall current, from which the thruster gets its name.

There are two main types of Hall thrusters: stationary plasma thrusters (SPT) and thrusters with anode layers (TAL) [7]. In the SPT, the walls of the acceleration channel are made of insulative materials, such as boron nitride or silicon carbide. The walls are therefore non-conductive dielectrics, thus charge builds up along the length of the acceleration channel walls. Here, the acceleration channel is relatively long, on the order of centimeters. Figure 1.4 shows the SPT Hall thruster that is the focus of this study. This particular thruster has a discharge power of about 6 kW and possesses a cathode that is mounted along the thruster centerline, resulting in a completely axisymmetric flow.

A TAL has a similar structure save for the material that makes up the acceleration channel walls: the walls are metallic (e.g. stainless steel) and therefore conductive.

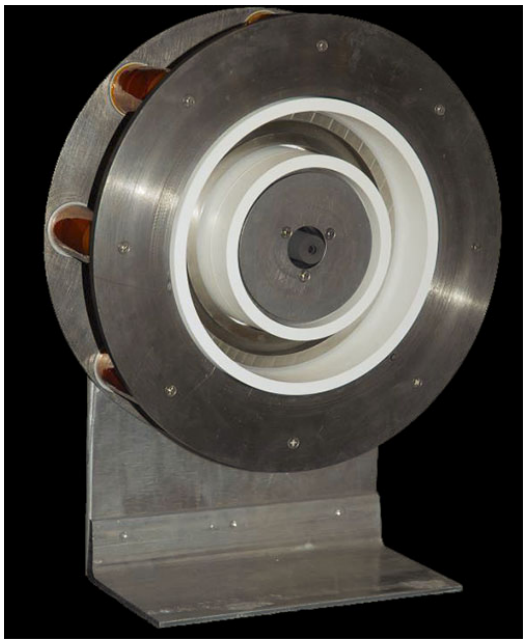

Figure 1.4: A 6 kW SPT Hall thruster. Photograph courtesy of the Plasmadynamics and Electric Propulsion Laboratory (PEPL) at the University of Michigan.

Due to this conductivity, a constant potential is observed along the entire wall of the acceleration channel. High electron temperatures are typically observed in a TAL ($>$ 20 eV). The total length of the acceleration channel is comparatively shorter in TAL Hall thrusters than in SPT Hall thrusters, on the order of millimeters. Figure 1.5 shows an example of a TAL, the D55 thruster.

1.1.2.4 Plume Characterization via Experimental Methods

The importance of understanding and characterizing the plumes of EP devices was covered in 1.1.1, thus the next two sections will discuss methods associated with this process. Experimental testing of EP devices is normally conducted in ground-based vacuum facilities. The majority of the experimental data presented in this study were acquired by the Plasmadynamics and Electric Propulsion Lab (PEPL) at the University of Michigan [8, 9, 10], with some data courtesy of the NASA Jet Propulsion Laboratory (JPL) [11].

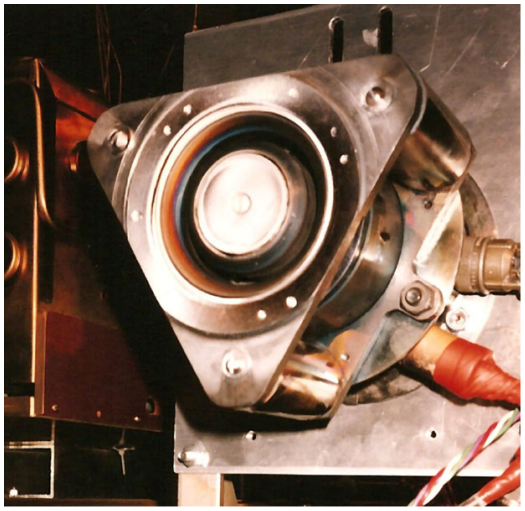

Figure 1.5: The D55 TAL Hall thruster. Photograph courtesy of the PEPL.

The vacuum facility in which the PEPL data were acquired is the Large Vacuum Test Facility (LVTF), the largest such facility at PEPL and one of the largest academic facilities in the US. The main part of the LVTF is a cylindrical chamber, 9 m long and 6 m in diameter. Figure 1.6 is a diagram of the facility, including various instrumentation, that illustrates the complexity of the chamber. The LVTF has a large pumping rate, on the order of 240,000 L/s for xenon. The effectiveness of this pumping rate is quantified by the measurable pressure due to background gas during thruster operation: for the experimental data presented here, the facility back-pressure is on the order of 1×10^{-3} Pa. The presence of this background gas complicates both experimental measurement and numerical prediction of the thruster plume. In the acceleration chamber, background gases can be reingested and accelerated, altering measurements of thruster efficiency. The background gas can also interact with accelerated particles in the plume, producing low-energy CEX ions. This can potentially affect measurements of current density, velocity distribution, and beam divergence.

The vacuum facility in which the JPL data were acquired is the Hall Thruster Test Facility, or the so-called "Patio chamber." The main part of the Patio chamber is a cylindrical chamber, 12 m long and 3 m in diameter. Figure 1.7 is a photograph

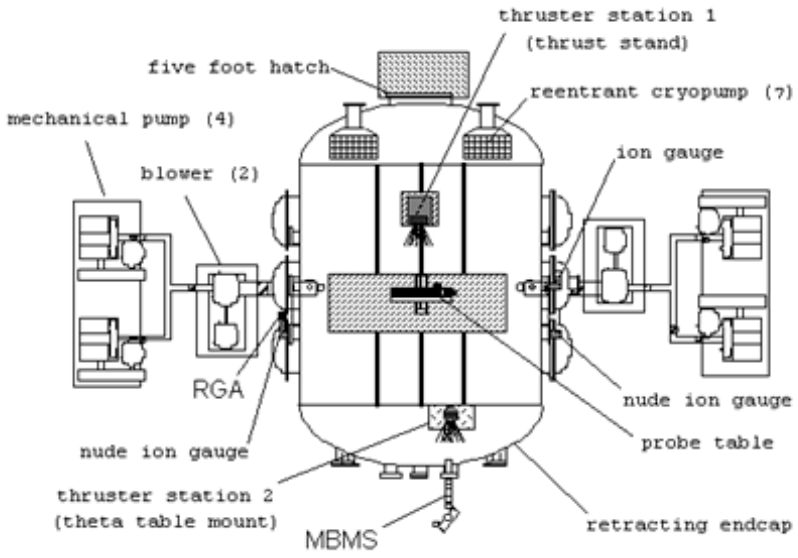

Figure 1.6: The LVTF. Schematic courtesy of the PEPL.

of the facility. The Patio chamber has a large pumping rate, on the order of 200,000 L/s for xenon, resulting in a back-pressure on the order of 2×10^{-3} Pa.

This study will be making comparisons to data acquired using four diagnostic methods: Faraday probes, Langmuir probes, floating emissive probes, and laser-induced fluorescence (LIF) velocimetry. Characterization of the experimental apparatus is based on Refs. [8, 9, 10, 11]; further details can be found therein. Note that all experimental data are considered time-averaged.

The first method of data acquisition utilized Faraday probes. Faraday probes are the simplest form of data acquisition, primarily consisting of a current collecting surface that is large relative to the local Debye length. The probes referenced in this study were voltage-biased in order to repel electrons so that the probes measure only the local ion current density. Faraday probes commonly employ guard-rings around the collecting surface to reduce edge effects that could artificially increase measured data. The experimental data reported in this study were acquired using two different Faraday probe designs: a 23.1 mm diameter tungsten-coated aluminum disk with a guard-ring was used to make far-field plume measurements of current density, while a

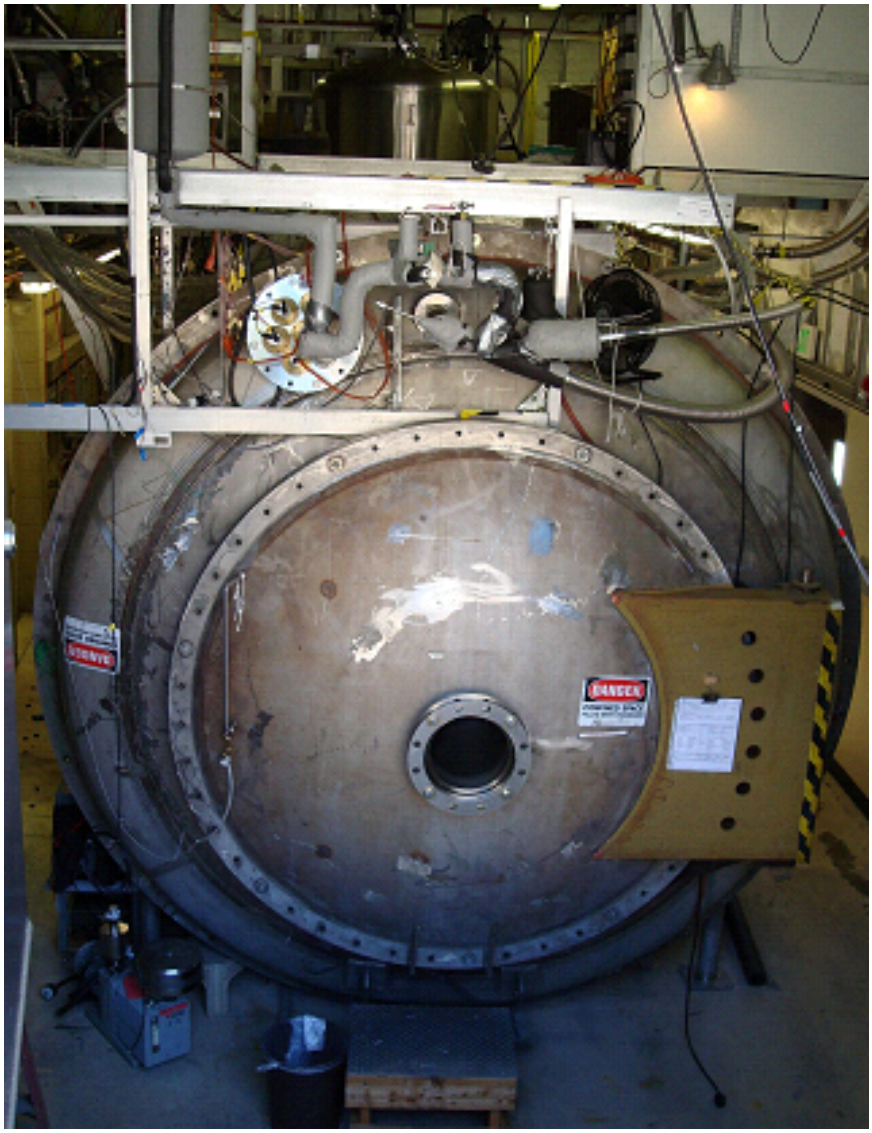

Figure 1.7: The Hall thruster test facility. Photograph courtesy of the JPL.

4.85 mm diameter molybdenum disk without a guard-ring was used to make near-field plume measurements. The uncertainty in the measurements taken with the far-field probe is due mainly to facility-induced CEX collisions redistributing main beam ions, and is conservatively estimated at $+0/-50\%$ on the integrated beam current [8]. The uncertainty in the measurements taken with the near-field probe is due mainly to probe area definition: the near-field probe lacked a guard-ring due to fabrication constraints. The uncertainty is therefore estimated at $\pm 10\%$ on the integrated beam current [8].

The second method of data acquisition utilized Langmuir probes. Langmuir probes are widely used in Hall thruster experimental testing due to their robustness: this single acquisition technique can measure a comprehensive set of plasma properties [8]. Langmuir probes typically consist of a single electrode which is exposed to plasma and subjected to a range of applied potentials. The plasma's response to these voltages is used to determine I-V characteristics that can be used to extract properties such as ion number density, floating plasma potential, and electron temperature. The internal plasma measurements reported in this study were acquired using a Langmuir probe with a 0.25 mm diameter tungsten wire tip. This tip is encased in a 1.5 mm diameter, double-bore alumina tube which is itself telescoped inside a 6.4 mm diameter alumina tube. A boron nitride shroud covered the portion of the probe that entered the acceleration channel so that the probe could withstand the heat loads of the thruster's internal plasma. Near-field plasma potential measurements are also reported in the present study: these measurements are courtesy of JPL, and were acquired using an emissive probe, outlined below. The uncertainty in internal plasma measurements is due to several factors, including time resolution and probe tip effects, and is conservatively estimated at $\pm 1V$ and plus $2-300\%$ on the derived number density. The source of the uncertainty on the number density measurements is as yet undetermined [8], though this type of number density measurement is typically

characterized by an uncertainty near ±50%. Uncertainty in electron temperatures derived from internal Langmuir probe data is not reported.

The third method of data acquisition utilized floating emissive probes. Historically, floating emissive probes have been primarily used to measure plasma potential [12, 13, 14]. Floating emissive probes utilize high-temperature filaments in order to produce thermionic emission of electrons. At low emission currents, the probe potential is low compared to the local plasma potential, and electrons escape into the local plasma, acting as an effective ion current. At higher emission currents, the probe potential is higher than the local plasma potential, and so emitted electrons are reflected back to the probe. In between these emission currents is a critical emission current at which the probe potential is the same as the local plasma potential, i.e. it is "floating" at the local potential. The experimental data reported in this study that were acquired at PEPL were obtained using a floating emissive probe with a 1.5 mm diameter, double-bore alumina tube which is itself telescoped inside a 6.4 mm diameter alumina tube, similar to the Langmuir probe. The filament loop was composed of a 0.127 mm diameter thoriated tungsten wire bent to a radius of curvature of 0.5 mm. The assembly is capped with a graduated boron nitride shroud. The experimental data reported in this study that were acquired at JPL were obtained using a floating emissive probe with two 1.6 mm diameter alumina tubes. The filament loop was composed of a 0.127 mm diameter tungsten wire. The uncertainty in measurements taken with either floating emissive probe is due primarily to space-charge limitations: space-charge limited emission leads to double sheath formation such that some electrons are reflected back by the potential well of the double sheath, not the local plasma. This is alleviated by utilizing electron temperature measurements to correct the probe measurements. The total uncertainty for the PEPL emissive prove is composed of a probe uncertainty of $\pm 5V$, plus an uncertainty in the correction method of $\pm 0.9\ T_e$, whereas the JPL emissive probe is reported to have an uncertainty of $\pm 1V$.

The fourth method of data acquisition that was used is LIF velocimetry [9, 10]. LIF operates on the principle that when a particle absorbs a photon, it will de-excite and emit another photon. Excited particles will de-excite through collision, spontaneous emission, or stimulated emission. Particles that spontaneously emit photons at the same energy as the absorbed photons are said to undergo resonant emission, whereas particles emitting photons at different energies are said to undergo non-resonant emission. This spontaneous emission, called fluorescence, radiates isotropically away from the particle. Velocimetry through LIF is obtained by way of Doppler shift theory. Non-relativistic particles will shift their absorption frequencies in proportion to the particle velocity component in the direction that the photon travels. By varying the frequency of injected photons and comparing the intensity of collected fluorescence, velocity distribution functions (VDF) a given species can be obtained. The uncertainty in the LIF velocimetry is due mainly to laser linewidth and is conservatively estimated at $\pm 50\ m/s$ or $\pm 2\%$, whichever is greater.

1.1.2.5 Plume Characterization via Computational Methods

Computational modeling provides the opportunity to mitigate the potential problems mentioned in Section 1.1.1 for a relatively low cost. Computational modeling offers a way to improve spacecraft integration by both: *i*) predicting spacecraft operation, as well as *ii*) filtering out issues that arise with ground-based vacuum facilities, e.g. simulating the effects of background gases in such facilities. The potential of computational modeling for isolating physics in this fashion is becoming more valuable with the development of high powered Hall thrusters: these thrusters operate at high mass flow rates which can diminish the effectiveness of vacuum facilities. The value of isolating physical processes is not limited to plume modeling, however. With thruster operational lifetime becoming a more pressing concern, computational modeling offers a way to determine which physical processes dominate operational

lifetime.

There are three types of computational models that are commonly applied to simulate Hall thruster plasmas: the fluid model, the kinetic model, and the hybrid model.

1. Fluid models. Simulations utilizing fluid models assume that both the heavy species (ions and neutral atoms) and the electrons that constitute the plasma that the thruster generates are represented as fluids. This approach is typically very fast, with computational wall-times several orders of magnitude smaller than analogous fully kinetic approaches. Fluid models are also well understood, having been developed by the computational fluid dynamics (CFD) community since the 1940's [15]; as such, they are easily adaptable to 1-D, 2-D, or axisymmetric geometries, as well as both steady and unsteady time-dependent solvers. One weakness of fluid models, however, is the continuum assumption on which their governing equations are based: as determined by their Knudsen number, Hall thruster plume plasmas are very rarely in the continuum regime, and more commonly are either transition flows or rarefied flows.

2. Kinetic models. Simulations utilizing kinetic models assume that both the heavy species and the electrons are represented as particles. Kinetic models have the advantage over fluid models of not assuming the continuum hypothesis, and as such, are better suited to plasmas in the transition or rarefied regimes. Kinetic models are at a significant disadvantage, however, in the amount of computational wall-time required. Since electrons are several orders of magnitude lighter than ions, their motion must be resolved using much smaller timescales, typically on the order of 500 times smaller than the timescales required to resolve ion dynamics alone. As a result, typical simulations utilizing kinetic models have wall-times several orders of magnitude greater than analogous fluid approaches.

3. Hybrid models. Simulations utilizing hybrid models do not assume that both the heavy species and the electrons are characterized in the same way, contrary to fluid and kinetic models. A typical hybrid model will assume that the heavy species are represented as particles while the electrons are represented as a fluid. This method maintains the accuracy of modeling the heavy species kinetically, and as a result, captures rarefied, non-Maxwellian features of the thruster plasma. The hybrid method also trades the more accurate particle modeling of the electrons for a fluid model, avoiding the severe computational cost that is associated with modeling the electrons kinetically. Although the electron population is not strictly a fluid, they behave as a fluid in that they adjust to perturbations quickly, relative to ion motion. Various fluid models are available for modeling the electrons, ranging from the simple Boltzmann relation applied throughout the domain to more sophisticated fluid models based on conservation laws.

The models enumerated above are flexible enough to simulate Hall thruster plasmas from propellant ionization to ejection and evolution into plume structures. The present study examines Hall thruster plasmas in two distinct but overlapping regions: the thruster acceleration chamber and the thruster plume. To examine each of these regions, two different computational models are used: HPHall and MONACO-PIC (MPIC). The domain for each of these models is shown in Figure 1.8. Note that there is a small, semi-circular region of overlap between these domains. In the present study, this region is called the very near-field plume. Though these models and their various submodels are outlined here, they will be more fully described in the subsequent chapter.

HPHall is an axisymmetric hybrid model designed to simulate plasmas internal to Hall thrusters, i.e. plasmas in the acceleration chamber and the very-near field plume, using a structured grid. Due to its exhibited robustness and success, it has

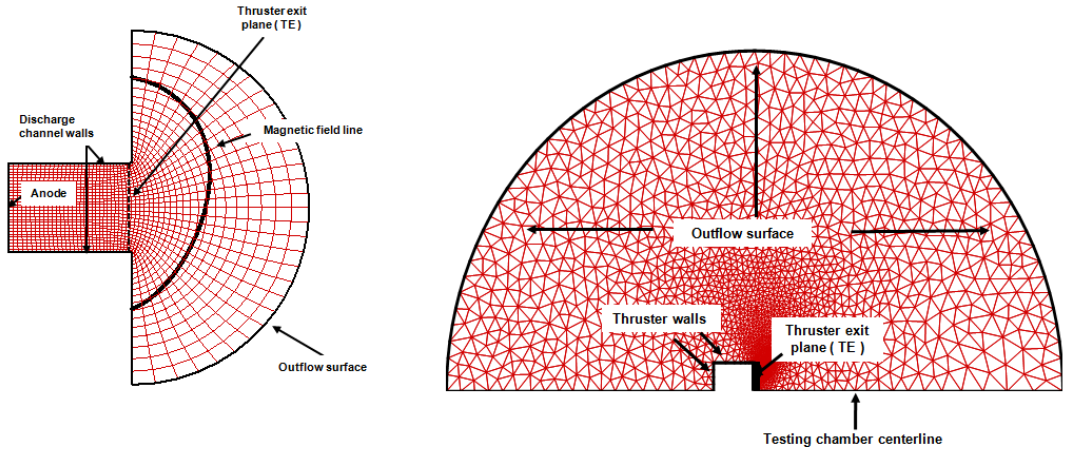

Figure 1.8: Computational domains of HPHall (left) and MPIC (right).

remained at the forefront of Hall thruster computational development, and various groups have since developed similar models [16, 17, 18, 19]. Although two versions of HPHall will be utilized in this study, HPHall2 (H2) and HPHall3 (H3), these versions have a broad, fundamental structure in common. The basic structure of HPHall consists of two submodels, both for the heavy species and for the electrons. The heavy species are modeled as discrete particles, whereas the electrons are modeled as a quasi 1-D fluid. The quasineutrality assumption, $n_i = n_e$, is used in order to link these two submodels. Additionally, the thruster's magnetic field is required as an input. Induced magnetic fields are ignored, and so the initial $\vec{B}$ field is considered static. Finally, several models are available for representing anomalous diffusion [20]. Although the models are not based on first principles, they are refined such that a wide variety of phenomena observed in measurements is captured [20, 21].

MPIC is an axisymmetric hybrid model designed to simulate plasmas external to EP thrusters, including Hall thruster plumes, using an unstructured grid. MPIC has been utilized for many and varied studies relating to Hall thruster plumes, including: investigation of facility effects on plumes and choice of electron fluid model [22, 23]; investigation of plasma-probe interactions [24]; and investigation of numerical plasma diagnostics [25]. Because it is a hybrid model, MPIC is well-suited for capturing the

rarefied features specific of Hall thruster plumes. Similar to HPHall, MPIC utilizes a hybrid method to model Hall thruster plumes, normally from the thruster exit plane to a chosen domain boundary (whether this be an outflow boundary or the walls of a facility). The hybrid model which MPIC utilizes consists of two submodels, one for the heavy species and one for the electrons. The heavy species are modeled as discrete particles, whereas the electrons are modeled as a fluid. MPIC utilizes a detailed electron fluid model, and links its two submodels by assuming quasineutrality.

1.1.2.6 Past Efforts in Hall Thruster Plume Modeling

In the past decade, different computer codes using many of the models outlined in the previous section have emerged as viable options for simulating Hall thruster plasmas. A fully fluid approach has been developed at JPL [26, 27], such that the Hall thruster plasma from the anode into the near-field is simulated with a single code. Refs. [26, 27] show that fluid models are viable options for plasmas that are closer to the continuum regime, i.e. plasmas where the thruster-diameter-based Knudsen number is below 0.1 . However, this is only applicable to the internal thruster plasma and the very near-field plume, and thus may not be a viable method for examining spacecraft integration issues specific to the far-field plume. Additionally, unsteady behavior that is regularly observed in Hall thrusters is not yet adequately resolved using this approach [26].

A further attempt has been made that models a Hall thruster plasma from the anode into the plume using a fully kinetic approach [28, 29]. This method was used in order to fully resolve electron behavior in the plasma. However, the high computational cost of using the fully kinetic approach necessitates scaling down the computational domain [29], precluding simulation of the far-field plume. Additionally, the computational cost required using a type of Monte Carlo collision (MCC) model not applicable in the far-field plume. Collision models are discussed in greater detail in

Chapter 2.

Since Boyd's review of Hall thruster modeling [30], simulations restricted solely to Hall thruster plumes are typically hybrid methods [31, 32, 33, 34, 35, 23, 36]. Most of these hybrid methods employ similar approaches for the heavy species submodel, where the main difference between each approach is typically in the choice of electron submodel. Electron submodels are usually based on either a simple Boltzmann relation, or a more sophisticated conservation-law model. The hybrid methods in Refs. [31, 32, 33, 34, 35, 23, 36] all utilize similar heavy species submodels, modeling collisions using a direct simulation Monte Carlo (DSMC) method; Refs. [31, 32, 33, 34] utilize the Boltzmann relation for the electron submodel, whereas Refs. [35, 23, 36] utilize an electron fluid submodel based on mass, momentum, and energy conservation. The differences between these models are discussed in greater detail in Chapter 2.

Finally, one objective of this work is to link together two separate computer codes in order to improve Hall thruster plume modeling since inflow conditions significantly impact the resulting structure of Hall thruster plumes [36]. Further, as Refs. [26, 29] demonstrate, it is difficult for a single code to accurately resolve a Hall thruster plasma from the anode into the far-field plume. Coupling together two codes is a type of study that has been done before: the approach in Ref. [31] used an internal plasma model based on Monte Carlo Collision (MCC) modeling that was developed from two previous internal plasma models [37, 38]; the internal plasma model was then coupled to a plume simulation model that utilized a DSMC method and the Boltzmann relation. The approach in Ref. [33] used a similar model for the plume simulations; however, Ref. [33] utilized a previous version of HPHall in order to simulate the internal plasma. Ref. [39] reports an approach that is identical to that in Ref. [33], in order to provide a complement to experimental data. Ref. [23] reports the development of a hydrodynamic code in order to simulate internal

thruster plasma that is subsequently coupled to a plume simulation that utilized DSMC methods and an electron fluid model. Based on this previous work, the present study represents contributions to the field in the following ways: first, the internal thruster model that is used is more robust than the models used in Refs. [31], [33], or [23], as will be shown in Chapter 3. Second, the plume simulations utilize collision models based on state-of-the-art measurements. This type of collision model has only been numerically validated very recently [40]; however, it has not as of yet been utilized in a full plume simulation. Results of the implementation in a full plume simulation are shown in Chapter 4. Third, the present study represents the first implementation in which a particle-fluid hybrid model for the internal plasma has been coupled to a particle-fluid hybrid model for the plasma plume. Further, the procedure in which separate codes for the internal plasma and the plasma plume are coupled is validated through comparisons between plasma properties in the very near-field plume: these comparisons will show the necessity for using different computational models for different regions of the Hall thruster plasma. This is discussed in greater detail in Chapter 5.

1.2 Dissertation Objectives and Outline

Broadly construed, the objective of this dissertation is to improve Hall thruster plume modeling accuracy and computational efficiency through two methods. First, plume modeling accuracy can be improved via code development: recent experimental data will be utilized to refine collision dynamics of the heavy species submodel in MPIC. Second, plume modeling accuracy and computational efficiency can be improved by linking it together with a state-of-the-art Hall thruster internal plasma model, HPHall. This coupling provides two advantages. First, it provides a scientific way of calculating boundary conditions at the thruster exit (TE) plane. These boundary conditions have a significant influence on the accuracy of the resulting

plume structure. Second, coupling these two models will also mitigate a potential disadvantage of MPIC, namely the neglecting of magnetic fields. MPIC neglects the effect of magnetic fields in order to reduce computational cost, therefore coupling MPIC and HPHall can improve computational efficiency. The success of this project will be measured by comparing newly generated computational results to: *i*) previously validated computational models, and *ii*) recent experimental data.

1. Boundary Condition Refinement. Previous studies that utilized MPIC in order to simulate Hall thruster plumes have concluded that boundary conditions at the TE plane have a significant impact on the final structure of the plume [25, 41, 36]. Unless experimental data is available and wide-ranging at the TE plane, options for scientifically determining such boundary conditions are few. In the present study, the internal Hall thruster plasma model HPHall is utilized to scientifically determine plasma conditions at the TE plane which can subsequently be fed into MPIC as inflow boundary conditions. This is potentially a significant improvement over semi-empirical methods of determining TE plane boundary conditions. In order to assess the accuracy of HPHall, the present study will be comparing a recently developed version (H3) to both a previous version (H2) and experimental data taken at PEPL. Specifically, this study will be comparing H2 and H3 results to experimental data acquired via each method outlined above, including LIF velocimetry. This is the first study to validate computational results against this velocimetry data.

2. Code Development. Regarding the heavy species submodel, MPIC has previously utilized simple scattering models due to the unknown angular dependence of particles involved in CEX collisions or elastic collisions involving high velocity ions and neutrals. For example, elastic collisions have been assumed to result in isotropic scattering and CEX collisions have been assumed to scatter according to an analytical curve fit. However, recent experimental measurements of

ion-atom interactions for singly-charged and doubly-charged xenon ions have enabled the computation of differential cross sections at typical Hall thruster ion energies. This allows for more accurate calculation of collision dynamics. Implementation of this new algorithm has already taken place in HPHall development. In the present study, this new approach to collision dynamics is extended to MPIC in order to assess its effect on plume simulation as compared to experimental data. The present study represents the first application of this new approach to collision dynamics in a plume simulation model as robust as MPIC.

3. Near-field Plume Characterization. MPIC is a widely developed plume simulation model with the capability of modeling an imposed magnetic field. This capability comes with great numerical expense, both in terms of computational wall time and numerical stability. Additionally, detailed magnetic field data is required over a large domain. Therefore, the present study utilizes a version of MPIC which neglects imposed magnetic fields. This lack of physical modeling will have the greatest impact in regions where the magnetic field is very strong. These regions are mostly confined to the near-field of the plume, within the overlap region of the two computational domains. Since HPHall models the magnetic field of the thruster, the computational results predicted by HPHall in the very-near field plume should be more accurate than those predicted by the version of MPIC that neglects the magnetic field. As a result, the present study will investigate the effect of mapping the thruster inlet onto a magnetic field line outside the strongest regions of the $\vec{B}$ field. HPHall allows for computing spatially resolved plasma conditions at a variety of locations within its computational domain, resulting in more control over boundary conditions for MPIC. Mapping the TE plane onto an effective inlet allows MPIC to start its simulations outside of the strong $\vec{B}$ field regions, resulting in more accurate

predictions as compared to experimental data.

The rest of the dissertation is organized as follows. Chapter 2 will review the background of rarefied gas theory and simulation methods, including techniques that pertain specifically to the numerical techniques utilized by MPIC and HPHall. Chapter 3 begins the discussion of the results of applying the methods described in Chapter 2. Specifically, Chapter 3 investigates the first objective of this dissertation, incorporation of a new collision dynamics algorithm into MPIC. Chapter 4 investigates the second objective of this dissertation, comparison of H2 and H3 to experimental data and examination of the use of H2 and H3 in generating boundary conditions for MPIC. Chapter 5 investigates the third objective of this dissertation, examination of the near-field plume and the effect of mapping the thruster inlet onto a contour outside of the strong magnetic field region of the domain. Finally, Chapter 6 summarizes the findings of Chapters 3-5 and makes recommendations for future work.

CHAPTER II

Methodology and Governing Equations

As outlined in Section 1.2, the present study will utilize two different computational models in order to examine a 6 kW Hall thruster's internal plasma flow and plasma plume. Therefore, this chapter will provide general background and discuss numerical techniques utilized by both models. The plasmas under consideration are predominantly in a transitional flow regime, i.e. the thruster-diameter-based Knudsen number is between 0.1 and 10 (starting at the anode and extending into the plume). Small regions in the far-field of the plasma plume are in a fully free molecular flow regime, i.e. the Knudsen number is on the order of 10. As such, it is important to review rarefied gas theory. After this review, various numerical techniques that are suited for simulation of such gases are explained.

2.1 Rarefied Gas Background

A gas flow can be modeled at either the macroscopic or the molecular level. Macroscopic-level models assume that gases can be accurately represented as continuous media. Once this continuum hypothesis is made, these models solve for macroscopic flow information such as velocity, temperature, pressure, and density. Models that assume the continuum hypothesis for gases and subsequently utilize the Navier-Stokes (NS) equations as governing flow physics are typical examples of

macroscopic-level approaches. Molecular models assume that gases can be accurately represented as a host of discrete particles with inner structure. Such molecular models solve for particle properties such as position, velocity, and internal state. Models that utilize the Boltzmann equation are typical examples of molecular-level approaches. The present study utilizes a molecular-level approach to analyze the properties of internal plasma flows and plasma plumes. Therefore, it is important to characterize the circumstances under which molecular-level models are preferred to macroscopic-level models.

Macroscopic flow properties are defined as average values of molecular quantities, and these properties are well defined as long as there are a sufficient number of molecules within the smallest significant volume of a flow. If this condition is satisfied, i.e. if the continuum hypothesis holds, then results from molecular models can be expressed in terms of typical macroscopic properties. However, when a gas becomes rarefied the condition no longer holds: the number of molecules in the smallest significant volume is not sufficient such that macroscopic properties are well defined, and using a macroscopic-level method will result in a loss of accuracy. Consider the example of the NS equations: when the continuum hypothesis fails, length scales associated with the gradient of flow properties are on the same order of magnitude as length scales associated with the average distance traveled by molecules between collisions. Transport terms in the NS equations assume that these length scales are not on the same order, and so are similarly not well defined. In order to quantify the degree of rarefaction of a gas, and implicitly the degree to which the continuum hypothesis fails, the average distance traveled by molecules between collisions is normalized by a characteristic length scale of the flow, resulting in the Knudsen number:

$$K_n = \frac{\lambda}{L} \tag{2.1}$$

Here, λ is defined as the mean free path, the average distance a molecule travels be-

tween collisions, and L is a characteristic length dimension of the flow. Typically, the upper bound of NS-equation validity is a K_n of about 0.01. Where K_n exceeds 0.01, the error in macroscopic-level models is significant, and kinetic or hybrid simulation methods should be considered. To mitigate the effects of rarefaction, the present study utilizes a hybrid model, consisting of a heavy species submodel and an electron submodel, for simulating both the thruster's internal plasma flow and the plasma plume. These two submodels are linked together via the assumption of quasineutrality such that $n_i = n_e$. The heavy species submodels will be explained below in Section 2.2. The electron submodels will be explained subsequently in Section 2.3.

2.2 Particle Methods

In particle simulations, the computational domain is divided into a network of cells, with each cell functioning as a region wherein molecular interactions take place and sampling of flow information occurs. Simulating every molecule in a given plasma is ordinarily unfeasible, however. Therefore, particle methods treat physical systems kinetically by tracking the motion of a representative number of computational particles, or "macroparticles," where each individual macroparticle represents a large number of real particles. In order to capture non-linear behavior as predicted by the Boltzmann equation, particle methods generally model real molecular collisions in a statistical manner. This is a computational tradeoff, and so, in order to resolve plasma inhomogeneities and maintain good statistics, the number of macroparticles in any given cell should be greater than 20 [42]. Note also that in the physical plasmas under consideration, neutral and ion densities differ by several orders of magnitude, and therefore there is a corresponding difference in numerical weight between macroparticles representing neutrals ("macroneutrals") and macroparticles representing ions ("macroions"). This difference can have consequences in collisional processes, as will be outlined below.

Since HPHall and MPIC utilize different particle method submodels, they will be characterized separately. First, the HPHall submodel is described in Section 2.2.1, with the MPIC submodel being described subsequently in Section 2.2.2. Note that time-averaged results from both submodels are presented, and both submodels are meant to represent atomic xenon, which is used exclusively in this dissertation.

2.2.1 The Heavy Species Submodel in HPHall

The heavy species submodel in HPHall is a type of Particle-In-Cell (PIC) method [21]. PIC methods characteristically track the motion of collections of charged particles, making them attractive options for analyzing plasmas. This method is well-understood, and a detailed description can be found in [43]. Application of PIC methods is fairly wide-ranging but has shown exceptional applicability to EP devices [22, 44, 45].

The basic concept on which PIC methods are based is as follows: a plasma is modeled as a collection of charged macroparticles that interact both with each other and with external fields. Macroparticles are injected at inlet boundaries using kinetic theory to decide properties such as the number of particles injected and their respective velocities. The particles then follow trajectories that are determined by Newton's 2$^{\text{nd}}$ Law subject to Lorentz forces, which are represented as follows:

$$\vec{F} \;=\; \frac{e}{m}\left(\vec{E} \;+\; \vec{v}\times\vec{B}\right) \;+\; \vec{R}_o \tag{2.2}$$

Here, $\vec{F}$ is the force acting on a macroparticle; $\frac{e}{m}$ is the charge-to-mass ratio (zero for neutrals); $\vec{E}$ is the electric field; $\vec{v}$ is the velocity of the macroparticle; $\vec{B}$ is the magnetic field; and finally, $\vec{R}_o$ is any non-electromagnetic force. Note that, in addition to being subject to Lorentz forces, collisions also affect macroparticle momentum. However, both HPHall and MPIC heavy species submodels account for collision-based momentum change in ways that separate collision dynamics from trajectory

calculation according to Eqn. (2.2).

Since the computational domain consists of a set of discretized points, the electromagnetic fields are not continuous in space or in time. The lines which divide the computational domain into cells intersect at grid points, and each of these grid points has assigned fields and charge densities. These fields and densities are assigned via a weighting algorithm that is outlined in Section 2.5.3. Macroparticles that occupy a given cell are then subject to the fields assigned to the various grid points which define the given cell. Macroparticle motion is computed via Eqn. (2.2), assuming the fields to be constant throughout the timestep Δt. After macroparticle motion has been computed for the timestep, the discretized field equations are solved and the field distribution is updated.

In general, the computational results of PIC methods are reliant on timestep size, cell size, and number of macroparticles used. The fields calculated at grid points which are interpolated to macroparticles within a given cell are the only forces that act on those macroparticles. This is a physically accurate model for non-neutral plasmas, provided that the cell sizes are on the order of the Debye length: physically, charged particles within a Debye length of each other interact with each other, whereas particles separated by more than a Debye length are shielded from each other and thus do not interact. Further, timescales of the physical phenomena of non-neutral plasmas are on the order of the inverse of the plasma frequency, shown below:

$$\omega_p \;=\; \sqrt{\frac{n_e e^2}{\epsilon_o m}} \tag{2.3}$$

The present study, however, assumes quasineutrality, such that Debye length restrictions on cell size and plasma freqency restrictions on timestep size are not applicable. Instead, the contraints of cell size, timestep size, and number of macroparticles stem from typical direct simulation Monte Carlo (DSMC) contraints, as outlined below in Section 2.2.2. Additionally, to compute the movement and interaction of macropar-

ticles, the timestep in HPHall has a further constraint: it should be selected so that one macroion does not advance more than one cell.

The heavy species submodel in HPHall utilizes a PIC method to model neutral xenon atoms (Xe), single-charged xenon ions (Xe^{+}), and double-charged xenon ions (Xe^{2+}). The general procedure of this submodel is as follows:

1. Load the static magnetic field and interpolate it to the grid. Note that, as described in Section 1.1.2.5, the magnetic field is considered static, therefore this step is only performed once.

2. Calculate the distribution of charge density and corresponding potential field by weighting macroion charges onto their local grid points.

3. Calculate the electric field by $\vec{E} = -\nabla\phi$.

4. Calculate updated properties for macroneutrals. This process consists of a handful of algorithms, outlined below in 2.2.1.1.

5. Calculate updated properties for macroions. This process also consists of a handful of algorithms, also outlined in 2.2.1.1.

6. Sample flow information.

Although HPHall computes variations in plasma properties over time, the present study is primarily concerned with time-averaged solutions. Therefore, the above steps (excepting 1.) are repeated until a pre-determined amount of time is reached.

2.2.1.1 Outline of Neutral and Ion Updating in HPHall

Updating properties for macroneutrals consists of the following steps:

1. Inject neutrals at inlet boundaries. In HPHall, there are three boundaries which function as inlets for neutrals: injection of propellant, in the form of neutrals

from the anode; injection of neutrals at wall boundaries due to recombination processes; and injection of neutrals from downstream boundaries, in order to emulate facility back-pressure.

2. Delete neutrals that have undergone ionization. In HPHall, ionization is computed via the electron submodel. The process is outlined below in Section 2.3.1.

3. Move neutrals. Trajectories of neutrals are calculated according to Eqn. (2.2), where $\vec{R}_o$ is the only force influencing neutral motion. Momentum-exchange (MEX) collisions are ignored as in Ref. [46]; thus $\vec{R}_o$ is the average resistive force felt by neutrals due solely to CEX collisions. HPHall handles CEX collisions using a Monte Carlo Collision (MCC) method, which is outlined below in the update procedure for macroions.

4. Apply boundary conditions. For each time step, neutral trajectories are tested to determine if their updated location crosses a computational boundary. If a neutral does in fact cross a boundary, one of two conditions is applied: if the boundary is an outflow boundary, the neutral is deleted from the simulation; if the boundary is a wall, the precise location of impact is determined, and the neutral is reflected diffusely such that the normal velocity component is sampled from a biased Maxwellian VDF.

Updating properties for the macroions consists of the following steps:

1. Perform CEX collisions with neutrals, making CEX ions and neutrals and scattering ions off neutrals. HPHall utilizes an MCC method for handling CEX collisions: these collisions affect the macroions individually; however, CEX collisions affect the macroneutrals only in an average sense. The basic parameter used to calculate the impact of CEX collisions is the rate parameter:

$$\zeta_{CEX} \;=\; \sigma_{CEX}\left(g\right) \cdot g \tag{2.4}$$

where ζ_{CEX} is based on the CEX cross section and relative macroscopic velocity, g. Note that σ_{CEX} will vary depending on the degree of ionization of the macroion: $Xe - Xe^{+}$ cross sections are about twice as large as $Xe - Xe^{2+}$ cross sections [47], [48]. The probability that a macroion undergoes a CEX collision is then based on the following:

$$P_{CEX} \;=\; 1 - \exp\left(n_n \zeta_{CEX} \Delta t\right) \tag{2.5}$$

Thus, for macroions, CEX collisions are decided probabilistically, and should a collision occur, new macroion velocities are determined by randomly sampling from a Maxwellian VDF. However, for each macroneutral, CEX collisions are modeled as a macroscopic resistive force:

$$\vec{R_o} \;=\; m_n n_i \zeta_{CEX} \vec{g} \tag{2.6}$$

CEX collisions thus affect macroneutrals in a bulk sense. Generally, the MCC method gives good results in internal plasma flows since the macroscopic velocities are similar in magnitude [21]. While this method is the only collision algorithm H2 utilizes, H3 offers a choice between this algorithm and a DSMC algorithm, which will be outlined in Section 2.2.2.

2. Move ions. Trajectories of macroions are calculated according to Eqn. (2.2), where $\vec{B}$ and $\vec{E}$ influence ion motion, and $\vec{R_o}$ is not applicable.

3. Apply boundary conditions. For each time step, ion trajectories are tested to determine if their updated location crosses a computational boundary. If an ion does in fact cross a boundary, one of four conditions is applied: if the boundary is an outflow boundary, the ion is deleted from the simulation; if the boundary is part of the anode, the ion loses its charge and is re-emitted

as a neutral, assuming 50% of its energy is lost to the wall and assuming the reflected direction is randomized; if the boundary is any other wall, the process is identical to that of the anode case, except the charge is collected in order to determine wall potential.

2.2.2 The Heavy Species Submodel in MPIC

The heavy species submodel in MPIC is a hybrid submodel: a DSMC algorithm is used to model collision dynamics, whereas a PIC algorithm is used to model the behavior of physical plasmas. The DSMC algorithm is described in Section 2.2.3 and the PIC algorithm is described in Section 2.2.4.

2.2.3 The DSMC Algorithm in MPIC

The DSMC method is the most common particle method used to simulate rarefied gas flows [42]. The method was introduced first by Bird in the 1960's [49]. Since then, it has been developed as a reliable, accurate tool which has gained widespread acceptance, notably for its accurate prediction of the inner structure of normal shock waves [22]. Additionally, the DSMC method is widely described in the literature [50, 51, 52, 53, 54].

As one kind of particle method initially described in 2.2, DSMC emulates the non-linear Boltzmann equation by simulating real molecular collisions. Similar to the previously described particle method, macroparticles are used to represent a much greater number of physical particles. Collisions between macroparticles are then modeled via collision frequencies and scattering velocity distributions that are determined from kinetic theory of rarefied gases. One of the basic assumptions of the DSMC method is that these collisions can be decoupled from particle motion. This assumption constrains certain simulation parameters: it requires the simulation timestep Δt to be smaller than the local mean collision time, and that the cell size in

the simulation be smaller than the mean free path. These requirements increase the amount of computational cost when compared to continuum-based methods. DSMC does, however, provide physically accurate results: Bird [55] has shown that, given a sufficiently large collection of macroparticles, the Boltzmann equation can be derived from the DSMC method.

The DSMC method has two principal limitations: the assumption of molecular chaos, and the dilute gas assumption. The assumption of molecular chaos requires macroparticles which collide with one another do not collide again until they have collided multiple times with multiple other particles. Effectively, assuming molecular chaos requires the velocities of collision pairs to be completely uncorrelated. The dilute gas assumption excludes DSMC methods from being applied to dense gases in which many-body interactions dominate, or extremely ionized plasmas in which long-range interactions dominate.

The DSMC algorithm that MPIC utilizes is similar to the algorithm described in 2.2.1: the computational domain under consideration is subdivided into cells wherein molecular interaction occurs. To calculate molecular interaction and macroparticle motion, a timestep is employed that is physically determined. In this case, the constraint on the timestep is that it must be smaller than the mean collision time of molecules. However, there are two major differences between the heavy species submodels in HPHall and MPIC. First, collision dynamics are computed differently: the essential difference between DSMC and MCC methods is that the DSMC method explicitly chooses two macroparticles and collides them, with momentum being transferred from/to both macroparticles; the MCC method chooses a single macroion and scatters it off a bulk of macroneutrals, such that momentum is transferred from/to macroions individually, but from/to macroneutrals in a bulk sense. This is explained in further detail in 2.2.3.2. Second, macroparticles are still subject to the Lorentz forces described by Eqn. (2.2), but in the present study, MPIC ignores magnetic

fields. This difference is specific to the PIC algorithm that is coupled with the DSMC algorithm in MPIC, and is described in 2.2.4.

2.2.3.1 The DSMC Procedure

The general procedure employed by the DSMC algorithm is as follows:

1. Select collision pairs. Pairs of macroparticles are randomly selected to collide. Random selection is governed by kinetic theory in order to replicate the physical collision frequency.

2. Perform binary collisions. The collision process consists of a redistribution of all types of energies and chemical reactions subject to the constraint that momentum and energy are conserved.

3. Inject new macroparticles at inlet boundaries. The number of particles injected and velocities of said particles are determined according to a Maxwellian VDF.

4. Move macroparticles and compute interactions with other boundaries. Particle motion occurs at a constant velocity with no interaction with other particles. As such, particle trajectories are calculated deterministically. Boundary interactions include: particles that travel from cell to cell, particles that cross an outflow boundary and are subsequently deleted, and particles that interact with wall boundaries and are reflected back.

5. Sample flow information.

Since this is a steady-flow simulation, the above steps are repeated until a predetermined amount of time is reached.

2.2.3.2 Collision Dynamics in DSMC

MEX collisions between macroparticles are evaluated by randomly selecting pairs in a given cell, regardless of their respective position or velocity. The total number of candidate pairs selected for collisions per timestep is calculated using Bird's No-Time-Counter (NTC) scheme [42]:

$$\text{Total number of pairs } = \frac{1}{2} n \overline{N} \left(\sigma g\right)_{max} \Delta t \tag{2.7}$$

Note that Eqn. (2.7) governs the number of pairs that are candidates for collisions in all DSMC simulations in the present study. Whether or not a collision actually occurs depends on the collision probability of the pair. This probability is computed by normalizing (σg) by the maximum (σg) for any pair in the given cell. This probability is then compared to a random number, R, that is uniformly distributed in $[0, 1]$. Mathematically, the candidate pair will undergo a collision if the following equation is satisfied:

$$\left(\sigma g\right) / \left(\sigma g\right)_{max} \; > \; R \tag{2.8}$$

Note that $\left(\sigma g\right)_{max}$ is initially set to an approximate value and automatically updated if a larger value is encountered during the simulation.

In order to use Eqn. (2.8) to determine collision events, the collision cross section σ must be calculated. One method of doing this is to use a typical inverse power law potential model. This method is not numerically stable: for certain conditions, the model calculates an infinite cross section. In order to avoid numerical instabilities, Bird [50] introduced the Variable Hard Sphere (VHS) model as a first-order approximation to the inverse power law potential model. In the VHS model, the total cross section σ is allowed to vary with the relative speed of the two colliding molecules as follows:

$$\frac{\sigma_{MEX}}{\sigma_r} = \frac{g^{1-2\omega}}{g_r^{1-2\omega}} \tag{2.9}$$

Here, g_r is the relative collision speed at a reference temperature T_r and σ_r is the reference cross section based on a reference molecular diameter: $\sigma_r = \pi d_r^2$. Assuming $T_r = 273K$, ω and d_r values can be found for several major species in [42].

Once a collision is determined to occur, post-collision properties are calculated. Conservation of momentum and conservation of energy provide four out of the six equations required to calculate post-collision velocities. Typically, assumptions regarding the post-collision velocity direction, or scattering angle, are made to provide the remaining equations. In the present study, the MEX scattering angles are calculated by one of two methods: *i*) isotropic scattering is assumed, or *ii*) statistical scattering based on measured differential cross sections is assumed. Method *i*) treats the angular dependence of the colliding particles as unknown and assigns the direction of the post-collision relative velocity vector at random on a unit sphere. Method *ii*) is based on recent measurements of ion-atom interactions: these data are used to determine the post-collision in-plane relative velocity angles , whereas out-of-plane angles are chosen randomly. Hereafter, MPIC simulations utilizing method *i*) are named MPIC1 simulations, and those utilizing method *ii*) are named MPIC2 simulations. It should be noted here that the heavy species submodel utilized by H3 has been updated to offer a DSMC method for handling ion-atom collisions that is identical to method *ii*): this is the main difference between H2 and H3.

2.2.3.3 Boundary Conditions in DSMC

The application of boundary conditions to macroparticles is dependent on what type of boundary they interact with. Macroparticles that interact with an outflow boundary are deleted. Macroparticle-wall interaction varies according to which type of wall they hit. The two most common types of walls in DSMC simulations are spec-

ular and diffuse walls. If the interaction is with a specular wall, the macroparticle's normal velocity component changes its sign and the tangential velocity component is unaffected. If the interaction is with a diffuse wall at a temperature T_w, its tangential velocity components are sampled from a Maxwellian distribution, such that:

$$f(c_t)\,dc_t = \frac{1}{\sqrt{2\pi RT_w}} \exp\left(\frac{-c_t^2}{2RT_w}\right) dc_t \tag{2.10}$$

The normal velocity component is sampled from a biased Maxwellian distribution:

$$f(c_n)\,dc_n = \frac{1}{2RT_w} c_n \exp\left(\frac{-c_n^2}{2RT_w}\right) dc_n \tag{2.11}$$

Determination of what type of interaction macroparticles have with a given wall depends on the wall's accommodation coefficient, ν. Accommodation coefficients describe the fraction of particles that can thermalize to the wall temperature before reflecting and are therefore fully accommodated: ν thus represents the fraction of particles that are fully accommodated and reflect diffusely; $1 - \nu$ represents the remaining fraction of particles that are incompletely accommodated and reflect specularly. Note that the internal energy of a reflecting particle can be handled separately, but, as stated in Section 2.2, atomic xenon is used exclusively in the present study, so internal energy considerations are ignored.

2.2.4 The DSMC-PIC Algorithm in MPIC

The PIC algorithm is the second half of the heavy species submodel utilized by MPIC. It is coupled to the DSMC algorithm described in Section 2.2.3 to form a heavy species submodel that is very similar to that described in Section 2.2.1. There are two major differences between strict DSMC modeling and DSMC-PIC. The first difference is the addition of collision classes that comes with additional species: the collision dynamics described in 2.2.3.2 only represented collisions between two macroneu-

tral particles, whereas the PIC algorithm introduces two new species, single-charged macroions and double-charged macroions. In addition to MEX collisions, the addition of macroion species requires modeling of CEX collisions. Therefore, compared to strict DSMC modeling, the number of different collision types increases from one to five: neutral-neutral MEX, neutral-single ion MEX/CEX, and neutral-double ion MEX/CEX (where ion-ion collisions are ignored).

The second major difference between strict DSMC modeling and DSMC-PIC can be summarized in the following equation which describes the forces macroparticles are subject to in the PIC algorithm that MPIC utilizes:

$$\vec{F} = \frac{e}{m}\vec{E} \tag{2.12}$$

Since macroparticle collisions account for momentum transfer between individual particles, there is no need to model the resistive force $\vec{R_o}$ that derives from the MCC method; because MPIC does not resolve magnetic field effects, there is similarly no model for the magnetic force $\vec{B}$ due to the imposed field.

2.2.4.1 The DSMC-PIC Procedure in MPIC

The general procedure employed by the DSMC-PIC algorithm is similar to the basic DSMC procedure with extra steps to account for forces acting on charged macroparticles. The procedure is summarized as follows:

1. Calculate the distribution of charge density and corresponding potential field by weighting macroion charges onto their local grid points.

2. Calculate macroneutral ionization in all cells. A fraction of neutrals are converted to ions using the following relation: $\Delta n_i = C_i n_i n_n \Delta t$, where the ionization rate C_i is determined by Eqn. (2.24) as explained in Section 2.3.2.2.

3. Calculate the electric field by $\vec{E} = -\nabla\phi$.

4. Perform collisions. Two classes of collisions are accounted for in DSMC-PIC: momentum-exchange (MEX) collisions and charge-exchange (CEX) collisions. MEX collisions occur in the following pairs: $Xe - Xe$, $Xe - Xe^{+}$, and $Xe - Xe^{2+}$. CEX collisions occur in $Xe - Xe^{+}$ and $Xe - Xe^{2+}$ pairs. CEX collisions result when a macroion passes a macroneutral: charge is transferred from the typically faster ion to the typically slower neutral, with the result that CEX collisions produce fast moving neutrals and slow moving ions.

5. Inject new macroparticles at inlet boundaries.

6. Determine macroion acceleration in a given cell from the coordinates of the particle and the electric field at each node that defines the cell.

7. Move macroparticles based on position, velocity, and acceleration, and compute interactions with other boundaries. Ion-boundary interactions are identical to neutral-boundary interactions, with the sole difference being that ions interacting with walls additionally lose their charge.

8. Sample flow information.

2.2.4.2 Collision Dynamics in DSMC-PIC

As outlined above in Section 2.2.3.2, collisions in DSMC-PIC are evaluated by randomly selecting pairs in a given cell, with the total number of candidate pairs selected for collisions per timestep being governed by the NTC scheme. The collision probability of the pair is similarly computed by normalizing (σg) by the maximum (σg) for any pair in the given cell. This probability is then compared to a random number, R, to determine if a collision occurs.

Collision cross sections between macroneutrals are computed as shown in Section 2.2.3.2, while four additional cross sections must be calculated for MEX and CEX collisions between macroneutrals and macroions. The MEX cross section for

$Xe - Xe^+$ pairs that is utilized in the present study is based on measurements by Pullins et al. [47] and Miller et al. [48]:

$$\sigma_{MEX}\left(Xe, Xe^+\right) \;=\; 1.0 \times 10^{-20}\left(87.3 - 13.6 \log \frac{m_c g^2}{2e}\right) m^2 \tag{2.13}$$

where m_c is the reduced mass. Based on previous work [22, 23], the present study assumes that MEX and CEX cross sections are similar enough to be equated:

$$\sigma_{MEX}\left(Xe, Xe^+\right) \;=\; \sigma_{CEX}\left(Xe, Xe^+\right) \tag{2.14}$$

$$\sigma_{MEX}\left(Xe, Xe^{2+}\right) \;=\; \sigma_{CEX}\left(Xe, Xe^{2+}\right) \tag{2.15}$$

Pullins et al. [47] and Miller et al. [48] additionally report that the CEX cross section for $Xe - Xe^{2+}$ pairs is approximately half as large as the cross section for $Xe - Xe^+$ pairs at corresponding energies. Therefore, the present study assumes that CEX cross sections are related:

$$\sigma_{CEX}\left(Xe, Xe^{2+}\right) \;=\; \frac{1}{2} \times \sigma_{CEX}\left(Xe, Xe^+\right) \tag{2.16}$$

The four additional cross sections required by the addition of two ion species are thus fully determined. Since MEX and CEX cross sections are assumed to be identical, one additional specification needs to be made in order to determine if a particular $Xe - Xe^+$ (or $Xe - Xe^{2+}$) interaction is MEX or CEX. Based on previous work [22, 23], the present study assumes that these collision types are equally likely; therefore, each is assigned a probability of 0.5. If a collision is determined to occur based on Eqn. (2.8), the collision type is then determined by comparison to a randomly generated number that is uniformly distributed in $[0, 1]$.

Once a collision is determined to occur, post-collision properties are calculated. MEX collisions are handled as outlined in Section 2.2.3.2. CEX collisions and their

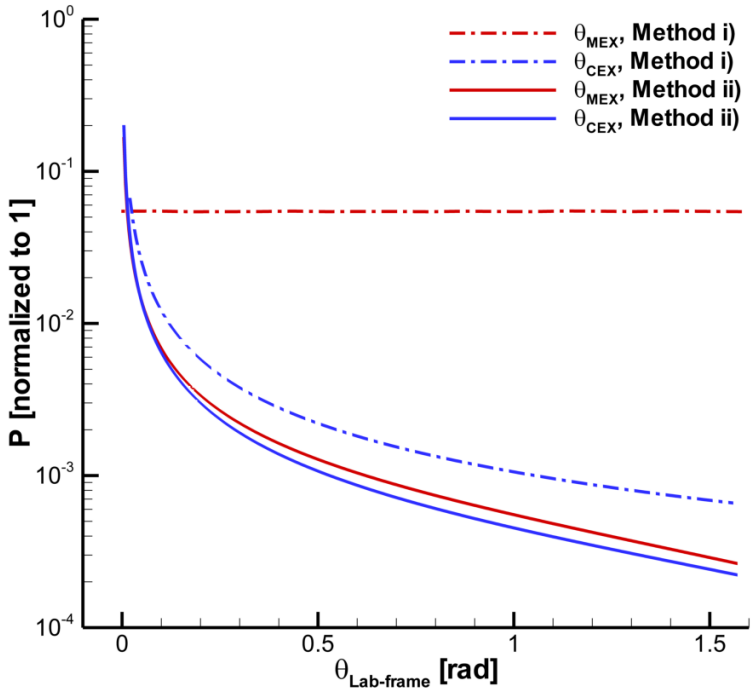

Figure 2.1: Scattering angle distributions sampled from in DSMC-PIC collisions.

effects are modeled by creating an ion moving at the bulk velocity of neutrals at the original ion's location. The original ion is then removed from the list of ions and added to the list of neutrals. Scattering angles for CEX collisions are subsequently calculated one of two ways, corresponding to the two methods for calculating MEX collision scattering angles : *i*) an analytical distribution is sampled from; *ii*) a curve fit based on empirical data is sampled from. Since scattering angles for CEX collisions are relatively small due to the lack of momentum transfer, the curve fit in method *i*) is biased toward low-angles. Figure 2.1 illustrates the distributions from which methods *i*) and *ii*) sample to determine scattering angles for MEX and CEX collisions.

The differences between each heavy species submodel (H2, H3, MPIC1, and MPIC2) are summarized in Table 2.2.4.2. Each label indicates how each type of collision is modeled: "$DSMC_{iso}$" indicates the DSMC method assuming isotropic scattering; "$DSMC_{ana}$" indicates the DSMC method assuming an analytic distri-

Collision Type		H2	H3	MPIC1	MPIC2
MEX	$Xe - Xe$	x	x	$DSMC_{iso}$	$DSMC_{iso}$
	$Xe - Xe^{+}$	x	$DSMC_{emp}$	$DSMC_{iso}$	$DSMC_{emp}$
	$Xe - Xe^{2+}$	x	$DSMC_{emp}$	$DSMC_{iso}$	$DSMC_{emp}$
CEX	$Xe - Xe^{+}$	MCC	$DSMC_{emp}$	$DSMC_{ana}$	$DSMC_{emp}$
	$Xe - Xe^{2+}$	MCC	$DSMC_{emp}$	$DSMC_{ana}$	$DSMC_{emp}$

Table 2.1: Comparison of collision dynamics methods in heavy species submodels.

bution of scattering angles; "$DSMC_{emp}$" indicates the DSMC method assuming a distribution of scattering angles that is fit to empirical data; "MCC" indicates the MCC method assuming ions scatter off of neutrals but not vice versa; and finally, "x" indicates that the type of collision is ignored:

2.3 Electron Fluid Methods

Both HPHall and MPIC are hybrid models that are composed of a heavy species submodel and an electron submodel. To reduce computational cost, these electron submodels represent electron motion with fluid approximations. For typical thruster conditions, electron collision frequency is almost two orders of magnitude higher than ion collision frequency. Electrons are also several orders of magnitude lighter than ions and move on a much smaller timescale. Therefore, it can be assumed that electrons adjust their velocities much more quickly than ions, making the fluid approximation more appropriate. Two types of electron fluid models are utilized in the present study: a quasi-1D fluid model, and a more detailed fluid model. HPHall utilizes the quasi-1D fluid model, whereas MPIC can utilize either a simple Boltzmann relation, or the more detailed fluid model. The HPHall electron submodel is described in Section 2.3.1, whereas the MPIC models are described in Section 2.3.2.

2.3.1 The Electron Submodel in HPHall

HPHall utilizes an unsteady electron fluid model to represent the highly-magnetized, diffusive regime that characterizes internal Hall thruster plasmas. In order to capture the fluid-like properties of electron motion and transport, the fluid model is evaluated at a much smaller time-step than the heavy species submodel. This time-step is called the electron subcycle. Additionally, due to the large anisotropy created by the magnetic field, electron motion and transport can be decoupled into the direction parallel to $\vec{B}$ field lines, $\hat{s}$, and the direction perpendicular to $\vec{B}$ field lines, $\hat{n}$, such that field properties are functions of natural coordinates (s, n).

2.3.1.1 The Electron Submodel Procedure

The general procedure employed by the electron submodel in HPHall is as follows:

1. Ionization of neutrals. Ionization of neutrals is computed utilizing a unique method developed specifically for HPHall. The number of macroions N_{ionize} created per timestep due to ionization of neutrals is calculated as follows:

$$N_{ionize} = \frac{m_i}{M_i} \langle \dot{n} \rangle_{cell} V_{cell} \Delta t \tag{2.17}$$

where $\langle \dot{n} \rangle_{cell}$ is the cell-averaged ionization rate and M_i is the weight of the new macroion. This ionization rate is calculated as follows:

$$\langle \dot{n} \rangle_{cell} = n_n n_e \zeta_{ionize} (T_e) \tag{2.18}$$

where ζ_{ionize} is determined by assuming a Maxwellian VDF for the electrons and a Drawin ionization cross section model [37, 56]. New macroions are probabilistically assigned positions within the cell, and velocities are assigned using a drifting Maxwellian VDF which is based on the local bulk velocity and the

temperature of the macroneutrals. Because the typical numerical weight of a macroneutral will be much larger than a macroion, no single ionization event can ionize a macroneutral into a macroion. Therefore, macroneutrals in a given cell experience a decay in weight per timestep, $M_n - M_{n,o}$ or ΔM_n as follows:

$$\Delta M_n \;=\; -\Delta t n_e \zeta_{ionize}\left(T_e\right) \tag{2.19}$$

2. Calculate electron motion and transport. To calculate electron behavior in the parallel direction, electrons are assumed to thermalize along magnetic streamlines such that electron temperature is constant along each line. As a result, the pressure gradient and electric forces in the electron momentum equation are balanced along these lines, and a constant thermalized potential, ϕ_r can be derived for each line. The potential at any point is then:

$$\phi\left(s,n\right) \;=\; \phi_r\left(n\right) + T_e\left(n\right) \ln\left(\frac{n_e\left(s,n\right)}{n_r}\right) \tag{2.20}$$

where ϕ is the potential, T_e is the electron temperature in eV, and n_e is the electron number density (also known as the plasma density). Eqn. (2.20) is a version of the Boltzmann relation, one of the most widely used electron models in plasma simulation. Note that, although Eqn. (2.20) is usually derived in part by neglecting magnetic field effects, the assumption that electron transport can be decoupled into parallel and perpendicular directions allows for its use in this case. The reference potential ϕ_r is a function of the magnetic field line, but is constant for any individual line and thus varies only in the $\hat{n}$ direction. T_e is also constant along a magnetic field line, and is computed between field lines by integrating the electron energy equation as shown [37]:

$$\frac{\partial}{\partial t}\left(\frac{3}{2}n_e T_e\right) + \nabla \bullet \vec{q_e} \;=\; -\left(e\vec{j_e} \bullet \vec{E} \;+\; \langle \dot{n} \rangle_{cell}\, \alpha_{Dugan}\right) \tag{2.21}$$

Integration of Eqn. (2.21) requires calculating electron motion across field lines, $\vec{j_e}$. This is governed by a generalized Ohm's Law that incorporates the effects of electron collisions into an effective electron mobility across field lines, $\mu_{e,\perp}$:

$$u_{e,\perp} \;=\; \mu_{e,\perp}\left(E_{\hat{n}} + \frac{1}{en_e}\frac{\partial p_e}{\partial \hat{n}}\right) \tag{2.22}$$

Using the ideal gas law, the definition $\vec{E} \;=\; -\nabla\phi$, and Eqn. (2.20), Eqn. (2.22) can be rearranged into a form that calculates electron current density (or electron velocity) in terms of derivatives which are constant along lines of force. Therefore, field properties ϕ and T_e can be calculated using the following inputs from the heavy species submodel: neutral number density n_n, electron number density n_e, and ion current density $\vec{j}$.

3. Apply boundary conditions. For each timestep, four electron boundary conditions are applied: at a segment of the outflow boundary, electrons are injected to emulate the cathode; for the remaining segment of outflow boundary, electrons are assumed to leave the domain and a count of their flux is maintained; at the anode, electrons are assumed to be destroyed; at a wall boundary, electrons are assumed to be destroyed and charge is collected to determine the wall potential.

2.3.2 The Electron Submodel in MPIC

2.3.2.1 The Boltzmann Relation

MPIC utilizes two electron fluid models, one based on the Boltzmann relation, the other based on a detailed fluid formulation. The Boltzmann relation, Eqn. (2.20), is a version of the electron momentum equation that results from several assumptions:

the fluid electron flow is isothermal, electron pressure obeys the ideal gas law, and magnetic fields can be neglected. This is a useful approximation for basic plasma modeling, but it has several shortcomings when applied to Hall thruster plumes: plumes, especially the very near-field plume, contain significant gradients in electron number density and electron velocity. These gradients can mitigate the usefulness of the Boltzmann relation approximation. Furthermore, experimental measurements of the near field plume of Hall thrusters show magnetic field leakage which is strong enough to affect electron motion in the region [57, 58]. Previous computational investigations using MPIC have shown that neglecting the effect of magnetic field leakage in the near field yields incorrect results [23]. Currently, MPIC does not have the capability to resolve $\vec{B}$ fields; instead, HPHall's capability for modeling $\vec{B}$ fields is utilized to characterize plasma located outside of regions of significant magnetic field leakage. This characterization is then used to provide inlet boundary conditions to MPIC, with the results shown in Chapter 5.

2.3.2.2 The Detailed Fluid Model

In order to increase the level of physics as compared to the Boltzmann relation, a detailed fluid electron model is incorporated into the MPIC electron submodel [22, 23, 36, 59]. The detailed fluid model represents the electron fluid using conservation law-type equations: one equation from mass conservation, one equation from momentum conservation, and one equation from energy conservation. Each equation is assumed to describe the electron fluid at steady state and is subsequently transformed such that a fundamental electron property is obtained: electron velocity, plasma potential, and electron temperature, respectively. This transformation also results in a set of Poisson equations with source terms.

Starting with the conservation of mass equation, a streamfunction ψ is introduced such that $\nabla\psi = n_e\vec{v_e}$. The resulting conservation equation is as follows:

$$\nabla^2 \psi \;=\; n_e n_n C_i \tag{2.23}$$

where C_i is the rate coefficient. This is expressed as a function of electron temperature according to a simple model developed by Ahedo [60]:

$$C_i \;=\; \sigma_r c_e \left(1 + \frac{T_e \epsilon_i}{\left(T_e + \epsilon_i\right)^2}\right) \exp\left(-\frac{\epsilon_i}{T_e}\right) \tag{2.24}$$

Finally, the conservation of momentum equation can be transformed into a generalized Ohm's Law (Eqn. (2.25)) and combined with the charge conservation condition (Eqn. (2.26)) in order to obtain a generalized Poisson equation for the plasma potential (Eqn. (2.27)):

$$\vec{j} \;=\; \sigma \left[-\nabla\phi + \frac{1}{e n_e} \nabla \left(n_e k T_e\right)\right] \tag{2.25}$$

$$\nabla \cdot \vec{j} \;=\; 0 \tag{2.26}$$

$$\begin{aligned} \nabla \cdot \left(\sigma \nabla \phi\right) \;=& \frac{k}{e}\left(\sigma \nabla^2 T_e + \sigma T_e \nabla^2 \ln\left(n_e\right) + \sigma \nabla \ln\left(n_e\right) \cdot \nabla T_e\right) \\ &+ \frac{k}{e}\left(T_e \nabla \sigma \cdot \nabla \ln\left(n_e\right) + \nabla \sigma \cdot \nabla T_e\right) \end{aligned} \tag{2.27}$$

The conservation of energy equation can be transformed into a Poisson equation for the electron temperature [56]:

$$\begin{aligned} \nabla^2 T_e \;=\; & -\nabla \ln\left(\kappa_e\right) \cdot \nabla T_e + \frac{1}{\kappa_e}\left(-\vec{j} \cdot \vec{E} + \frac{3}{2} n_e \left(\vec{v_e} \cdot \nabla\right) k T_e\right) \\ & + \frac{1}{\kappa_e}\left(3 \frac{m_e}{m_i} \nu_e n_e k \left(T_e - T_h\right) + n_e n_n C_i \epsilon_i\right) \end{aligned} \tag{2.28}$$

where the electric conductivity σ, the electron thermal conductivity κ_e, the ion-electron collision frequency ν_{ei}, and the neutral-electron collision frequency ν_{en} can be found in [56, 61] and their references:

$$\sigma = \frac{e^2 n_e}{m_e \upsilon_e} \tag{2.29}$$

$$\kappa_e = \frac{2.4}{1 + \frac{\nu_{ei}}{\sqrt{2}\nu_e}} \frac{k^2 n_e T_e}{m_e \nu_e} \tag{2.30}$$

where $\nu_e = \nu_{ei} + \nu_{en}$ and said frequencies are evaluated for a xenon system using cross sections provided in Ref. [56].

Finally, by treating the right-hand side terms as known sources, the left-hand side properties in Eqns. (2.23), (2.27), and (2.28) are computed, yielding improved results for plasma plume simulations when compared to results computed via the Boltzmann relation. The difference between the two models is especially important in high-gradient regions of the plasma plume: the detailed fluid model more accurately simulates these regions as compared to the Boltzmann relation, since the mathematical form of the Boltzmann relation inherently limits the dynamic range of computed plasma properties [25].

2.4 Summary

This section is intended to concisely enumerate the basic steps of each hybrid method described above. The following list summarizes steps in HPHall, whereas the subsequent list summarizes steps in MPIC:

2.4.1 General Steps for HPHall

1. Initialize the static magnetic field and interpolate it to the grid.
2. Calculate the distribution of charge density and corresponding potential field by weighting macroion charges onto their local grid points.
3. Calculate the electric field by $\vec{E} = -\nabla\phi$.
4. Inject neutrals at inlet boundaries.

5. Delete neutrals that have undergone ionization in the previous timestep.

6. Move neutrals.

7. Apply boundary conditions pertaining to neutrals.

8. Perform CEX collisions with neutrals, making CEX ions and neutrals and scattering ions off neutrals.

9. Move ions.

10. Apply boundary conditions pertaining to ions.

11. Ionization of neutrals.

12. Calculate electron motion and transport.

13. Apply electron boundary conditions.

14. Sample flow information.

2.4.2 General Steps for MPIC

1. Calculate the distribution of charge density and corresponding potential field by weighting macroion charges onto their local grid points.

2. Calculate plasma potential ϕ using a fluid electron model.

3. Calculate ionization in all cells.

4. Calculate the electric field on each node by $\vec{E} = -\nabla\phi$.

5. Perform collisions.

6. Inject new macroparticles at inlet boundaries.

7. Determine macroion acceleration.

8. Move macroparticles and compute interactions with other boundaries.

9. Sample flow information.

2.5 Numerical Implementation

There are a number of issues that arise in the numerical implementation of the two hybrid methods summarized in Sections 2.4.1 and 2.4.2. This section discusses details of the implementation of particular models in each code: the finite element solver for the Poisson equations of the detailed fluid electron model, derivative calculation on unstructured grids, weighting schemes, back-pressure treatments, and macroparticle weighting.

2.5.1 Finite-Element Solution to General Poisson Equations

Eqns. (2.23), (2.27), and (2.28) can be expressed as general Poisson equations with source terms [62]:

$$-\nabla(P(x,y,z)\cdot\nabla Q(x,y,z)) \;=\; S(x,y,z) \tag{2.31}$$

where $P(x,y,z)$ is a distribution of coefficients, $Q(x,y,z)$ is a distribution of primary variables which are solved for, and $S(x,y,z)$ is a known distribution of source terms. Solution of Eqn. (2.31) is normally done by utilizing an alternating-direction, implicit (ADI) iterative solver [63, 64, 65, 66]. However, the ADI method is not well-suited for solving equations on sufficiently complex geometries or unstructured grids [23]. Therefore, the present study utilizes a general purpose finite-element solver based on the work of Ref. [22] in order to solve Eqns. (2.23), (2.27), and (2.28). This general purpose solver does not exhibit either of ADI's previously mentioned shortcomings, and is applicable to a variety of problems: structured or unstructured grids, two-dimensional or three-dimensional domains, and complex geometries. For a more

detailed discussion of the finite-element solver, see Ref. [22].

2.5.2 Derivative Calculation on Unstructured Grids

For each timestep, calculation of derivatives is required at every node. HPHall utilizes a structured grid, and derivative calculation on this grid is performed using a well-known method of successive over-relaxation (SOR) [64, 46]. MPIC, however, utilizes an unstructured grid, and derivative calculation, such as those derivatives required for calculation of the $\vec{E}$ field, is performed using a least-squares method [23, 67].

In order to calculate, for example, the $\vec{E}$ field from the plasma potential field, ϕ, it is assumed that two unknown gradients on one node are $\vec{E}(r,z) = (E_r, E_z)$. Then, if N nodes with differences in plasma potential $d(\phi)_i$ are connected to this node by distance vectors dX_i, the N nodes form $N \times 2$ relations which are overdetermined:

$$M\ E\ =\ d\phi \tag{2.32}$$

where M is an $N \times 2$ matrix, E is a 2×1 vector, and $d\phi$ is an $N \times 1$ vector. By left-multiplying each side of Eqn. (2.32) by a transposed matrix M^T, this overdetermined matrix is transformed into a 2×2 matrix of equations that can be solved.

The least-squares method requires information from every node in order to compute the derivative at one node, necessitating the formulation of a table of node connections at the start of each simulation. This table must also be maintained throughout the simulation, creating additional computational cost. However, because every other node influences the calculation of the derivative at one node, the accuracy of this method is high [23].

2.5.3 Weighting Schemes

As described in Sections 2.4.1 and 2.4.2, a common step in PIC methods is the allocation of charge density and the potential field by weighting macroions onto various grid points. Therefore, each simulation method must utilize some type of weighting function. This is a crucial step in each simulation since several important physical properties or phenomena depend in some way on the weighting function: ion number density is calculated by weighting the charges of all ions connected to a given node; particle accelerations are determined by electric fields which are in turn dependent on the weighting function; and ionization depends on accurate plasma density and neutral number density calculations, both of which have dependence traceable to the weighting function.

Since it utilizes structured grids, HPHall employs a first-order weighting function based on cell positions and cell volumes [21]. Macroions' charges are allocated to cell nodes according to weights that are calculated by the particle position within a cell and the volume of the cell. Schemes of this type are accurate for structured grids, but application of this kind of method to unstructured grids is unsound [23, 68]. Therefore, MPIC employs a different weighting function than HPHall.

MPIC employs a weighting function based on cell-averages: charge density on a specific node is calculated by summing macroion charges inside a closed area around the node and subsequently dividing by that area. The difference between this method and the method HPHall employs is as follows: the closed areas that MPIC uses to weight charge density can include all cells that are connected to a certain node, or they can include a fraction of the connected cells. Note that, because of the flexibility in which area is used to weight charge density, this method is easily implemented in parallel simulations [23]. Additionally, in order to suppress statistical scatter in density weighting calculations, MPIC utilizes a relaxation technique in ion and neutral number density on a node:

$$n_{new} = 0.1 n_{allocate} + 0.9 n_{old} \tag{2.33}$$

where n_{new} is the current ion or neutral number density, $n_{allocate}$ is the density obtained from MPIC's area-averaged weighting function, and n_{old} is the density from the previous timestep. This treatment is effective at suppressing statistical scatter in steady flow simulations [22, 23].

2.5.4 Back-pressure Treatment

As discussed in 1.1.2.4, the vacuum facility where experimental data were acquired operates with a finite background gas pressure, or simply back-pressure. Therefore, accurate computational modeling will account for back-pressure. HPHall and MPIC account for facility back-pressure in two different ways. HPHall injects a stream of macroneutrals downstream of the anode in order to emulate the effects of facility back-pressure. These neutrals have properties that are derived from the pressure and temperature of the background gas. The back-pressure-neutrals then behave as regular macroneutrals. MPIC accounts for facility back-pressure by initializing simulations with a distribution of static background neutrals: each cell contains several tagged macroneutrals with velocities sampled from a zero-centered Maxwellian VDF. These particular neutrals participate in collisions with other plume particles and change their velocities, but their positions and velocities never change.

2.5.5 Macroparticle Weights

As discussed in 2.2, the various macroparticles involved in HPHall and MPIC simulations have correspondingly varied weights. The algorithm HPHall employs for modeling different physical processes while accounting for weight disparity was described in Section 2.3.1.1. Macroparticle weighting in MPIC is modeled as follows: macroparticles have static relative weights, as well as weights depending on local cell

weight ratios. Collisions between macroparticles of disparate weights results in the splitting of the larger particle into two smaller particles: one of the new particles has an identical numerical weight to the lighter original particle, while a second new particle keeps the rest of the weight. The particles of identical weight participate in a collision, whereas the remaining particle is unchanged. Neutrals with negligible weights can be removed from the simulation completely, or have their weights statistically changed to meet a certain threshold value. A more detailed discussion of the macroparticle weighting method can be found in Refs. [22, 23].

CHAPTER III

Hall Thruster Plasma Simulations and Boundary Condition Refinement

In this chapter, results of Hall thruster plasma simulations are presented. The simulations are performed using the computer code HPHall in order to model the plasma discharge within a 6 kW Hall thruster using xenon propellant. The goal of this analysis is to supply accurate boundary conditions that can be implemented into the plume code MPIC. MPIC requires plasma properties to determine inlet flow conditions at the thruster exit (TE) plane, properties such as ion number density, electron temperature, and plasma potential. Plume structure is highly dependent on these inlet boundary conditions, therefore accurate determination of these conditions is necessary for accurate calculation of plume structure.

This chapter is divided into three parts. First, results from two different simulations are presented in order to assess effects of two different post-collision scattering models. Second, results from these simulations are compared to experimental data taken at the University of Michigan's PEPL. These comparisons are made by examining internal plasma properties as well as velocimetry data. Third, MPIC inlet boundary conditions are extracted from the internal plasma simulations for implementation into plume simulations, since plume simulations provide a further tool for assessing the accuracy of the two methods.

3.1 Evaluating Internal Plasma Models

3.1.1 HPHall Background and Differences between HPHall2 and HPHall3

HPHall is a hybrid model computer code designed to simulate the internal plasma of a Hall thruster. The computational domain of HPHall is shown in Section 1.1.2.5, whereas details regarding the HPHall code are discussed in Sections 2.2.1 and 2.3.1. The primary global inputs for HPHall are as follows: discharge potential, discharge current, cathode potential, anode mass flow rate, and the imposed magnetic field. HPHall additionally requires the following local boundary condition inputs: anode temperature, channel temperature, and injector Mach number. Finally, there are a number of modeling parameters that need to be set. Broadly, these parameters determine electron mobility, turbulence intensity, and level of electron temperature anisotropy. The present study determines the global boundary conditions, local boundary conditions, and free parameters as done in Ref. [8]. The global boundary conditions correspond to a nominal operating condition for the thruster, summarized as follows:

$$\begin{aligned} \dot{m}_{anode} &= 20\ \frac{mg}{s} \\ V_d &= 300\ V \\ I_d &= 20\ A \\ V_{cathode} &= -12\ V \end{aligned}$$

The local boundary conditions are determined as follows. The channel temperature is set based on results reported in Ref. [69], whereas the anode temperature is offset from the channel temperature by 100 K, based on the results reported in Ref. [8]. The injector Mach number is determined by simulation results also reported in [8].

The local boundary conditions are summarized as follows:

$$\begin{aligned} T_{channel} &= 940\ K \\ T_{anode} &= 840\ K \\ M_{injector} &= 0.38 \end{aligned}$$

Since HPHall utilizes global operating parameters in order to simulate Hall thrusters at specific operating conditions, it is primarily used as a tool to complement experimental projects. The fine-tuning of HPHall input parameters allows for examining trends outside the scope of experimental investigations, such as microscopic trends in collision frequency or plasma behavior outside the investigation window. The close reliance of HPHall on thruster-specific conditions has resulted in a history of good agreement between computational predictions and experimental measurements [20]. HPHall has also been successfully applied in a limited fashion to predict thruster lifetime [70]. Finally, previous work has determined that inlet flow conditions computed by HPHall are significantly more accurate in determining plume structure than semi-empirical methods which do not account for thruster-specific details or spatial resolution of properties [36]. Therefore, there is sufficient motivation to use plasma properties computed by HPHall as inlet flow conditions in MPIC.

As noted in Chapter 2, HPHall computes the time-variation of plasma properties. However, in the present study, all experimental data sets are considered time-averaged. Therefore, in order to make meaningful comparisons between HPHall results and experimental data, the HPHall results were time-averaged. In order to verify that the time-averaged results are independent of the sampling period over which the results are averaged, time-varying outputs are examined. Figure 3.1 illustrates a typical time-varying output obtained from HPHall, where the characteristic time scale of the calculated oscillations is around 1×10^{-4}.

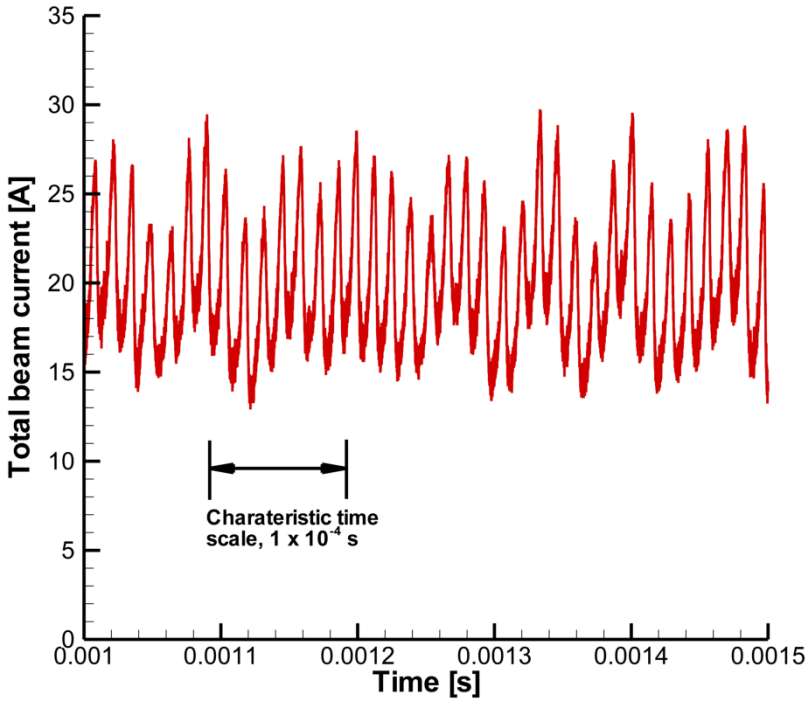

Figure 3.1: Profile of total beam current variation in time, as calculated by H2.

The computed oscillations correspond to the so-called "breathing-mode" phenomenon associated with Hall thrusters [20, 71]. Unsteady breathing-mode behavior is the primary unsteady phenomenon in Hall thrusters, and it is characterized by low-frequency, high-amplitude oscillations in the thruster plasma [71]. Using the breathing-mode time scale as the characteristic local time scale of oscillations in plasma properties, numerical parameters in HPHall are set such that the sampling period is much larger than the local time scale. This is shown explicitly in Section 3.1.2.

As outlined in Section 2.2.4.2, the heavy species submodel of H2 utilizes an MCC method. CEX collisions alter the properties of individual macroions which are then scattered isotropically. This approach to scattering has been common due to the fact that the energy and angular dependence of xenon ion-atom interactions was unknown until recently [40]. However, recent measurements of differential scattering cross sections taken at Hanscom Air Force Base have resulted in a new method for determining

scattering angles for both Xe^+ and Xe^{2+} collisions [40, 72]. Utilizing previous total cross section data, these measurements have been used to calculate absolute differential cross sections at a typical Hall thruster energy. These differential cross sections show the angular dependence of ion-atom interactions, removing the need to assume isotropic scattering. In order to utilize the new differential cross section data, H2 was modified to include an alternative method for handling collision dynamics: a DSMC algorithm was added such that MEX and CEX collisions for $Xe - Xe^+$ and $Xe - Xe^{2+}$ pairs could be computed using differential cross sections [73]. This version of HPHall is termed H3. Replacing the MCC algorithm with a DSMC alternative refines the physical model in HPHall in two ways. First, the DSMC alternative directly models both particles that participate in a binary collision, whereas the MCC algorithm represents binary collisions as one particle scattering off a background of particles. MCC-style collisions effectively spread out the influence of collisions among all background particles in a given cell. The MCC method is less computationally expensive since the effect of collisions on one half of the collision pair, the background particles, can be calculated all at once. However, the computational efficiency of this method comes with information loss and computational constraints: by averaging the effect of collisions across background particles in a given cell, MCC methods lose particle-specific information; further, MCC methods are physically appropriate only for collision pairs with similar velocity magnitudes. Both of these disadvantages are mitigated by utilizing a DSMC method. The second way in which the DSMC alternative refines the physical model of HPHall is its incorporation of two new collision types. As outlined in Section 2.2.4.2, H2 does not model any type of MEX collision. The differential cross section data incorporated into H3 models MEX collisions for $Xe - Xe^+$ and $Xe - Xe^{2+}$ pairs.

The primary difference between the H2 and H3 heavy species submodels is expected to be exhibited in macroneutral behavior: since the MCC method distributes

collision effects across macroneutrals, CEX collisions have the net effect of increasing the average velocity of Xe particles, whereas the physical effect of CEX collisions is to create a distinct population of high-speed neutrals (and a corresponding population of low-speed ions). Additionally, as outlined in Section 2.2.4.2, the H3 heavy species submodel calculates the effects of ion-atom MEX collisions, whereas H2 does not calculate the effect of any MEX collision. The inclusion of MEX collisions in H3 introduces a new source of scattering, therefore the divergence of macroneutrals (as well as macroions) is expected to increase. In order to determine the influence of the heavy species submodel, velocimetry and flux data are compared, followed by comparisons of typical plasma properties.

3.1.2 Comparison of H2 and H3 Results

The HPHall simulations are performed as described in Ref. [20]: neutral xenon atoms are injected for 20,000 timesteps, at which point xenon ions are also injected and sampling of plasma properties begins. The simulations run for an additional 80,000 timesteps. The timestep size used for the xenon particles is 5×10^{-8} seconds, with an electron subcycle timestep of 5×10^{-10} seconds. This results in a sampling time of 4 ms, or around 40 breathing-mode periods. The HPHall simulations use approximately 300,000 particles over the domain shown in Figure 1.8, where the domain consists of 1,530 quadrilateral cells. All simulations are run in serial on a 2.67 GHz Intel Core 2 CPU, resulting in a computational walltime of around 10 and 13 hours for H2 and H3, respectively.

3.1.2.1 Velocity Distributions and Fluxes

Three different types of velocity distribution function (VDF) and flux data are examined in this section. These data are presented for two reasons. First, the differences between H2 and H3 are most readily apparent in their calculation of heavy

species properties. Second, the heavy species inflow conditions have a significant impact on MPIC plume simulations, thus detailing the differences between H2 and H3 provides a basis to understand the effect that utilizing either H2 or H3 has on plume structure.

In this section, VDF at various axial stations within the acceleration channel are presented and analyzed. Next, constant-radius velocity and flux data along the acceleration channel centerline between the anode and TE plane are presented and analyzed. Finally, velocity and flux data at an axial station corresponding to the TE plane are presented and analyzed.

VDF are extracted from H2 and H3 by sampling macroparticles over a volume. In order to extract VDF that accurately represent the plasma near the channel centerline, sampled volumes are chosen as follows: the TE plane was divided into three segments, S_1, S_2, and S_3, with the middle segment, S_2, centered on the acceleration channel centerline. The volume is then determined by the cells adjacent to the middle segment. Macroparticles in this volume are sampled while the simulation results are time-averaged. VDF are then formed by binning the sampled particles. Figure 3.2 illustrates the extraction lines that are used to make comparisons between each model, and additionally illustrates the location of S_1, S_2, and S_3.

Figure 3.3 shows axial-direction VDF extracted at the TE plane from H2 and H3 simulations. There are two primary differences between H2 and H3 calculations: first, there is a population of high-velocity neutrals in the H3 calculation; second, the H3 simulations calculate a higher bulk velocity for the ions when compared to the H2 simulations. The high-velocity population of neutrals is a clear result from the introduction of a DSMC algorithm for collisions: CEX collisions directly affect individual neutrals instead of evenly distributing collision effects across the entire population. Therefore, a distinct population of high-velocity neutrals is observed.

The increased axial bulk velocity calculated for Xe^+ and Xe^{2+} occurs for two rea-

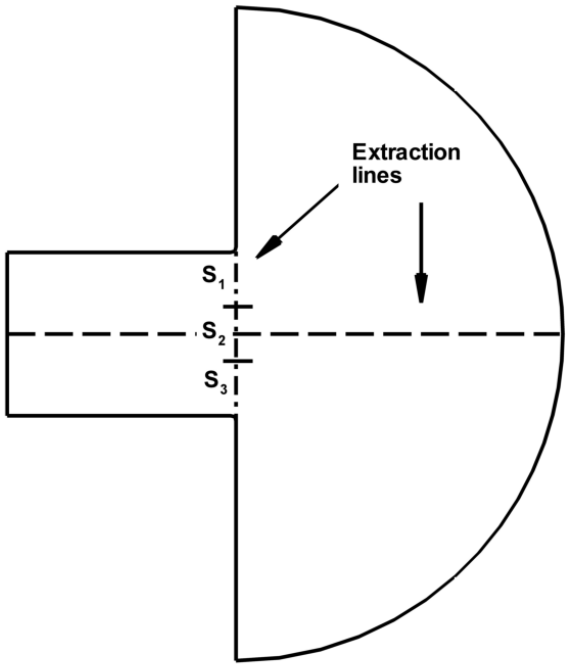

Figure 3.2: Extraction lines utilized in internal thruster comparisons.

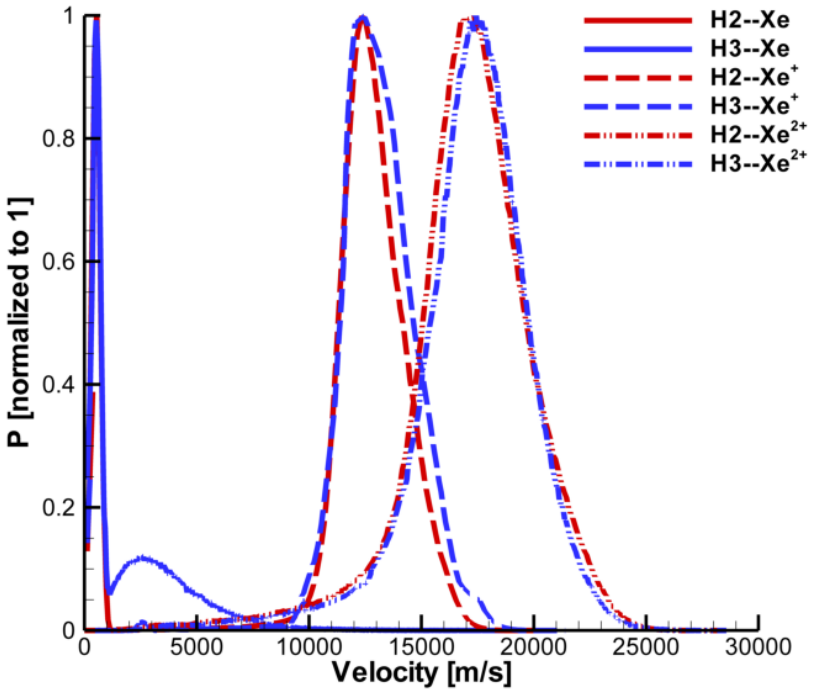

Figure 3.3: H2 and H3 calculations of axial-direction VDF at the TE plane for Xe, Xe^{+}, and Xe^{2+} species.

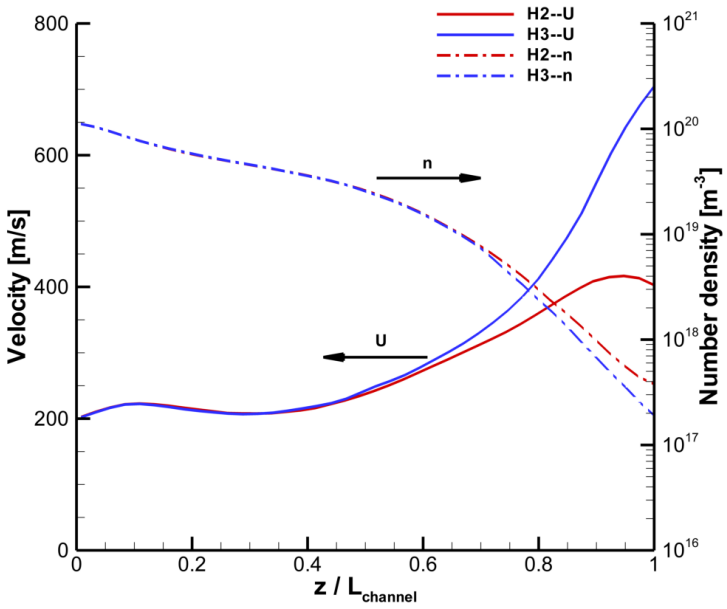

Figure 3.4: H2 and H3 calculations of number density and axial bulk velocity along the channel centerline for Xe.

sons. First, since H3 simulations calculate post-collision scattering angles based on the empirical data fit shown in Section 2.2.4.2, low-angle scattering is much more probable than scattering occurring at larger angles. The MCC method does not weight scattering toward low-angles and instead samples randomly. Therefore collisions modeled in H2 will on average scatter at higher angles, affecting the axial bulk velocity of ions to a greater extent. Second, the time-invariant continuity equation can be applied directly since: *i*) H2 and H3 calculate time-averaged steady state solutions, and *ii*) the region under consideration is constant area. The mass flow rate of neutrals from the anode is held constant at 20 $\frac{mg}{s}$. Therefore, since CEX collisions increase the bulk velocity of neutrals, the neutral number density at corresponding locations should decrease. Both H2 and H3 model ionization processes by assuming ionization rates directly proportional to neutral number density (see Eqn. (2.18)). Since H3 predicts a drop in the number of neutrals available for ionization, there is a corresponding drop in ion number density.

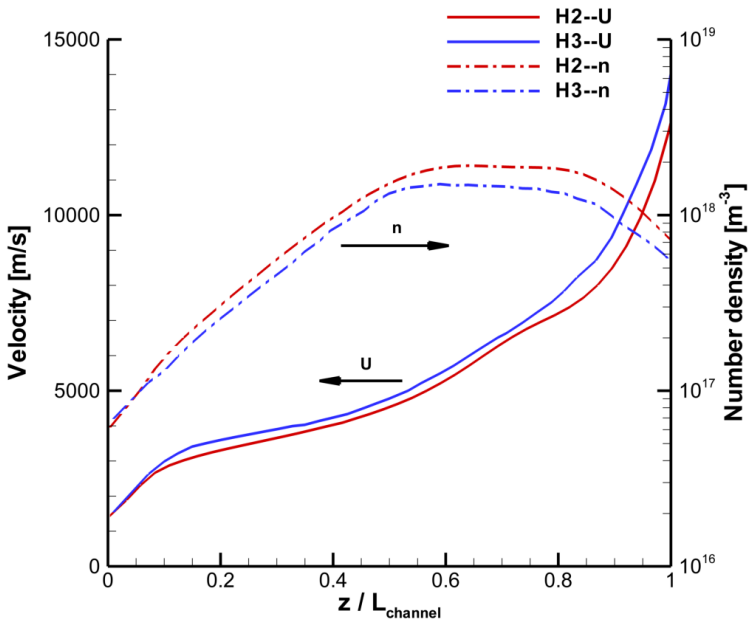

Figure 3.5: H2 and H3 calculations of number density and axial bulk velocity along the channel centerline for Xe^{+}.

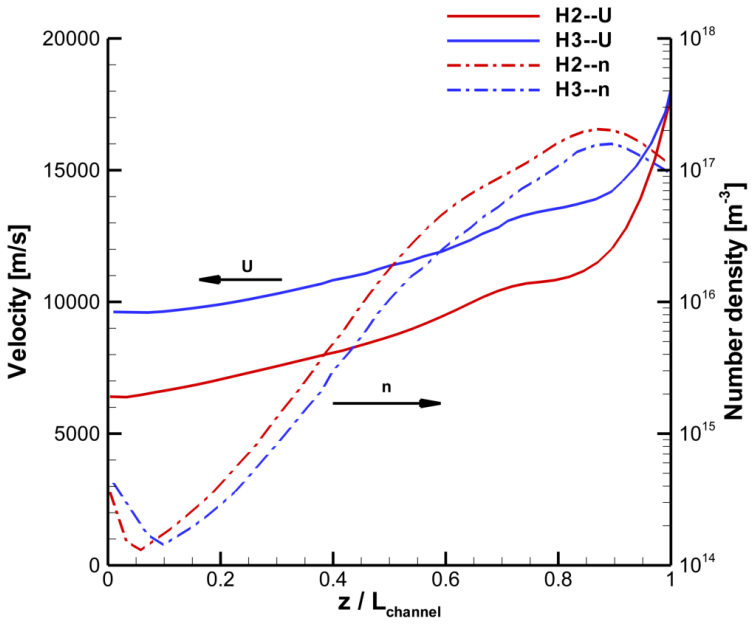

Figure 3.6: H2 and H3 calculations of number density and axial bulk velocity along the channel centerline for Xe^{2+}.

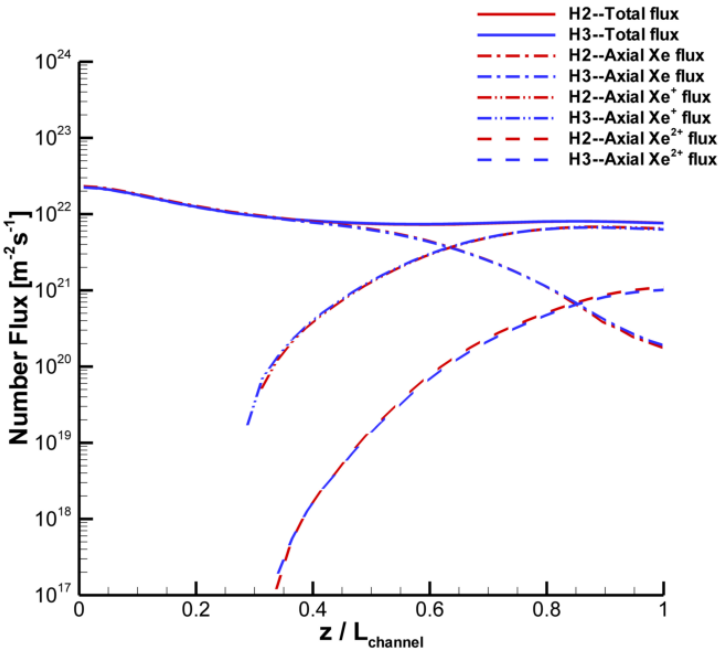

Figure 3.7: H2 and H3 calculations of number flux along the channel centerline for Xe, Xe^{+}, Xe^{2+}, and total number flux.

This behavior is also exhibited in the variation in number densities and bulk velocities along the acceleration channel centerline. Figures 3.4, 3.5, and 3.6 show axial variations in number density and bulk velocity for each species. Note that axial locations have been normalized by the length of the channel such that the TE plane is located at $z/L_{channel} = 1$. Relative to H2, calculated bulk velocities in H3 are typically higher and calculated number densities are typically lower, with the maximum difference occurring at the TE plane. Since the MPIC simulations in the present work depend on the number densities and velocities at the TE plane calculated by HPHall, plume simulations utilizing inflow conditions based on H2 vary significantly from plume simulations utilizing conditions based on H3.

The data in Figures 3.4, 3.5, and 3.6 are used to determine axial variations in number flux for each species. Figure 3.7 shows the variation along the channel centerline of Xe, Xe^{+}, Xe^{2+}, and total number flux. Note that axial-direction fluxes are shown because they are, generally, at least two orders of magnitude greater than

radial direction fluxes for $z/L_{channel} < 1$. Figure 3.7 illustrates the make-up of the mass flow inside the acceleration channel between the anode and the TE plane: the mass flow begins solely made up of neutrals. Moving away from the anode, the flow diverges slightly, decreasing the axial component of the total number flux. Continually moving toward the TE plane, first Xe^{+} and then Xe^{2+} begin to constitute larger fractions of the total mass flow. Finally, at the TE plane, the mass flow is made up primarily of Xe^{+}, followed by Xe^{2+} and Xe. Comparing calculated number fluxes between H2 and H3 illustrates that the same general trends are captured, although there are small variations in the individual species components. These variations are due primarily to the difference in neutral number density: H3 calculates a smaller neutral number density relative to H2, lowering the ionization rate relative to H2. The lower ionization rate results in a lower ion number density calculated relative to H2. The end result is a small difference in the contribution of each species to the total mass flow; however, the variations in mass flow fraction are all less than 7%. Further discussion of this result is provided in 3.1.2.2.

As stated above, there are significant differences in predicted values at the TE plane, i.e. $z/L_{channel} = 1$. The TE plane is one of the locations where information calculated in HPHall is utilized in MPIC. Figures 3.8, 3.9, and 3.10 show the variations in number density and axial bulk velocity at the TE plane for each species. Note that the radial coordinate has been normalized to vary between $r/W_{channel} = 0$ at the inner wall of the acceleration channel and $r/W_{channel} = 1$ at the outer wall of the acceleration channel. The same trends discussed above are illustrated in these data: axial bulk velocities calculated by H3 generally are increased relative to H2, and number densities calculated by H3 are generally decreased relative to H2. Although the increase in bulk velocity is greatest in Xe, this is slightly misleading: axial bulk velocity is calculated by averaging the axial velocity of macroparticles in a given region. As seen in Figure 3.3, there is a distinct population of high velocity neutrals

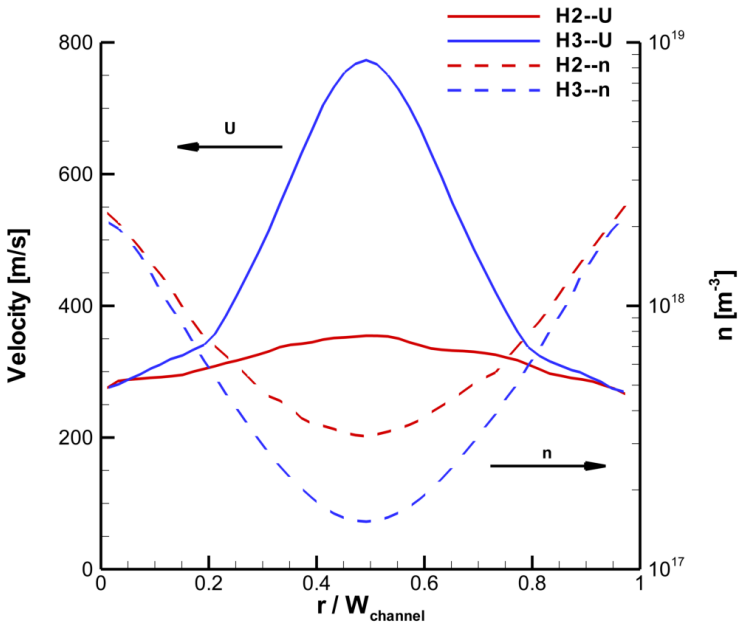

Figure 3.8: H2 and H3 calculations of number density and axial bulk velocity at the TE plane for Xe.

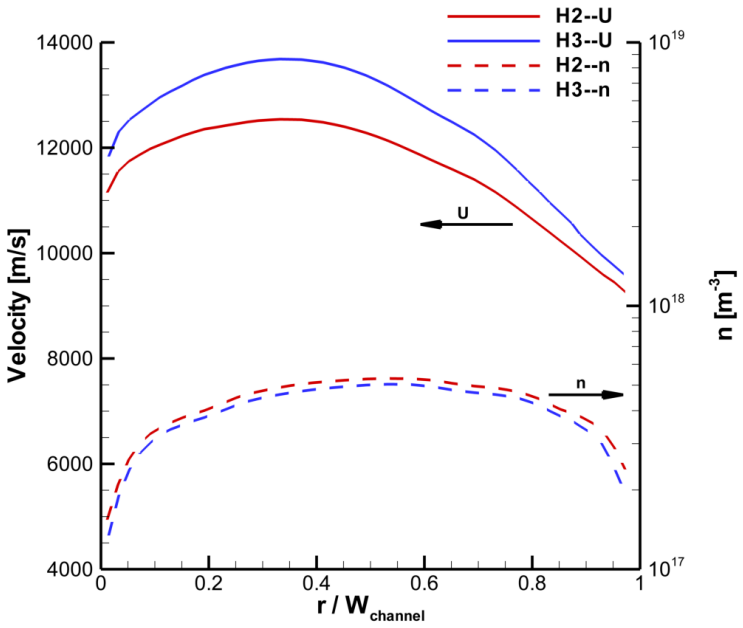

Figure 3.9: H2 and H3 calculations of number density and axial bulk velocity at the TE plane for Xe^{+}.

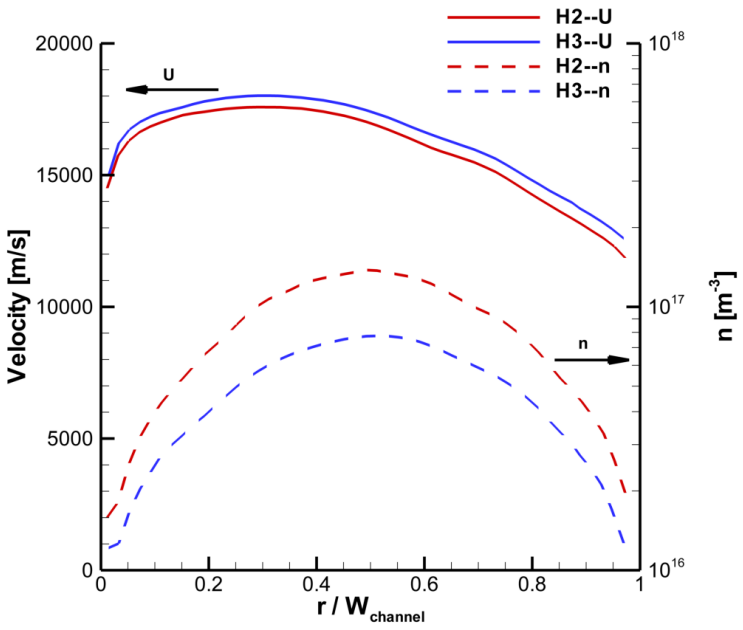

Figure 3.10: H2 and H3 calculations of number density and axial bulk velocity at the TE plane for Xe^{2+}.

near the center of the TE plane. This alters the calculation of bulk velocity to the point that it is no longer well-defined as a velocity at which the bulk of the particles in a given population are moving. However, given that the sole difference between Xe VDF calculated by H2 and H3 is the high-velocity tail calculated by H3, comparing axial bulk velocities links statistical and macroscopic effects.

3.1.2.2 Plasma Properties

In this section, three different plasma properties are shown in order to further examine the effect of the collision model in H3 relative to H2: ion number density, electron temperature, and plasma potential. Axial variations along the acceleration channel centerline between $z/L_{channel} = 0$ and $z/L_{channel} = 2$ for each property are presented. Note that the region of consideration in this case extends beyond the TE plane since experimental data for these properties are available up to $z/L_{channel} = 2$.

Figure 3.11 shows the axial variation of ion number density and ion production

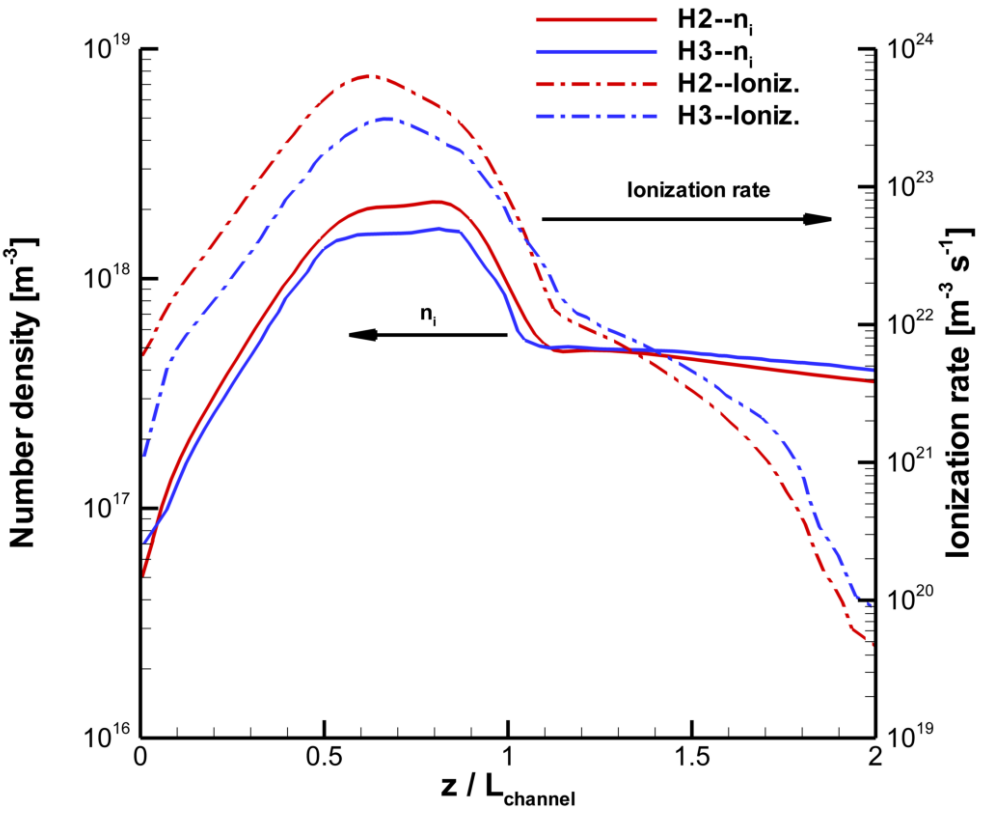

Figure 3.11: H2 and H3 calculations of ion number density and ion production rate along the channel CL.

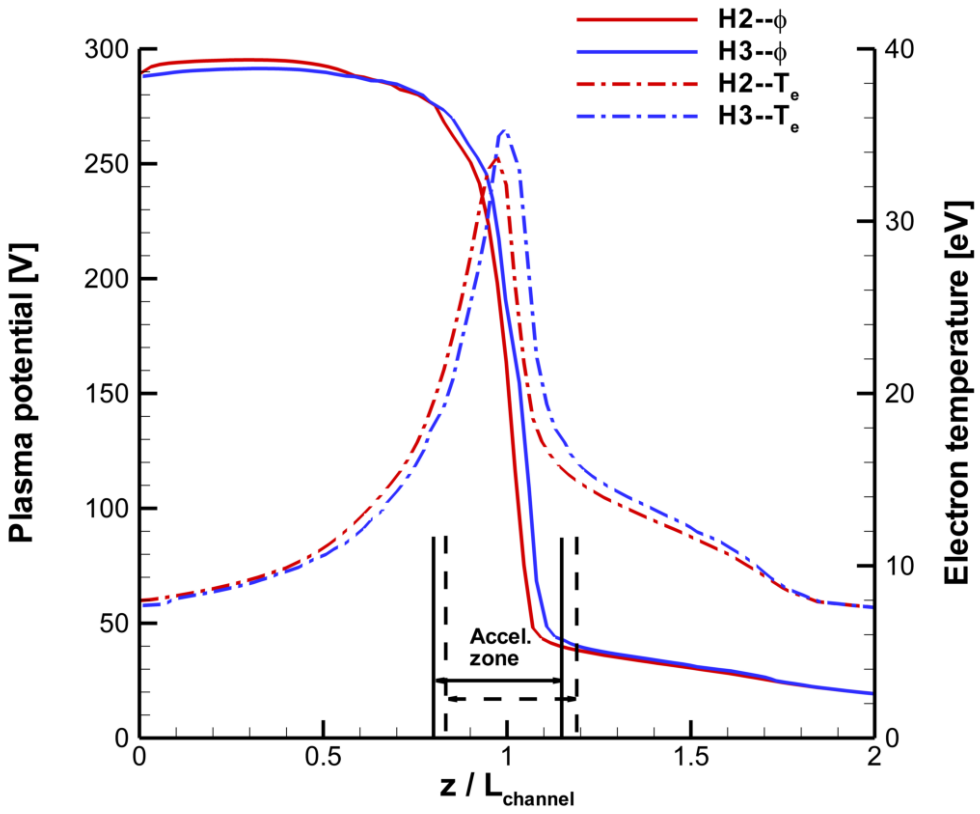

Figure 3.12: H2 and H3 calculations of plasma potential and electron temperature along the channel CL.

rate as calculated by H2 and H3. H2 and H3 both assume quasineutrality, i.e. the electron number density is identical to ion number density, therefore variations in ion number density correspond to variations in electron number density. Moving from anode to TE plane, collision effects become more prevalent and thus the difference in calculated electron number density between H2 and H3 is more perceptible. Inside the acceleration channel, H3 calculates a lower electron number density relative to H2 due to the same continuity considerations covered in Section 3.1.2.1.

Figure 3.12 shows the axial variation of plasma potential and electron temperature as calculated by H2 and H3. Relative to H2, H3 calculates qualitatively similar profiles for plasma potential and electron temperature. However, the collision submodel in H3 produces two visible differences: first, the plasma potential and electron temperature profiles are slightly shifted downstream, about 2% of the length of the channel; second, the electron temperature profile has a slightly higher peak, about 7% higher than the peak calculated by H2.

The difference in axial location when comparing H3 to H2 is essentially a shift in the primary ionization/acceleration zone, where this region is generally bounded by locations at 50% of the peak electron temperature, i.e. full-width at half-maximum (FWHM). Figure 3.12 marks this out for H2 using solid lines, whereas the H3 zone is marked with dashed lines. The shift is attributed to the decreased electron number density. Since calculated electron number density in H3 is decreased relative to H2, there is a corresponding decrease in plasma potential calculated according to Eqn. (2.20). However, downstream of the TE plane, the electron number density calculated by H3 is comparable to that calculated by H2. This is an effective downstream shift of the primary ionization/acceleration zone, with more ionization and acceleration occurring outside the acceleration channel relative to H2.

The shift in the primary ionization zone is shown in electron temperature calculations as well. Electron temperature is calculated by integration of the electron energy

conservation equation. The source terms for this are a function of electric field (and thus the potential) and ionization rate. As seen in Figures 3.11 and 3.12, both of these profiles are shifted. Therefore, H3 calculates a shifted profile, effectively pushing the ionization zone further downstream. The difference in peak electron temperature is a result of this dependence as well: Figure 3.11 shows that the ionization rate calculated in H3 is slightly higher downstream of the TE plane relative to H2, leading to a relative increase in peak electron temperature.

3.1.3 Discussion

The difference in collision dynamics models between H2 and H3 is most readily apparent in two data sets: *i*) Xe VDF at $z/L_{channel} = 0.9$ and $z/L_{channel} = 1$, and *ii*) plasma potential and electron temperature along the channel CL. The difference in calculated Xe VDF is directly dependent on the collision models in H2 and H3, as described in detail in Section 3.1.2.1, whereas the differences in calculated plasma potential and electron temperature are indirect results of collision model differences, as described in detail in Section 3.1.2.2. Since ion-atom collisions are more prevalent for $z/L_{channel}$ from 0 to 1, the different collision models calculate marginally different results at the TE plane. Plume simulations utilize these calculations at the TE plane, therefore, in the next section, the H2 and H3 results are compared to experimental measurements in order to determine which model should be used.

3.2 Assessing H2 and H3 Via Experimental Data

In this section, H2 and H3 calculations of heavy species' VDF and plasma properties are compared to experimental measurements. The 6 kW Hall thruster under consideration has been throughly characterized experimentally by the University of Michigan's PEPL [8, 9, 10, 74, 75], and all experimental measurements that are compared against in the present study were provided by the lab.

This section is divided into two parts. First, Xe and Xe^+ VDF comparisons at two axial stations along the acceleration channel centerline are shown. Second, constant-radius profiles of two plasma properties are presented.

3.2.1 Comparing Simulated VDF Results to Experimental Measurement

Experimental measurements of Xe and Xe^+ axial-direction VDF were performed by Huang [9, 10]. Velocimetry measurements were acquired using LIF as outlined in Section 1.1.2.4, such that Xe and Xe^+ populations are characterized at several axial locations. The associated error for these measurements is ± 50 m/s or $\pm 2\%$, whichever is greater. All VDF data presented here are calculated or measured along the acceleration channel centerline. VDF data are presented at two different axial stations, namely at 90% of the length of the channel ($z/L_{channel} = 0.9$) and at the TE plane ($z/L_{channel} = 1$).

It should be noted that, since populations near the tails of each VDF are more scarcely populated, spontaneous emissions are correspondingly less frequent and therefore more difficult to measure. Emissions eventually becomes infrequent enough to drop below the signal-to-noise ratio (SNR). Measurements with an intensity lower than the SNR cannot be definitively attributed to the observed region of the population. To illustrate this in the presented VDF data, probabilities under a certain minimum threshold value are not plotted. After the VDF peak has been normalized to 1, the minimum threshold value for the VDF data presented here is set to 0.05 (arbitrary units). This is relatively conservative: some of the measured data appear consistently noisy between probabilities of 0.1-0.2. Therefore, setting the threshold to 0.05 will filter out the most obviously spurious measurements.

Figures 3.13, 3.14, 3.15, and 3.16 show VDF comparisons between H2, H3, and experimental measurements for Xe and Xe^+. Beginning with the neutral atom VDF, the experimental measurements show that the most probable axial velocity of Xe

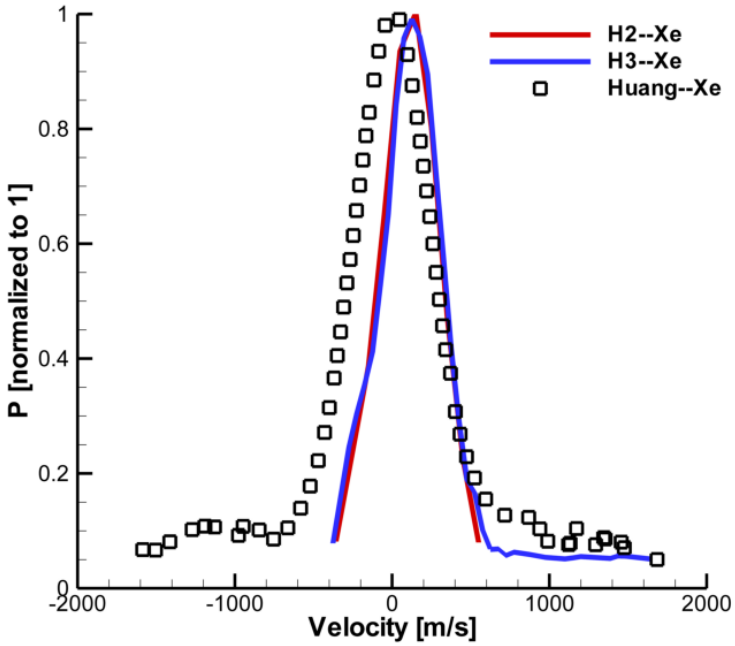

Figure 3.13: Comparisons between HPHall calculations and experimental measurements of axial-direction VDF of Xe at $z/L_{channel} = 0.9$.

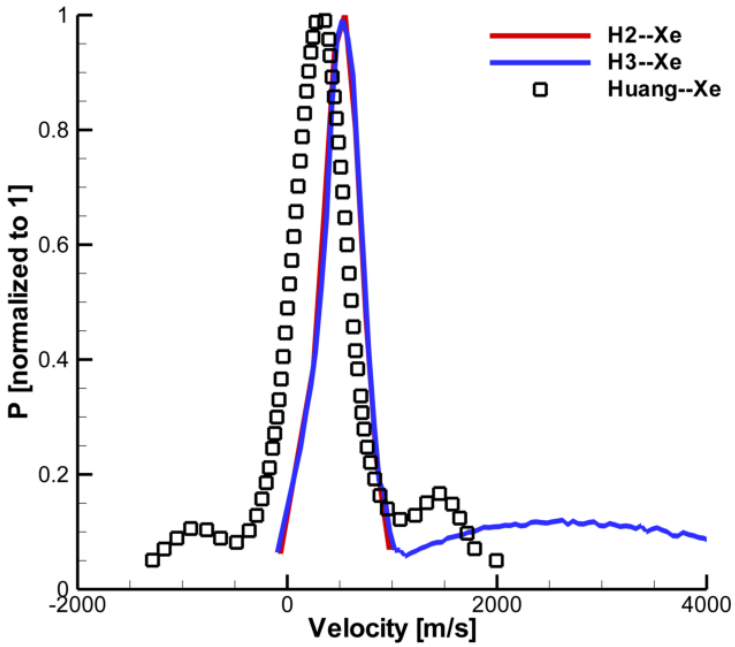

Figure 3.14: Comparisons between HPHall calculations and experimental measurements of axial-direction VDF of Xe at $z/L_{channel} = 1$.

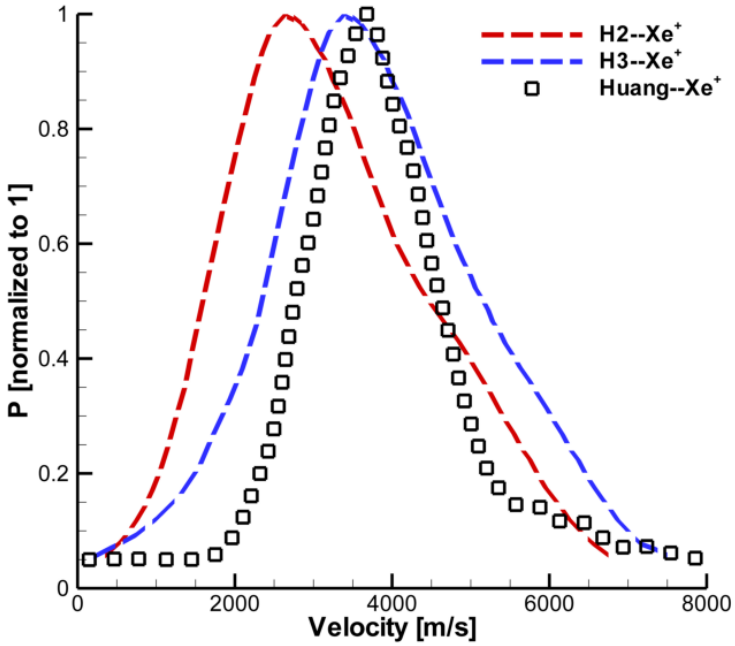

Figure 3.15: Comparisons between HPHall calculations and experimental measurements of axial-direction VDF of Xe^+ at $z/L_{channel} = 0.9$.

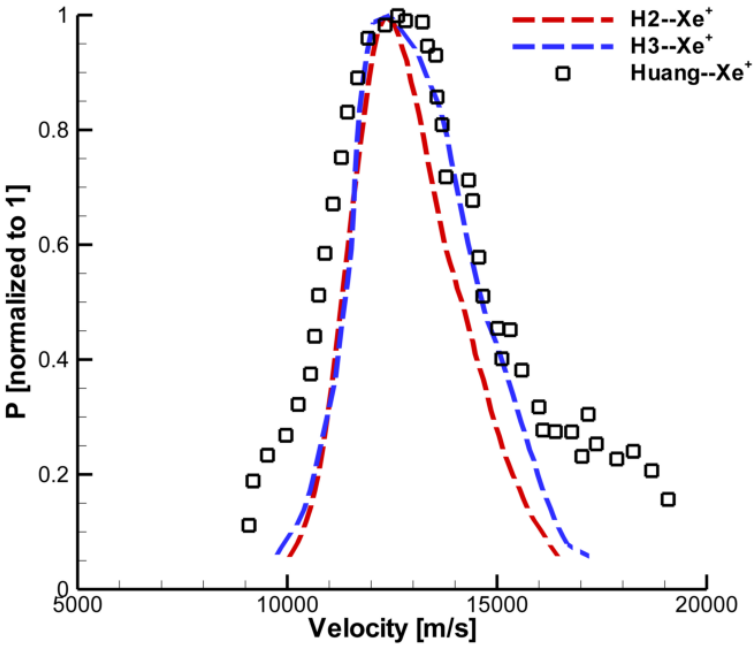

Figure 3.16: Comparisons between HPHall calculations and experimental measurements of axial-direction VDF of Xe^+ at $z/L_{channel} = 1$.

increases regularly as $z/L_{channel}$ increases from 0.9 to 1. The measured most-probable axial velocity is approximately 70 m/s lower than the most-probable velocity calculated by H2 and H3 at $z/L_{channel} = 0.9$, whereas the measured most-probable axial velocity is approximately 110 m/s lower than the calculated most-probable velocity at $z/L_{channel} = 1$. The FWHM of the VDF at $z/L_{channel} = 0.9$ is measured at around 600 m/s, whereas H2 and H3 both calculate FWHM of around 400 m/s at the same location. Note that, assuming a Maxwellian VDF, the previously mentioned FWHM correspond to temperatures of 600 K and 400 K. At $z/L_{channel} = 1$, the measured FWHM of the VDF is still around 600 m/s, whereas the simulations show an increase to 480 m/s. Excepting the discrepancy in most-probable velocity measurement and prediction, the qualitative comparisons are good: H2, H3, and measured data all show a Xe population primarily consisting of a near-Maxwellian distribution at both axial stations. Further, the measured VDF at the TE plane shows the presence of a high-velocity population of Xe, between 1000 and 2000 m/s. Due to its scattering model, H2 does not resolve a population of Xe in this region. However, this is the same region in which H3 calculates a significant population of Xe, and although the probability is measured to be approximately twice as large as the calculated probability for the same region, Section 3.1 demonstrated that this population has a significant effect on plasma properties.

The Xe^+ VDF comparisons exhibit similar trends in most-probable axial velocity. The most-probable velocity calculated by H3 corresponded well with the measured velocity: at $z/L_{channel} = 0.9$, the most-probable velocity calculated by H3 is 350 m/s less than the measured value, and at $z/L_{channel} = 1$, the velocity calculated by H3 is 330 m/s greater than the measured value. This comes out to differences of -9% and +2.5% for $z/L_{channel} = 0.9$ and $z/L_{channel} = 1$, respectively. The most-probable velocity calculated by H2 also corresponded well with the measured velocity: at $z/L_{channel} = 0.9$, the most-probable velocity calculated by H2 is 1000 m/s less than

the measured value, and at $z/L_{channel} = 1$, the most-probable velocity calculated by H2 is 200 m/s greater than the measured value. These are differences of -27% and +1.5% for $z/L_{channel} = 0.9$ and $z/L_{channel} = 1$, respectively. H3 showed better agreement with the measured most-probable velocity at the axial station upstream of the TE plane, but both H2 and H3 were very close to the measured velocity at the TE plane. The FWHM of the VDF at $z/L_{channel} = 0.9$ is measured at around 1900 m/s, whereas H2 calculates a FWHM of 3000 m/s, and H3 calculate FWHM of around 2900 m/s. At $z/L_{channel} = 1$, the measured FWHM of the VDF increases to around 4400 m/s, whereas the simulations show an increase to 3100 m/s and 3600 m/s for H2 and H3 respectively. The qualitative comparisons between VDF also show good agreement: H2, H3, and measurements show the Xe^+ VDF has a positive skewness. This indicates the presence of a high-velocity tail in the VDF. There is some discrecpancy between HPHall and the measured data in the width of the VDF: at $z/L_{channel} = 0.9$, both H2 and H3 calculate VDF significantly wider than the measured data, indicating that the kinematic compression of the measured VDF is not resolved by HPHall; however, at $z/L_{channel} = 1$, both H2 and H3 calculate VDF in better agreement with the measured data, with the main discrepancy in the amount of skewness exhibited. The skewness in the Xe^+ VDF has been attributed to $Xe^+ - Xe^{2+}$ CEX collisions [10]; however, this type of collision is not modeled in H2 or H3, and the skewness calculated by those models is attributed to the relationship between ion number density and plasma potential: ion number density and ionization rate both peak at locations between $z/L_{channel} = 0.7 - 0.8$, therefore more ions than not are accelerated by the full potential drop, resulting in a high velocity population that skews the calculated VDF.

3.2.2 Comparing Simulated Plasma Properties to Experimental Measurement

Experimental measurements of ion number density, electron temperature, and plasma potential were performed by Reid [8]. Ion number density and electron temperature measurements were acquired using a Langmuir probe, whereas plasma potential measurements were acquired using a floating emissive probe in conjunction with the electron temperature measurements taken by the Langmuir probe, as outlined in Section 1.1.2.4. The associated error for these measurements is between $2-300\%$ on the number density, and $\pm(5\ V\ +\ 0.9\ T_e)$ on the plasma potential. All of the plasma property data presented here are either calculated or measured along the acceleration channel centerline, between the anode ($z/L_{channel}\ =\ 0$) and twice the length of the acceleration channel ($z/L_{channel}\ =\ 2$). Note that the ion number density data presented are derived using a "blended" analysis of the ion saturation current, utilizing both thin-sheath and thick-sheath analyses. This is the most rigorous data analysis available; see Ref. [8] for details.

Figure 3.17 shows plasma number density comparisons between H2, H3, and measured data. Note that HPHall simulations assume quasineutrality, therefore the calculations of the axial variation of ion number density are identical to calculations of electron or plasma number density. Near $z/L_{channel}\ =\ 0.6-0.8$, there is a significant discrepancy between the magnitude of the peak measured density and the magnitude of peak calculated density: the difference between measurements and H2 is -51% relative to the measured peak, and the difference between measurements and H3 is -65% relative to the measured peak. This discrepancy persists beyond $z/L_{channel}\ =\ 0.6$ to the edge of the domain. However, this discrepancy is at or near the expected uncertainty generally associated with this kind of measurement, and it is well within the uncertainty for this particular case. Due to the unknown source of high uncertainty in the measurements, only qualitative assessments can be made using plasma number

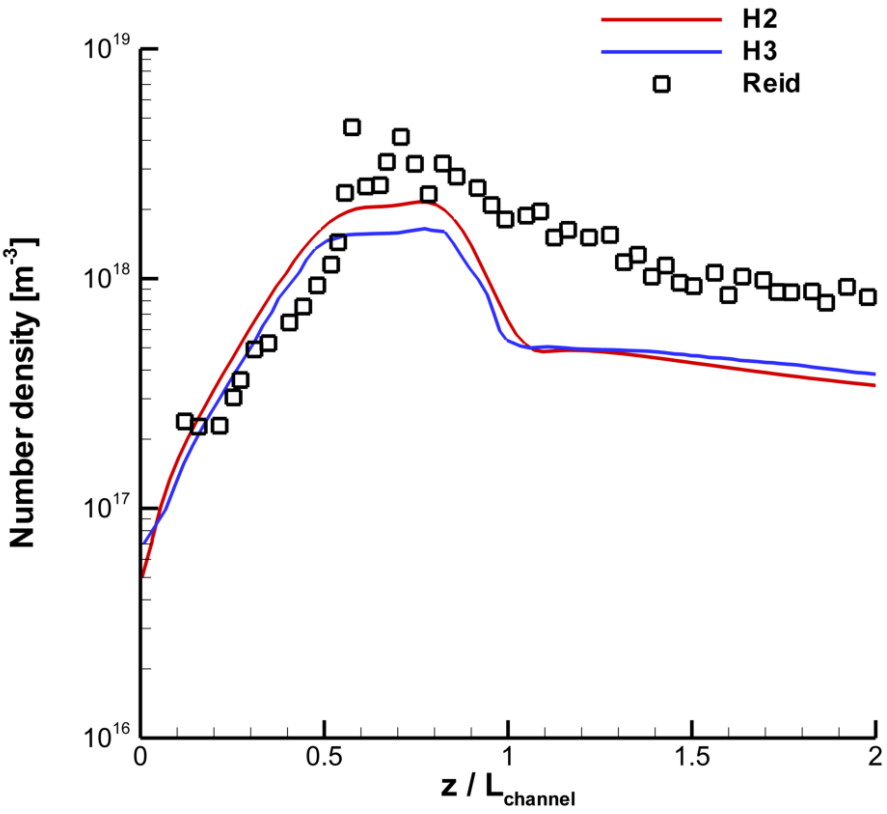

Figure 3.17: Comparisons between HPHall calculations and experimental measurements of plasma number density along the channel CL.

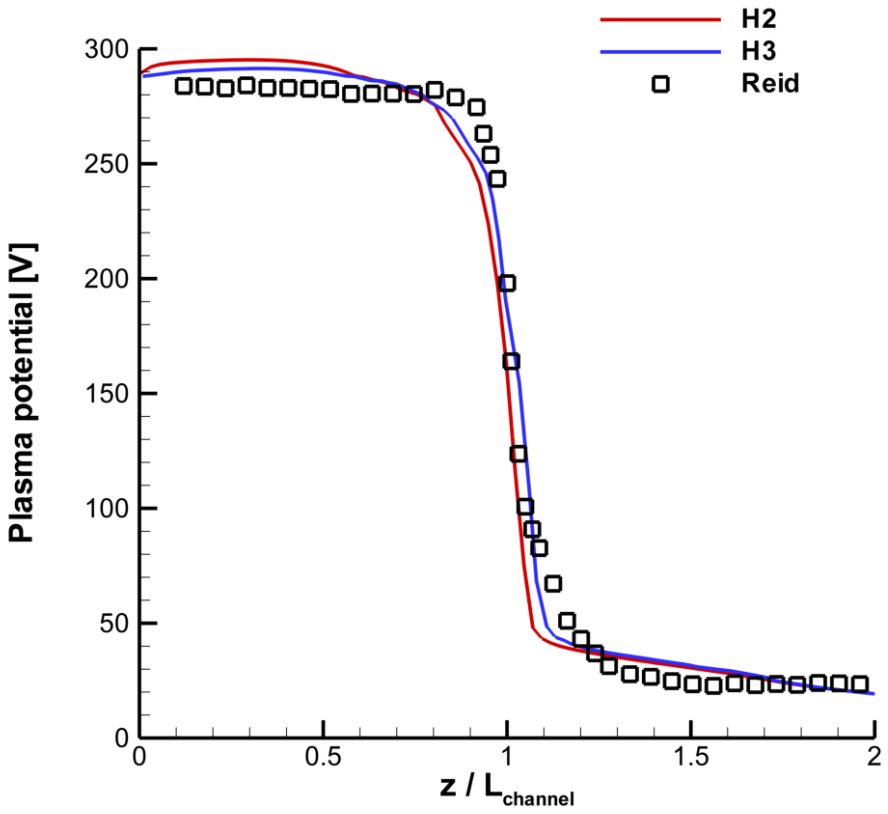

Figure 3.18: Comparisons between HPHall calculations and experimental measurements of plasma potential along the channel CL.

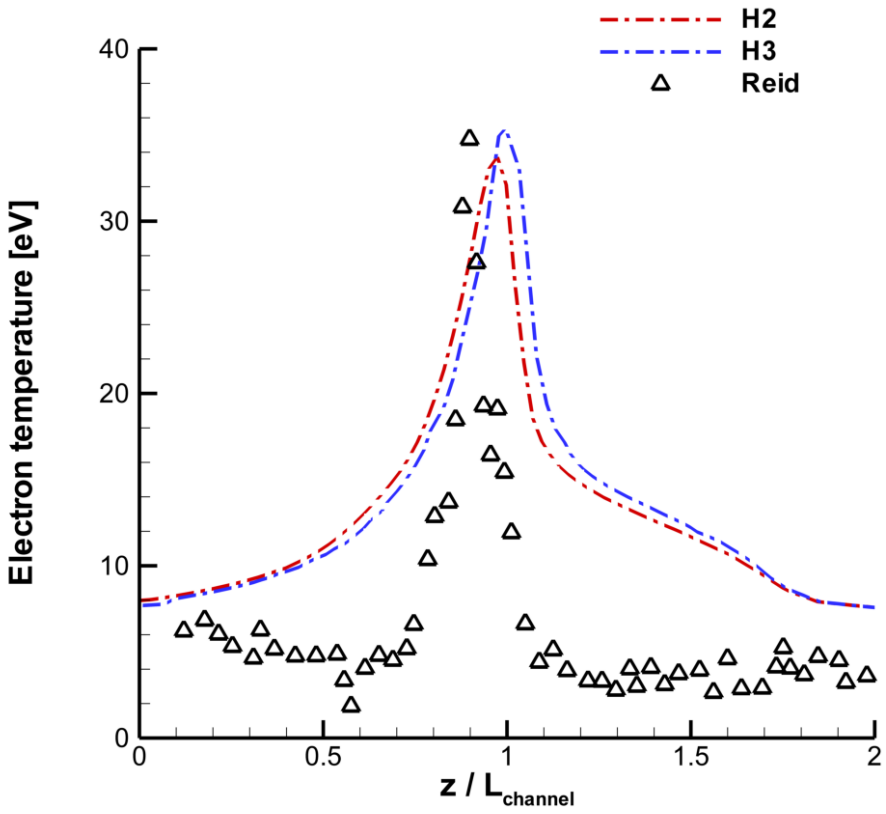

Figure 3.19: Comparisons between HPHall calculations and experimental measurements of electron temperature along the channel CL.

density. Overall trends in the plasma number density calculated by H2 and H3 correspond well with measurements: the density increases to a peak magnitude between $z/L_{channel} = 0.6 - 0.8$ before monotonically decreasing as $z/L_{channel}$ approaches 2.

Figures 3.18 and 3.19 show comparisons of plasma potential and electron temperature between H2, H3, and measured data. Starting with the plasma potential comparisons, both H2 and H3 show good agreement with measured potentials: the qualitative features of the measurements are all resolved in the HPHall simulations. It has been previously noted that H2 shows good agreement with plasma potential measurements [8], with the only discrepancy being a small upstream shift (5% $L_{channel}$) in the simulated profile. The profile calculated by H3 shows a profile shift approximately 2% $L_{channel}$ downstream, predicting an acceleration zone closer to the region determined by measurements. There is, however, a persisting discrepancy between HPHall simulations and measurements in the magnitude of the gradient in plasma potential: both H2 and H3 predict a more smoothly varying plasma potential through the acceleration zone than the measured profile. There are two possible explanations for this. First, the measurements presented in Figure 3.18 are corrected using electron temperature measurements. This adds an additional source of uncertainty to the measurements, and the uncertainty associated with the corrections scales with the electron temperature data used to correct the raw data. The net effect of this is illustrated in a close up of the acceleration zone in Figure 3.20: since electron temperature peaks in the acceleration zone, the largest error in measurements occurs in the acceleration zone as well. Figure 3.20 shows that the additional uncertainty has the effect that some calculations in potential via H2 and H3 are within the error bars after the raw data is corrected. Another possible explanation for the difference in gradient magnitude is the HPHall electron submodel: plasma potential is calculated in part by utilizing the Boltzmann relation. This method has been shown to artificially smooth gradients in plasma potential due its mathematical form [25].

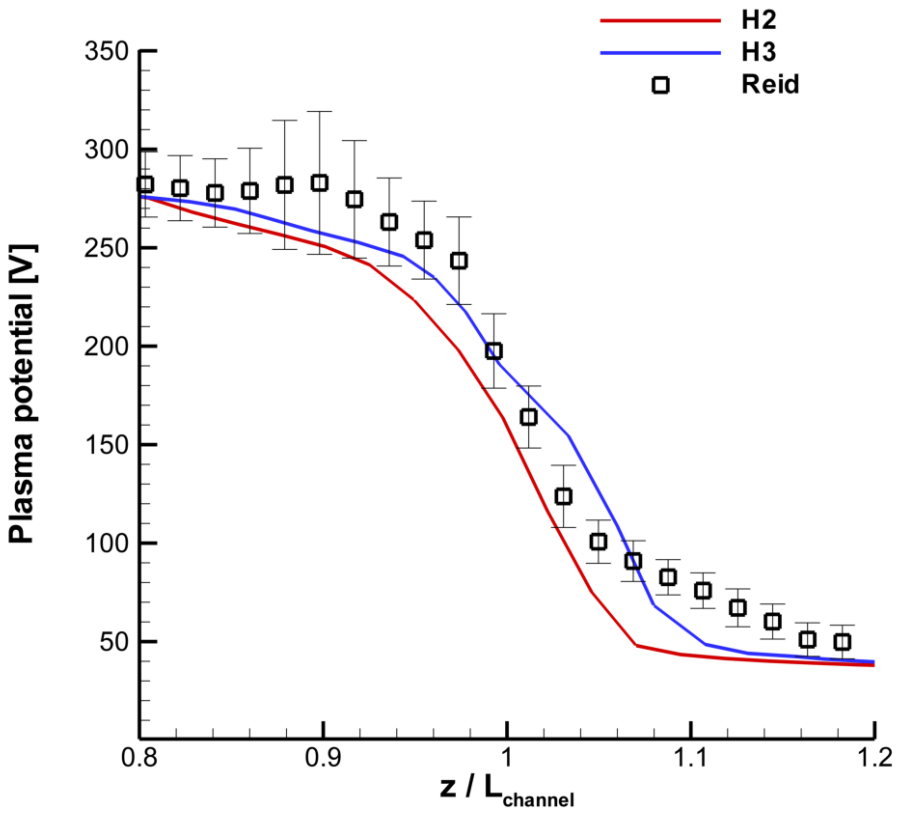

Figure 3.20: Comparisons between HPHall calculations and experimental measurements of plasma potential, including associated error bars: close-up of the acceleration zone.

The electron temperature comparisons between H2, H3, and the measured data did not agree as closely as the plasma potential comparisons. Peak electron temperature calculation using H2 and H3 agreed with measured data well: the difference between measurements and H2 is -3% relative to the measured peak, and the difference between measurements and H3 is +5% relative to the measured peak. However, the location of peak electron temperature was consistently calculated to be downstream of the measured peak. The measured location of peak electron temperature is $z/L_{channel} = 0.95$, whereas H2 calculates a peak temperature location of $z/L_{channel} = 1.02$ and H3 calculates a peak temperature location of $z/L_{channel} = 1.05$. Further, outside of $z/L_{channel} = 0.9 - 1.02$ the electron temperature calculated by H2 and H3 is consistently overpredicted by anywhere from 30-300%. Though some of this difference stems from the difference in calculated and measured location of peak temperature, there is still a large discrepancy. One explanation for this is the HPHall electron submodel: electron temperature is calculated by integrating the electron energy equation. In order to simplify this integration numerically, the source term of the energy equation is solved for by utilizing the Boltzmann relation. This artificially limits the range over which the source term can vary, limiting the range of calculated electron temperatures. The initial conditions are set such that the peak electron temperature is in good agreement with measurements, but at the cost of overprediction upstream and downstream of the peak temperature location.

3.2.3 Discussion

Based on results in Sections 3.1 and 3.2, there are moderate differences between H2 and H3 simulations, and these differences are traced back to the heavy species submodels they utilize. Due to the DSMC algorithm that constitutes the heavy species submodel in H3, H3 calculates VDF and plasma properties that agree with measurements more closely than the H2 counterparts. H3 VDF calculations for Xe

resolve the high velocity tail that is seen in LIF measurements (Figures 3.13 and 3.14), a VDF feature that is absent in H2 calculations. This difference in collision modeling has a traceable effect on various plasma properties that generally improved agreement between simulations and measured data (Figures 3.17, 3.18 and 3.19).

3.3 Extracted Inflow Conditions from HPHall

The final comparison of the heavy species submodels in H2 and H3 is performed using MPIC: plume simulations are run using inflow conditions extracted from both H2 and H3 calculations, the results of which are reported in Chapter 4. These plume simulations are compared against near- and far-field plasma property measurements in order to assess, in part, the viability of H2 and H3. In order to provide inflow conditions, heavy species and electron properties are extracted from H2 and H3 calculations. This section tabulates the inflow conditions calculated by H2 and H3. The TE plane inlet geometry is spatially discretized as follows: the TE plane is divided into three equal line segments in order to represent radial variation of inflow properties, and these segments are numbered starting with the segment farthest from the thruster centerline. Required inflow conditions for the heavy species submodel are described below in Section 3.3.1, followed by a description of inflow conditions required for the electron submodel in Section 3.3.2.

3.3.1 Heavy Species Inflow Conditions

MPIC requires the following parameters as inflow conditions for the heavy species submodel, where i ranges over each species that is modeled: $U_i,\ V_i,\ W_i,\ T_i,\ n_i$, where U, V, and W are in m/s, T is in K, and n is in m^{-3}. Note that in all extracted data, out-of-plane bulk velocity W is found to be zero, and so is not included in the tables. Additionally, segments are abbreviated such that the first segment, i.e. the line segment farthest from the thruster centerline, is labeled S_1, with subsequent

Species	Location	U, m/s	V, m/s	T, K	n, m^{-3}
Xe	S_1	305	155	590	1.82×10^{18}
	S_2	350	-10	600	4.96×10^{17}
	S_3	305	-155	590	1.80×10^{18}
Xe^+	S_1	9100	100	10400	4.59×10^{17}
	S_2	12300	-400	3200	5.11×10^{17}
	S_3	12500	-500	11100	3.95×10^{17}
Xe^{2+}	S_1	13800	-800	28300	6.11×10^{16}
	S_2	16900	-400	9900	1.35×10^{17}
	S_3	17150	-220	26500	5.10×10^{16}

Table 3.1: H2-extracted heavy species inflow parameters at the TE plane.

Species	Location	U, m/s	V, m/s	T, K	n, m^{-3}
Xe	S_1	420	190	900	7.80×10^{17}
	S_2	710	-40	2800	1.65×10^{17}
	S_3	425	-170	930	7.74×10^{17}
Xe^+	S_1	11000	100	14600	4.08×10^{17}
	S_2	13100	-360	4000	4.05×10^{17}
	S_3	12900	-500	12900	3.71×10^{17}
Xe^{2+}	S_1	16500	-870	30100	3.78×10^{16}
	S_2	17400	-400	11000	6.55×10^{16}
	S_3	17500	-220	29900	4.00×10^{16}

Table 3.2: H3-extracted heavy species inflow parameters at the TE plane.

segments labeled accordingly. The inflow parameters that are extracted from H2 are tabulated in Table 3.3.2, whereas the parameters extracted from H3 are shown in Table 3.3.2.

3.3.2 Electron Inflow Conditions

MPIC requires the following parameters as inflow conditions for the electron sub-model: ϕ, $\nabla\psi$, T_e. Note that $\nabla\psi$ is equivalent to electron current density normalized by the elementary charge, e. Segments are abbreviated as in Section 3.3.1. The inflow parameters that are extracted from H2 are tabulated in Table 3.3.2, whereas the parameters extracted from H3 are shown in Table 3.3.2.

Species	Location	ϕ, V	$\nabla\psi$, $m^{-2}\,s^{-1}$	T_e, eV
e^-	S_1	130	-5.08×10^{21}	35.6
	S_2	142	-6.89×10^{21}	33.2
	S_3	109	-6.27×10^{21}	31.4

Table 3.3: H2-extracted electron submodel inflow parameters at the TE plane.

Species	Location	ϕ, V	$\nabla\psi$, $m^{-2}\,s^{-1}$	T_e, eV
e^-	S_1	166	-5.24×10^{21}	32.5
	S_2	179	-7.01×10^{21}	31.1
	S_3	138	-6.48×10^{21}	29.8

Table 3.4: H3-extracted electron submodel inflow parameters at the TE plane.

CHAPTER IV

Plume Simulations Using Differential Cross Section Collision Dynamics

In this chapter, results of Hall thruster plume simulations are presented. The simulations are performed using the computer code MPIC in order to model the plasma plume of the 6 kW Hall thruster described in Chapter 3. The goal of this analysis is to accurately predict plume structure while maintaining relatively low computational cost. This goal is motivated by the role that plume structure plays in spacecraft integration: plume impingement has significant bearing on the failure mechanisms of certain spacecraft systems. As such, accurately predicting plume structure is a critical aspect of spacecraft design.

This chapter is divided into four sections. First, simulation boundary conditions are detailed. Second, MPIC results that utilize the inflow conditions calculated by H2 and H3 simulations are presented and compared to experimental data taken at PEPL and JPL in order to assess viability of the two different internal plasma models. Third, results from MPIC simulations utilizing the new colllision model (dubbed MPIC2) are compared to the previous version (dubbed MPIC1) in order to characterize the differences between post-collision scattering models as described in Section 2.2.4.2. Finally, these plume simulations are compared to experimental data in order to assess the accuracy of the two models. These comparisons are made by examining heavy

species properties in the near- and far-field.

4.1 Boundary Condition Outline

The thruster considered in the present study is a 6 kW Hall thruster, as shown in Section 1.1.2.3, with nominal operating conditions shown in Section 3.1.1. Thruster operation within the LVTF is modeled using the computational domain shown in Section 1.1.2.5. In order to simulate thruster operation, boundary conditions are required at the TE, outflow surfaces, the axis of symmetry, cathode, and along the thruster wall, for both the heavy species submodel and the electron submodel. Boundary conditions for the heavy species submodel are presented first, followed by those for the electron submodel.

Since macroparticles are injected according to a Maxwellian VDF, some of the macroscopic plasma properties are required at the inflow boundary, namely the number density, bulk velocity components, and the temperature of each heavy species in the simulation. The inflow boundary in this case is the TE plane, which is discretized into three regions as described in Section 3.3. The tabulated inflow properties listed therein are utilized for plume simulation. To determine particle properties at the cathode, the assumption is made that the mass flow consists solely of neutral xenon atoms. This assumption allows for a clear calculation of boundary conditions for the fluid electron model, as injecting xenon ions from the cathode creates a current density which feeds back into determination of the fluid boundary conditions. The neutrals are assumed to have a characteristic temperature of 1300 K [76]. The neutrals injected at the cathode are assumed to have sonic velocity, which, using the reported mass flow rate of 7% of the anode mass flow rate [8] and the cathode exit area, thereby determines the number density. The particle properties for species at the cathode are appended to the tabulated TE data in Tables 4.1 and 4.2.

There is only one solid surface that is modeled in the present analysis, namely the

Species	Location	U, m/s	V, m/s	T, K	n, m^{-3}
Xe	S_1	305	155	590	1.82×10^{18}
	S_2	350	-10	600	4.96×10^{17}
	S_3	305	-155	590	1.80×10^{18}
	Cathode	320	0	1300	1.78×10^{20}
Xe^+	S_1	9100	100	14000	4.59×10^{17}
	S_2	12300	-400	3200	5.11×10^{17}
	S_3	12500	-500	12200	3.95×10^{17}
	Cathode	0	0	0	0
Xe^{2+}	S_1	13800	-800	28300	6.11×10^{16}
	S_2	16900	-400	9900	1.35×10^{17}
	S_3	17150	-220	26500	5.10×10^{16}
	Cathode	0	0	0	0

Table 4.1: Heavy species inflow conditions at the TE plane and cathode. TE plane conditions extracted from H2.

Species	Location	U, m/s	V, m/s	T, K	n, m^{-3}
Xe	S_1	420	190	900	7.80×10^{17}
	S_2	710	-40	2800	1.65×10^{17}
	S_3	425	-170	930	7.74×10^{17}
	Cathode	320	0	1300	1.78×10^{20}
Xe^+	S_1	11000	100	14600	4.08×10^{17}
	S_2	13100	-360	4000	4.05×10^{17}
	S_3	12900	-500	12900	3.71×10^{17}
	Cathode	0	0	0	0
Xe^{2+}	S_1	16500	-870	30100	3.78×10^{16}
	S_2	17400	-400	11000	6.55×10^{16}
	S_3	17500	-220	29900	4.00×10^{16}
	Cathode	0	0	0	0

Table 4.2: Heavy species inflow conditions at the TE plane and cathode. TE plane conditions extracted from H3

Species	Location	ϕ, V	$\nabla\psi$, $m^{-2}\,s^{-1}$	T_e, eV
e^-	S_1	130	-5.075×10^{21}	35.6
	S_2	142	-6.894×10^{21}	33.2
	S_3	109	-6.270×10^{21}	31.4
	$Cathode$	4	3.251×10^{24}	3.0
	$Wall$	0	0	0
	$Symmetry$	0	0	0
	$Outflow$	0	0	3.0

Table 4.3: Electron submodel boundary conditions. TE plane conditions extracted from H2.

thruster itself. It is assumed to have a plasma potential of zero, i.e. to be electrically grounded. All ions that collide with the thruster wall are neutralized and reflect as outlined in Section 2.2.3.3, assuming full accommodation to a surface temperature of 300 K for the thruster wall. Finally, particles interacting with outflow surfaces are removed from the simulation.

The boundary conditions for the detailed-fluid model must be determined in order to solve the conservation equations shown in Section 2.3.2.2. Since each equation is Laplace-like, each one requires specification of either a Dirichlet (direct) value, or a von Neumann (gradient) value. Thus the plasma potential, the electron temperature, and the quantity $\nabla\psi$, i.e. $n_e v_{e,\hat{n}}$, are specified as either direct or gradient values at each boundary in the simulation. Each boundary condition is direct except for the following: *i*) each boundary condition for the axis of symmetry is a gradient-type condition, *ii*) the wall of the thruster has a gradient-type condition for the electron temperature, and *iii*) the outflow surface has a gradient-type condition for $n_e v_{e,\hat{n}}$ and ϕ. The value to which each is set is specified in Tables 4.3 and 4.4. Note that the TE plane is discretized into three regions as described in Section 3.3.

Due to the grounding of the thruster, the plasma potential condition is direct and set to zero for the thruster walls. At the TE plane and the cathode, the plasma potential is set to values from HPHall. The electron temperature is also set to char-

Species	Location	ϕ, V	$\nabla\psi$, $m^{-2}\,s^{-1}$	T_e, eV
e^-	S_1	166	-5.243×10^{21}	32.5
	S_2	179	-7.010×10^{21}	31.1
	S_3	138	-6.475×10^{21}	29.8
	$Cathode$	4	3.251×10^{24}	3.0
	$Wall$	0	0	0
	$Symmetry$	0	0	0
	$Outflow$	0	0	3.0

Table 4.4: Electron submodel boundary conditions. TE plane conditions extracted from H3.

acteristic values based on HPHall. The TE plane boundary condition for $n_e v_{e,\hat{n}}$ is determined using electron current density information from HPHall:

$$n_e v_{e,\hat{n}} \;=\; \frac{\vec{j_e}}{e} \tag{4.1}$$

The cathode boundary condition for $n_e v_{e,\hat{n}}$ is determined by the discharge current and cathode area as follows:

$$n_e \; v_{e,\hat{n}} \;=\; \frac{I_d}{e \; A_{cathode}} \tag{4.2}$$

In summary, the electron submodel boundary conditions utilized in this chapter are shown in Figure 4.1.

4.2 Plume Simulations Utilizing H2 and H3

The plume simulations presented in this section use the MPIC1 heavy species submodel as outlined in Section 2.2.4.2 and the detailed fluid electron submodel as outlined in Section 2.3.2.2. The plume simulation runs for 350,000 timesteps to reach a steady state and then for another 100,000 timesteps to sample macroscopic data. This results in a total of approximately 2.5 million particles at steady state over the domain shown in Figure 1.8, where the domain consists of 3,191 triangular cells. This

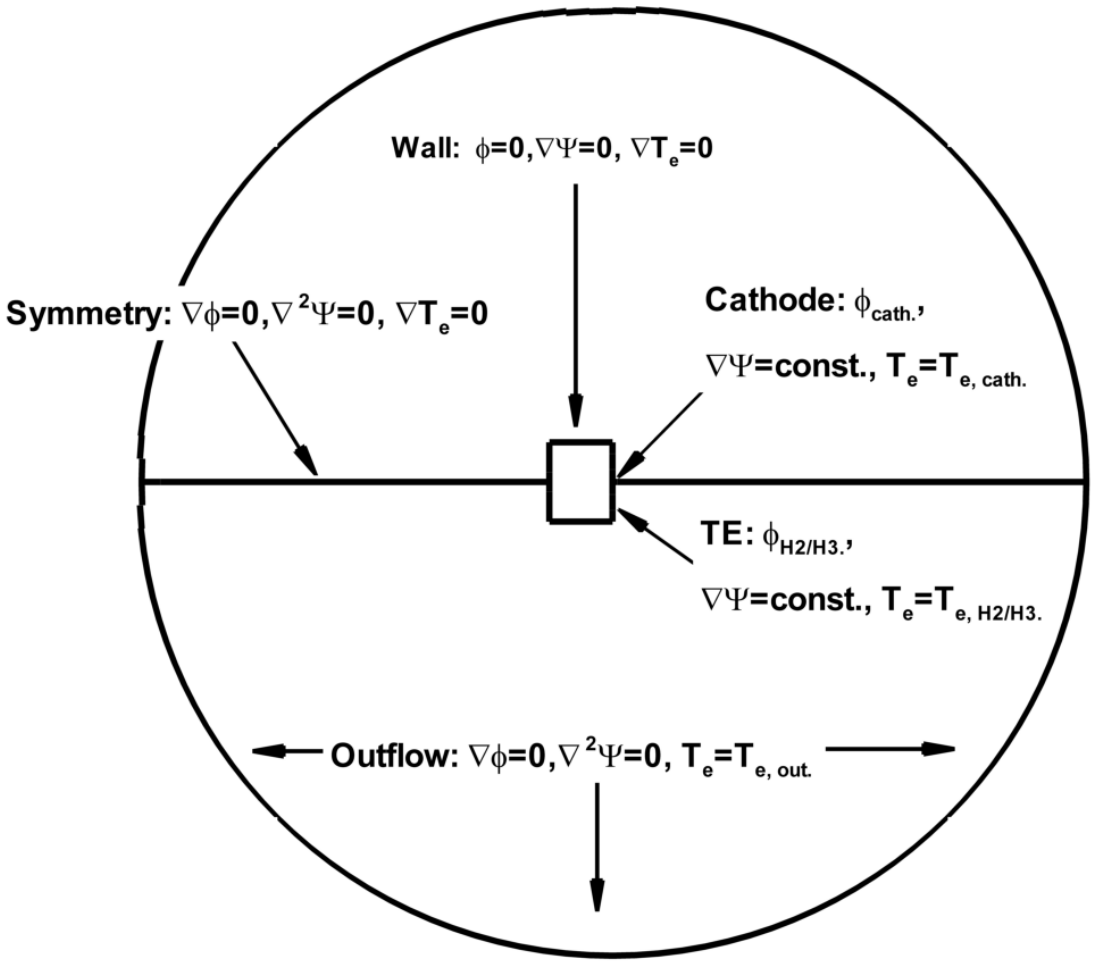

Figure 4.1: Boundary conditions for the electron submodel.

results in between 50-6000 macroparticles per cell. The timestep size is 1×10^{-7} seconds, resulting in a total sampling time of 0.01 seconds. All simulations are run in parallel on the University of Michigan Center for Advanced Computing's Nyx cluster. All simulations utilized 32 processors, with the computational wall time of simulations reported in this section at about 12 hours.

Plume simulations are performed utilizing inflow boundary conditions extracted from results generated by both H2 and H3. Plume simulations utilizing H2 inflow conditions are dubbed "MPIC1-H2," and those utilizing H3 inflow conditions are dubbed "MPIC1-H3." Note that, as in Chapter 3, all results in this chapter use spatial coordinates that are normalized by a characteristic length associated with the thruster, in this case, the mean thruster diameter. Comparisons between the plume simulations are made through examining the following macroscopic plasma properties: ion current density, plasma potential, and electron temperature. Comparisons between the plume simulations and experimental data are made through examining the ion current density and plasma potential. The comparisons focus primarily on the near-field plume region, between 0-3 mean thruster diameters downstream of the TE plane, and between 0-2.5 mean thruster diameters radially from the thruster centerline. There is an additional comparison made using far-field plume data taken in a 180° circular arc with a radius of approximately 1 m and an origin on axis in the TE plane. All comparisons are depicted in Figure 4.2.

4.2.1 MPIC1-H2 and MPIC1-H3 Comparisons

4.2.1.1 Ion Current Density

In this section, ion current density results are presented. Field contours of ion current density are shown in Figure 4.3. Subsequent figures present data that are extracted from this field data. The primary difference between MPIC1-H2 and MPIC1-H3 is in the magnitude of the peak ion current density. The peak ion current density

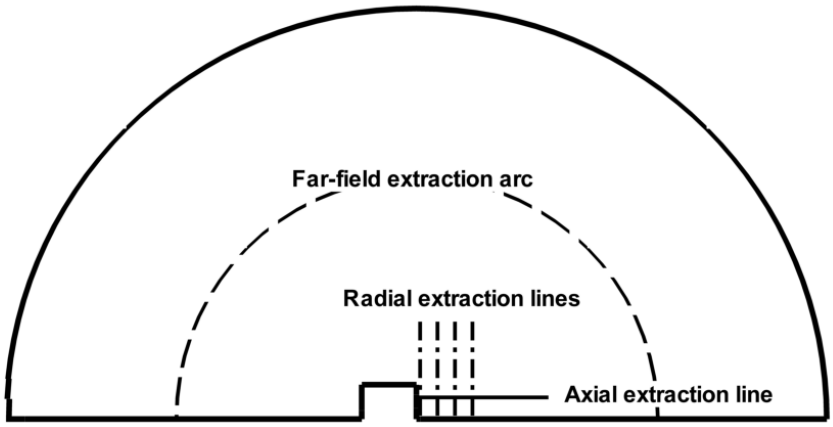

Figure 4.2: Extraction lines utilized in plume comparisons.

occurs approximately 0.05 mean thruster diameters downstream of the TE plane, where H3 predicts a peak current density 11% lower than that predicted by H2, relative to H2. There are three possible reasons for this. First, although the total mass flow rates calculated by H2 and H3 are identical, the mass flow exiting the TE plane as calculated by H3 is constituted differently than the same mass flow calculated by H2: the number flux of neutrals calculated by H3 is slightly higher, therefore the number flux of ions is a smaller fraction of the total mass flow. However, since the total mass flow is primarily made-up of ions, the decrease in number flux of ions is less than 1%. Second, the temperature of the injected ions in MPIC1-H3 is generally higher than that in MPIC1-H2, leading to a greater plume divergence and thereby reducing ion current density. However, Ref. [41] showed that this effect is not significant in the near-field plume. Therefore, the difference in peak ion current density is due to the different plasma potential boundary conditions. As shown above in

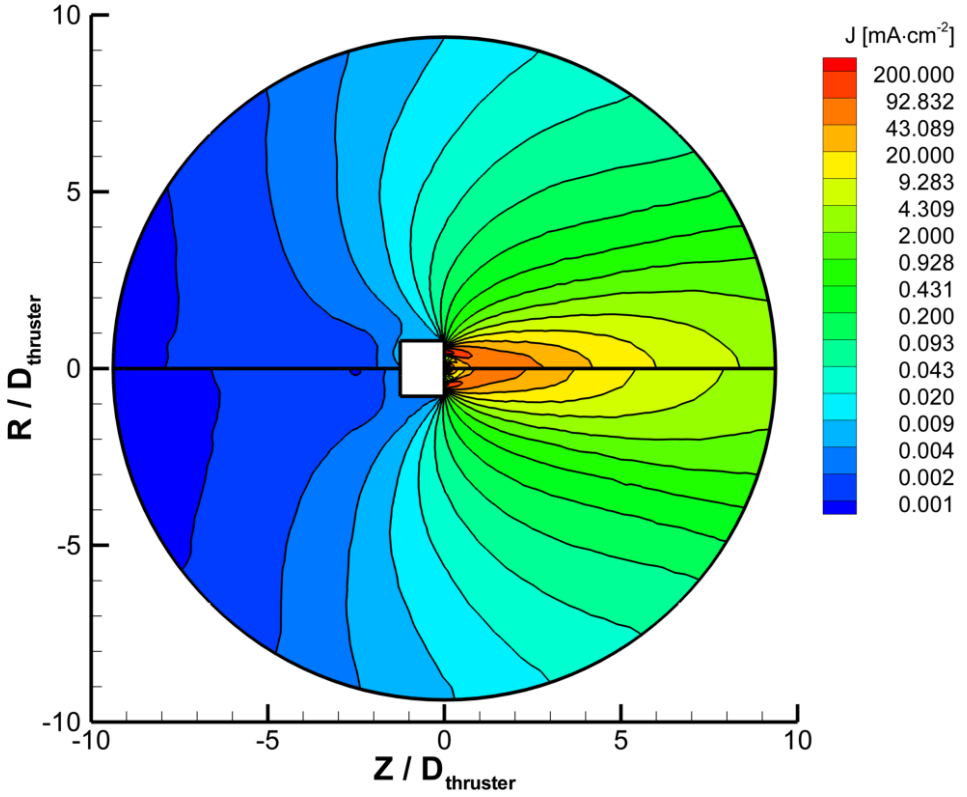

Figure 4.3: Comparison between MPIC1-H2 (top) and MPIC1-H3 (bottom): ion current density contours.

Tables 4.3 and 4.4, the plasma potential at the TE plane as calculated by H3 is significantly higher than that calculated in H2. Since the thruster wall is assumed to be grounded in each case, this results in a larger gradient in potential in MPIC1-H3 than in MPIC1-H2. The difference in gradients is most significant in the near-field where gradients in plasma potential are typically the highest. The larger gradient in MPIC1-H3 increases plume divergence, reducing peak ion current density near the TE plane.

Figures 4.4, 4.5, and 4.6 illustrate quantitative differences between the two plume simulations. Figure 4.4 shows the axial variation of ion current density along the thruster's acceleration channel CL. The MPIC1-H3 calculates a lower ion current density near the TE plane relative to the H2 simulation. In either simulation, the

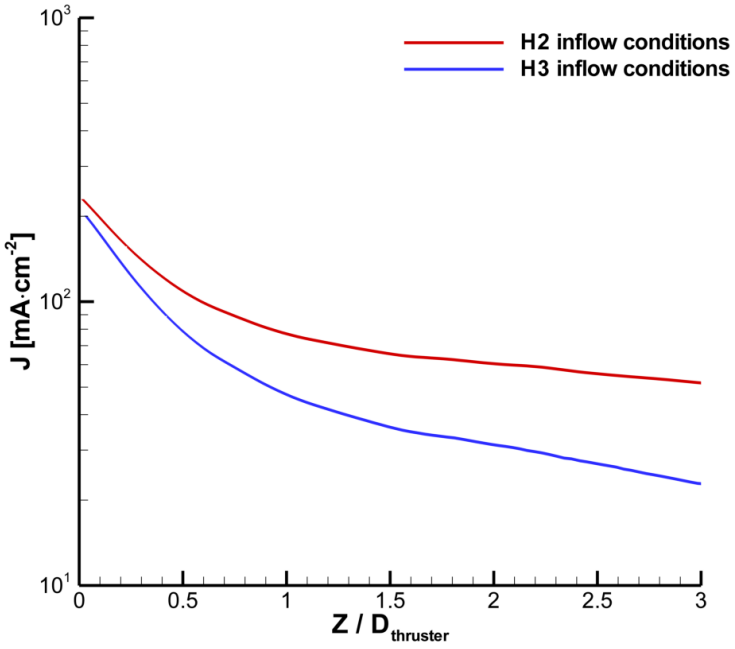

Figure 4.4: Comparison between MPIC1-H2 and MPIC1-H3: axial ion current density variation along $R/D_{thruster} = 0.5$.

ion current density monotonically decreases as $Z/D_{thruster}$ increases, although the H3 simulations calculate a more rapid decay than the H2 simulations. This is due to the abovementioned difference in plasma potential: the H3 overaccelerates the ions at the TE plane, relative to H2, leading to increased plume divergence and more rapid ion current density decay.

Figures 4.5 and 4.6 show radial variations of ion current density at different axial stations. General trends agree with the explanation given above regarding the effect of plasma potential gradients in the near-field on ion current density: MPIC1-H3 typically calculate lower peak ion current densities at each axial station, and MPIC1-H2 calculate a more rapid decline in ion current density as $R/D_{thruster}$ increases.

Figure 4.7 shows angularly resolved ion current density data along a 1 m circular arc. Excepting small differences in low-angle calculations, both MPIC1-H2 and MPIC1-H3 calculate nearly identical profiles: between 5°-45°, ion current density

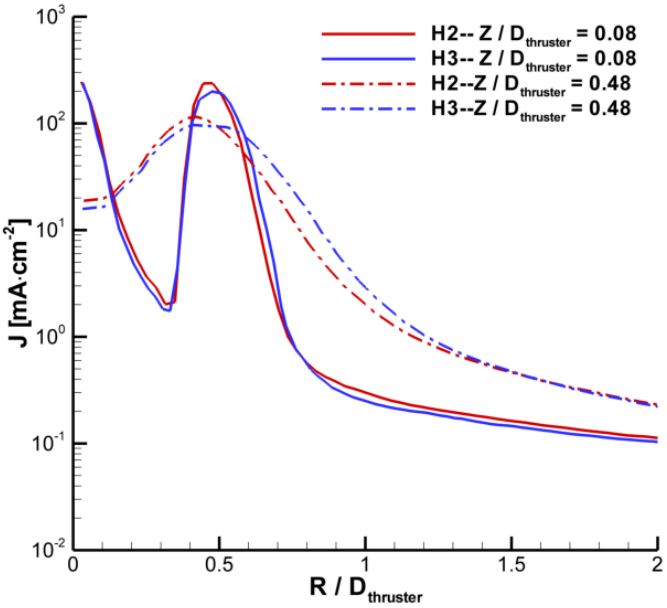

Figure 4.5: Comparison between MPIC1-H2 and MPIC1-H3: radial ion current density variation along $Z/D_{thruster} = 0.08$ and $Z/D_{thruster} = 0.48$.

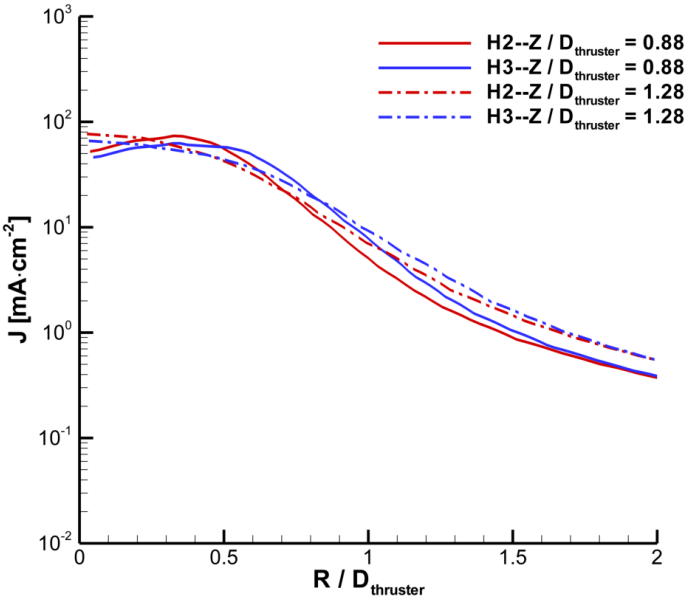

Figure 4.6: Comparison between MPIC1-H2 and MPIC1-H3: radial ion current density variation along $Z/D_{thruster} = 0.88$ and $Z/D_{thruster} = 1.28$.

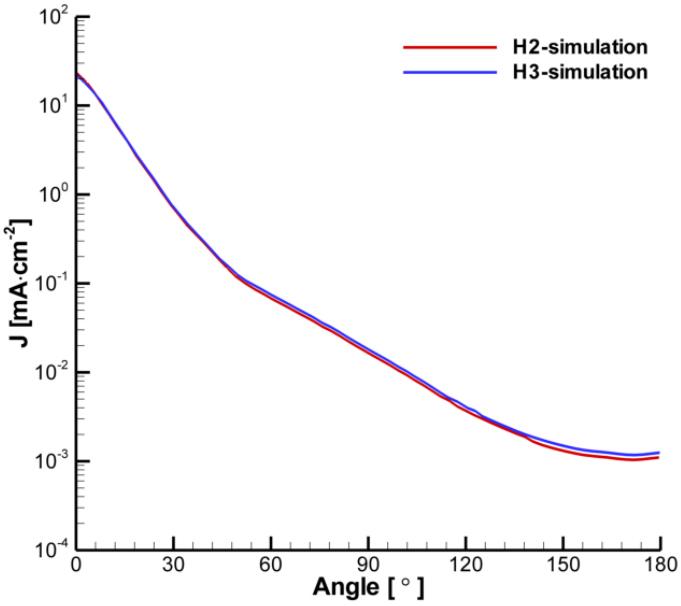

Figure 4.7: Comparison between MPIC1-H2 and MPIC1-H3: far-field ion current density angular variation along a 1 m circular arc.

decays exponentially. There is an inflection point around 45° such that the profile transitions to an exponential decay at a different rate between 45°-150°. These two rates are illustrated in Figure 4.8. At angles greater than 150°, so-called CEX "wings" constitute the bulk of the ion current density.

High plume divergence angle ion current density directly relates to plume impingement concerns stated in Section 1.1.1. Although, as Figure 4.7 illustrates, high-angle ion current density is smaller than low-angle current density by nearly 4 orders of magnitude, ions that constitute high-angle ion current density are more likely to impinge on key spacecraft systems. Therefore, accurately resolving high-angle current density is used in the present study as a metric for assessing each computational model.

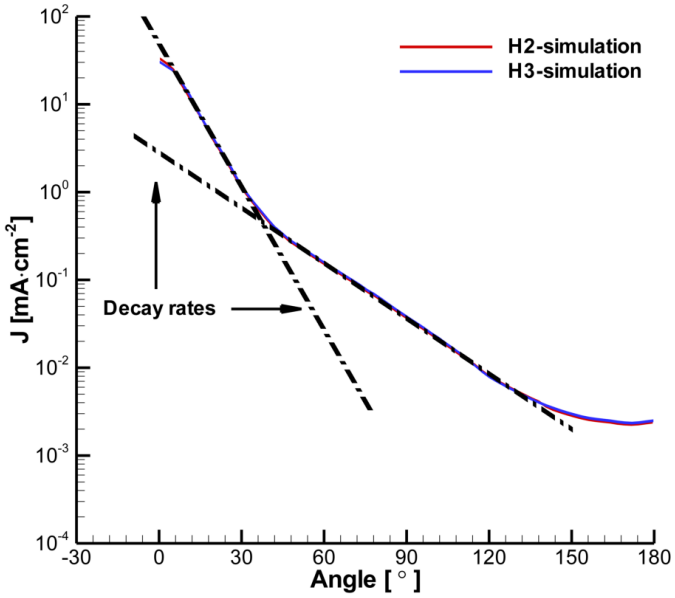

Figure 4.8: Comparison between MPIC1-H2 and MPIC1-H3: illustrating decay rates.

4.2.1.2 Plasma Potential

In this section, plasma potential results are presented. Field contours of plasma potential are shown in Figure 4.9. Subsequent figures present data that are extracted from this field data. The primary difference between MPIC1-H2 and MPIC1-H3 is in the magnitude of the plasma potential at the TE plane. As shown in Tables 4.3 and 4.4, the plasma potential at the TE plane as calculated by H3 is significantly higher than that calculated in H2. This has two effects. First, the peak in plasma potential is larger in MPIC1-H3 than in MPIC1-H2. Second, the MPIC1-H3 calculates a larger gradient in potential than in MPIC1-H2. The difference in gradients is most significant in the near-field, as shown in Figure 4.11.

Figures 4.10, 4.11, and 4.12 illustrate quantitative differences between the two plume simulations. Figure 4.10 shows the axial variation of plasma potential along the thruster's acceleration channel CL. The MPIC1-H3 calculates a higher plasma potential near the TE plane relative to the H2 simulation. The constant $R/D_{thruster}$ =

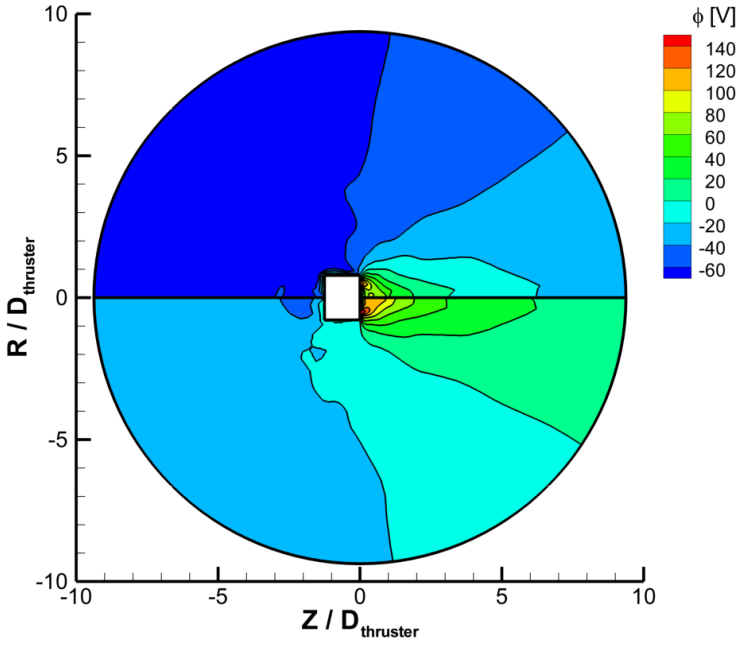

Figure 4.9: Comparison of plasma potential between MPIC1-H2 and MPIC1-H3: H2 inflow conditions on top, H3 inflow conditions on bottom.

0.5 results show similar behavior in MPIC1-H2 and MPIC1-H3: the plasma potential monotonically decreases as $Z/D_{thruster}$ increases. As has been noted, the MPIC1-H3 calculates a larger potential than the MPIC1-H2.

Figures 4.11 and 4.12 show radial variations of plasma potential at different axial stations. General trends agree with the explanation given above regarding the effect of plasma potential gradients in the near-field on ion current density: in the near-field, MPIC1-H3 calculate a larger gradient in potential.

4.2.1.3 Electron Temperature

In this section, electron temperature results are presented. Field contours of electron temperature are shown in Figure 4.13. Subsequent figures present data that are extracted from this field data. The primary difference between MPIC1-H2 and MPIC1-H3 is in the magnitude of the electron temperature at the TE plane. As

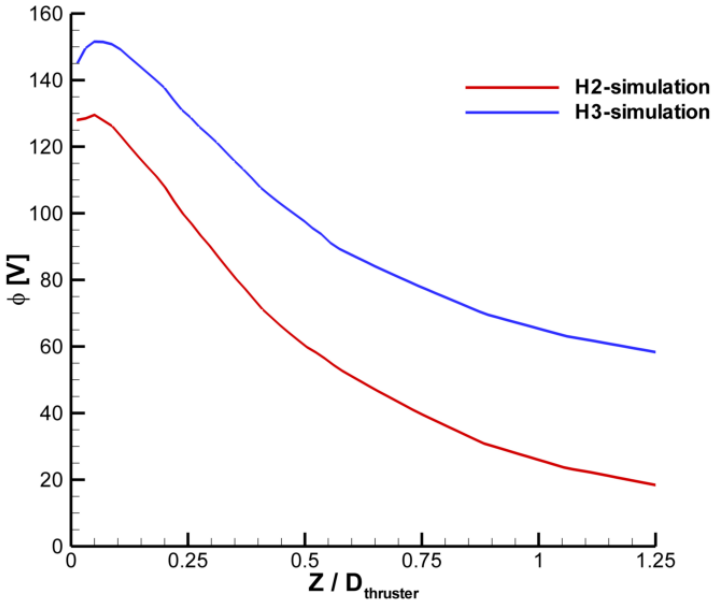

Figure 4.10: Comparison between MPIC1-H2 and MPIC1-H3: axial plasma potential variation along $R/D_{thruster} = 0.5$.

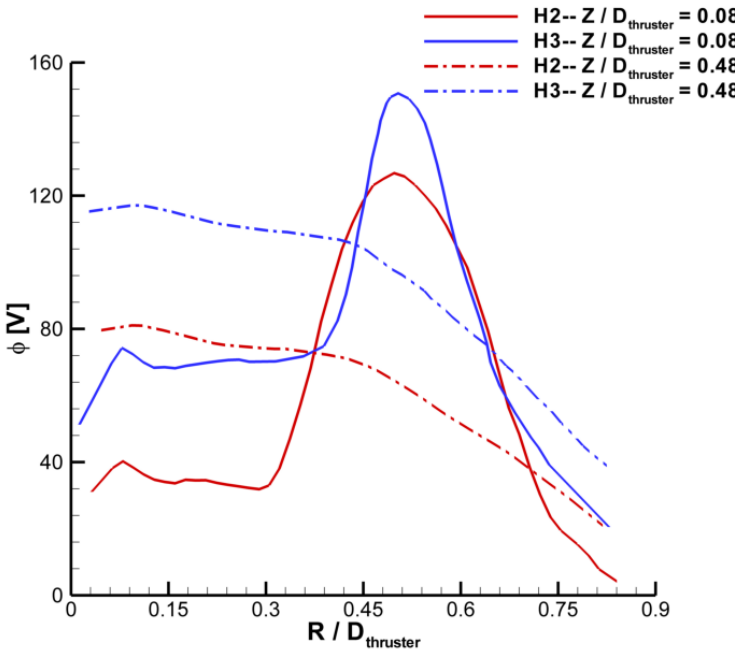

Figure 4.11: Comparison between MPIC1-H2 and MPIC1-H3: radial plasma potential variation along $Z/D_{thruster} = 0.08$ and $Z/D_{thruster} = 0.48$.

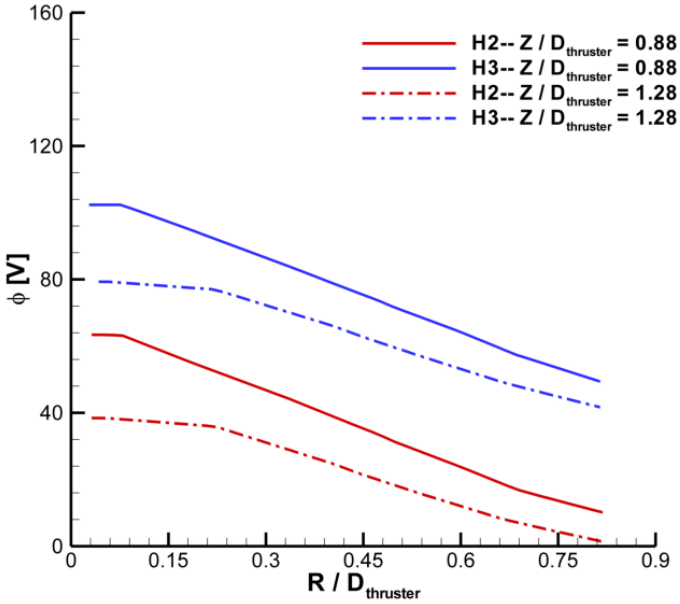

Figure 4.12: Comparison between MPIC1-H2 and MPIC1-H3: radial plasma potential variation along $Z/D_{thruster} = 0.88$ and $Z/D_{thruster} = 1.28$.

shown in Tables 4.3 and 4.4, the electron temperature at the TE plane as calculated by H3 is marginally higher than that calculated in H2. This results in similar trends between MPIC1-H2 and MPIC1-H3, with the sole difference being the magnitude of the calculated temperature.

Figures 4.14, 4.15, and 4.16 illustrate quantitative differences between the two plume simulations. Figure 4.14 shows the axial variation of electron temperature along the thruster's acceleration channel CL. The MPIC1-H3 calculates a higher electron temperature near the TE plane relative to the H2 simulation. The constant $R/D_{thruster} = 0.5$ results show similar behavior in MPIC1-H2 and MPIC1-H3: the electron temperature monotonically decreases as $Z/D_{thruster}$ increases. As has been noted, the MPIC1-H3 calculates a larger electron temperature than the MPIC1-H2.

Figures 4.15 and 4.16 show radial variations of electron temperature at different axial stations. General trends correspond with field results: a slightly larger magnitude of electron temperature is calculated in MPIC1-H3 relative to MPIC1-H2,

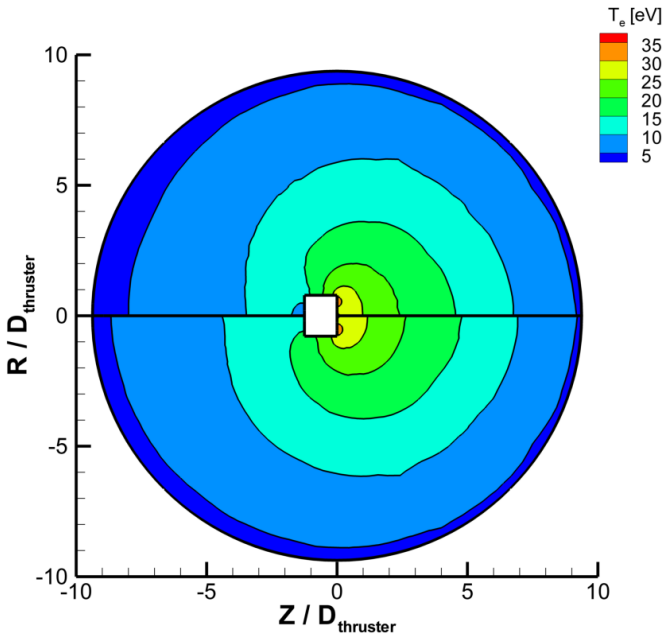

Figure 4.13: Comparison of electron temperature between MPIC1-H2 and MPIC1-H3: H2 inflow conditions on top, H3 inflow conditions on bottom.

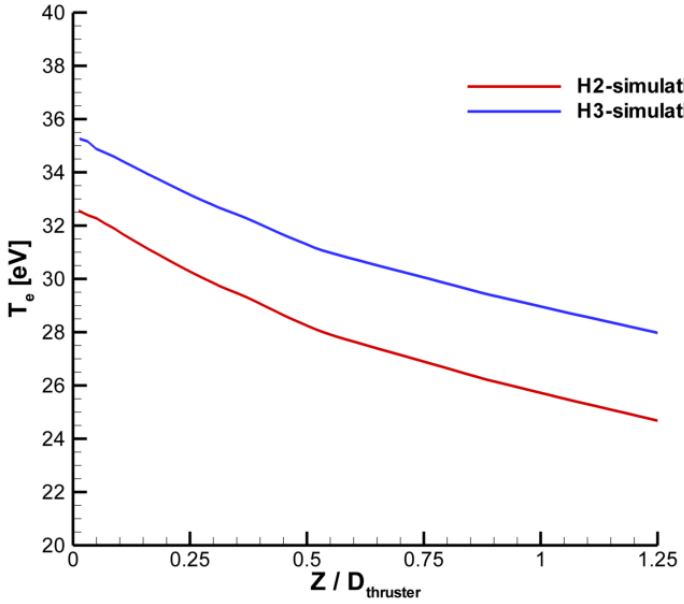

Figure 4.14: Comparison between MPIC1-H2 and MPIC1-H3: axial electron temperature variation along $R/D_{thruster} = 0.5$.

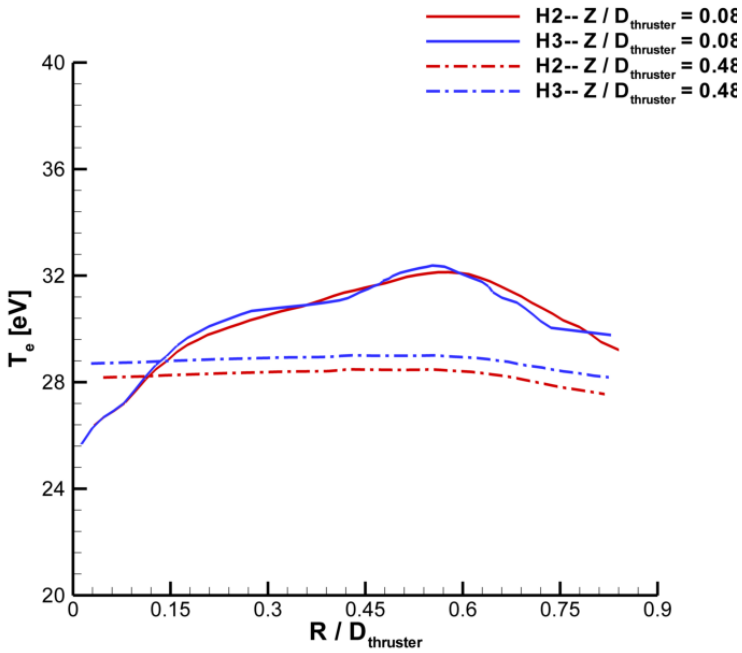

Figure 4.15: Comparison between MPIC1-H2 and MPIC1-H3: radial electron temperature variation along $Z/D_{thruster} = 0.08$ and $Z/D_{thruster} = 0.48$.

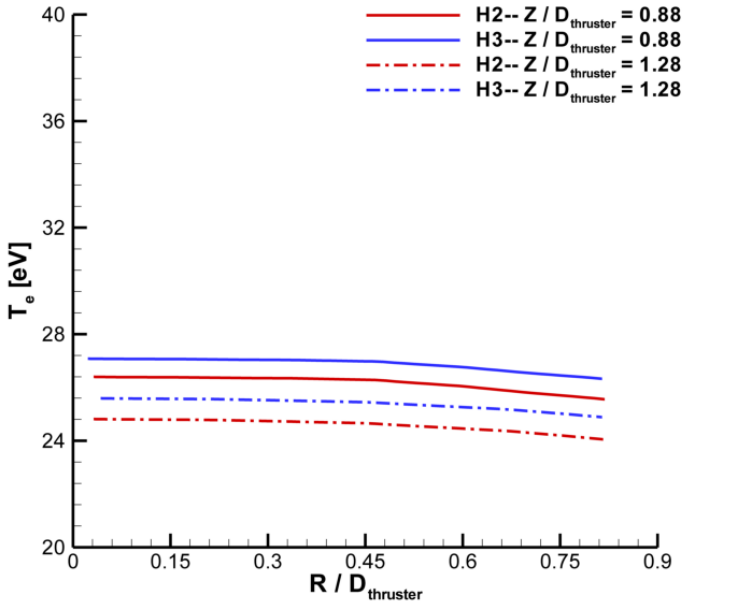

Figure 4.16: Comparison between MPIC1-H2 and MPIC1-H3: radial electron temperature variation along $Z/D_{thruster} = 0.88$ and $Z/D_{thruster} = 1.28$.

and temperature uniformly decreases as axial and radial distance from the TE plane increases.

4.2.1.4 Discussion

In general, MPIC1-H2 and MPIC1-H3 produce qualitatively similar results. The primary difference between the two inflow conditions is in the plasma potential magnitude: the higher magnitude potential in MPIC1-H3 produces larger gradients in potential, relative to MPIC1-H2. These larger gradients increase plume divergence, diffusing the main ion beam to a greater extent than in MPIC1-H2. In the next section, simulated results are compared to experimental measurements in order to evaluate these differences.

4.2.2 Comparing Plume Simulations to Experimental Measurement

In this section, MPIC1-H2 and H3-based plume simulation calculations of ion current density and plasma potential are compared to experimental measurements. The ion current density measurements that are compared against were provided by PEPL, whereas the plasma potential data were provided by JPL.

4.2.2.1 Ion Current Density

Experimental measurements of ion current density were performed by Reid [8]. The ion current density measurements were taken using the two Faraday cup probes outlined in Section 1.1.2.4. The uncertainty associated with the near-field probe measurements is $\pm 10\%$, whereas the uncertainty associated with the far-field probe measurements is $\pm 0 - 50\%$ on the integrated beam current. The near-field data is presented first, followed by the far-field data.

The near-field ion current density contours reported here are formed from over 64,000 individual measurements [8]. Subsequent comparisons of ion current density

profiles are extracted from this experimental data set. It should be noted here that these measured data were not corrected for sheath growth, edge effects, or cosine losses. Figures 4.17 and 4.18 show comparisons of these measurements to near-field ion current density calculations in MPIC1-H2 and H3-based plume simulations. Both simulations, as well as the experimental data, show the beam of ions at the TE plane to be highly collimated over the first mean thruster diameter. Both MPIC1-H2 and MPIC1-H3 generally overpredict the magnitude of ion current density relative to the measured data, with MPIC1-H2 overpredicting by a larger factor than MPIC1-H3. The measured peak ion current density for the main beam is 128 $\frac{mA}{cm^2}$ and occurs at $Z/D_{thruster} = 0.2$ and $R/D_{thruster} = 0.5$, whereas the simulations calculate ion current densities of approximately 159 $\frac{mA}{cm^2}$ and 145 $\frac{mA}{cm^2}$ at the same location for MPIC1-H2 and MPIC1-H3, respectively. MPIC1-H2 and MPIC1-H3 calculate a higher peak ion current density than the measured peak, even when accounting for measurement uncertainty of +10%. The discrepancy could be due to the placement of the investigation window for the measurements: the calculated peak ion current densities for the main beam occur at $Z/D_{thruster} = 0.05$, which is nearly coincident with the edge of the window. More likely, however, this might be due to the electron submodel utilized in MPIC1: neglecting the $\vec{B}$ field has the largest impact near the TE plane, where gradients in plasma potential are under-predicted, relative to MPIC1-H2. This results in an under-prediction of electric field magnitude and subsequent under-acceleration of ions, which in turn increases ion current density.

Figures 4.19- 4.23 show ion current density profiles as calculated by MPIC1-H2 and MPIC1-H3 compared to experimental data. The axial profiles in Figure 4.19 show qualitative agreement between the measured data and the calculated ion current densities: for $Z/D_{thruster} > 0.3$, ion current density monotonically decreases. In general, MPIC1-H3 shows better agreement with measured data than MPIC1-H2. However, the measured data shows a higher rate of decay relative to either simula-

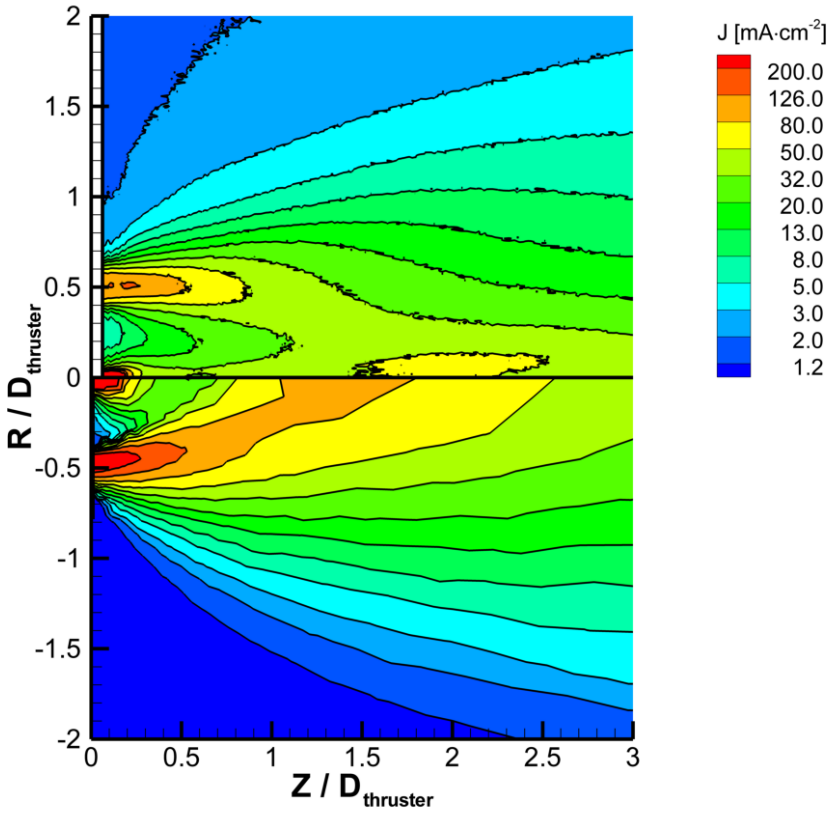

Figure 4.17: Comparison of ion current density between experimental measurements (top) and MPIC1-H2 (bottom).

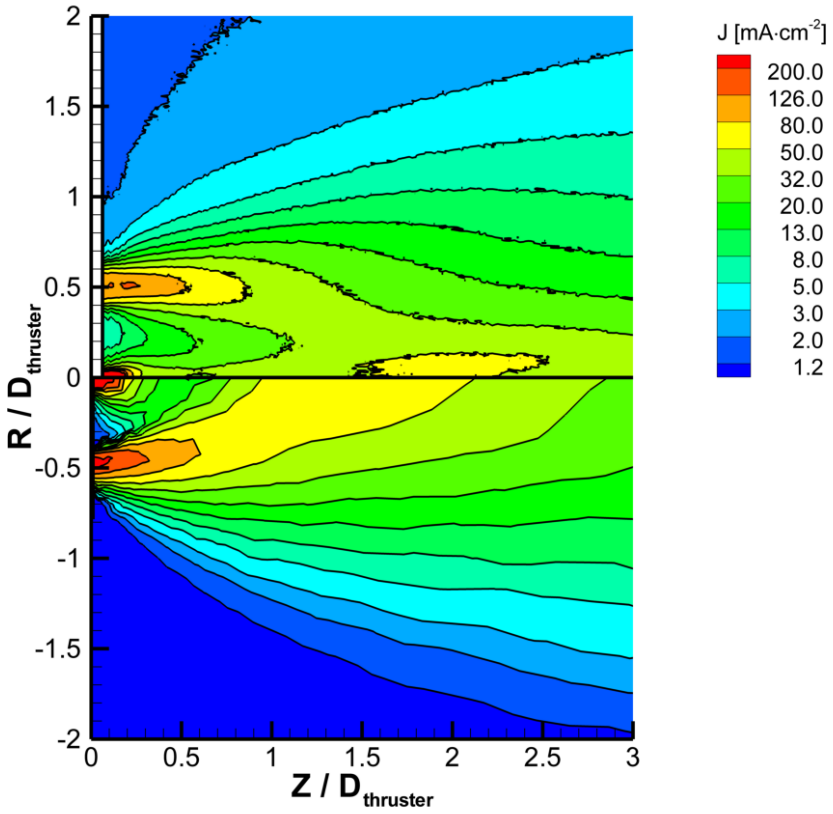

Figure 4.18: Comparison of ion current density between experimental measurements (top) and MPIC1-H3 (bottom).

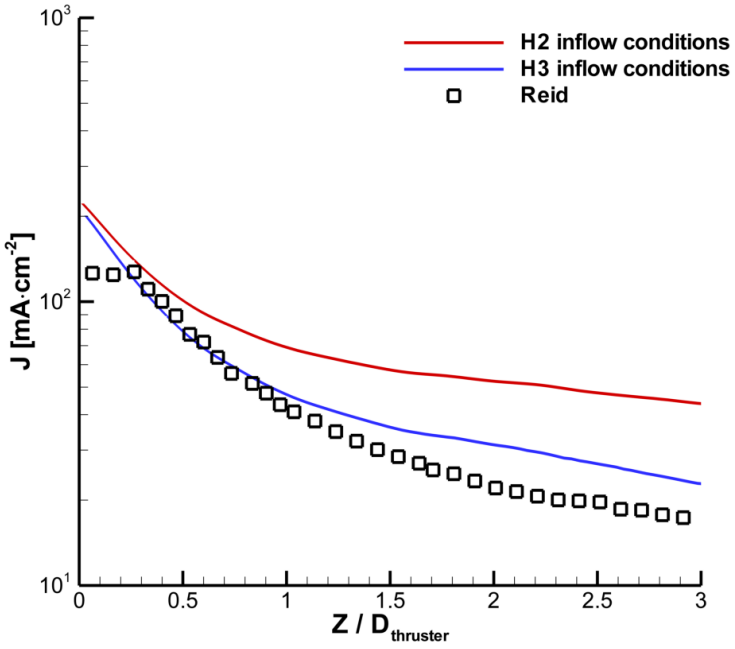

Figure 4.19: Comparison between MPIC1-H2, MPIC1-H3, and experimental measurements: axial ion current density variation along $R/D_{thruster} = 0.5$.

tion. Additionally, between $Z/D_{thruster} = 0.05 - 0.2$, measured data actually shows an increase in ion current density, whereas both simulations calculate a decrease in ion current density due to the same limitations of the electron submodel discussed above.

Figures 4.20- 4.23 show radial profiles of ion current density as calculated by MPIC1-H2 and MPIC1-H3 compared to measured data. Figure 4.20 shows radial profiles at an axial station of $Z/D_{thruster} = 0.08$. While there is qualitative agreement between the simulations and the measured data at this location, there are also significant quantitative discrepancies. First, there is a centerline "spike" in ion current density in the near field plume that the simulations underpredict relative to the measured data. The "spike" as discussed in [8] is due to both non-zero radial velocity of ions at the TE plane, as well as the plasma potential field focusing ions toward the thruster centerline. When compared to measured data, MPIC1-H2 and MPIC1-H3

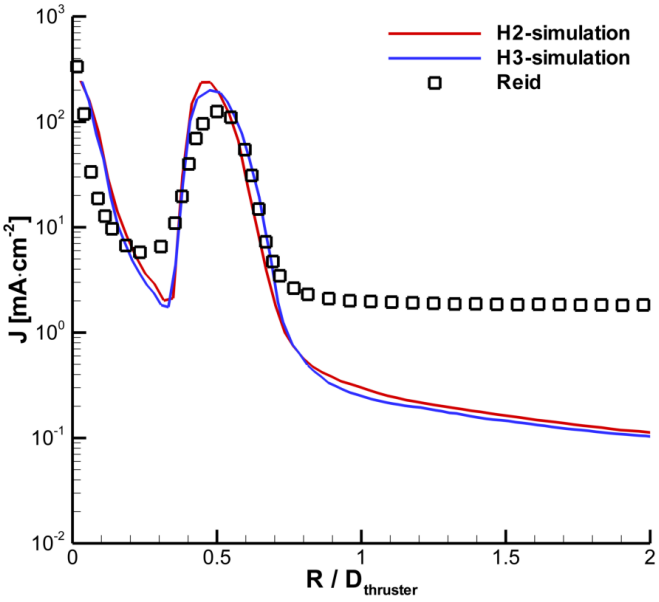

Figure 4.20: Comparison between MPIC1-H2, MPIC1-H3, and experimental measurements: radial ion current density variation along $Z/D_{thruster} = 0.08$.

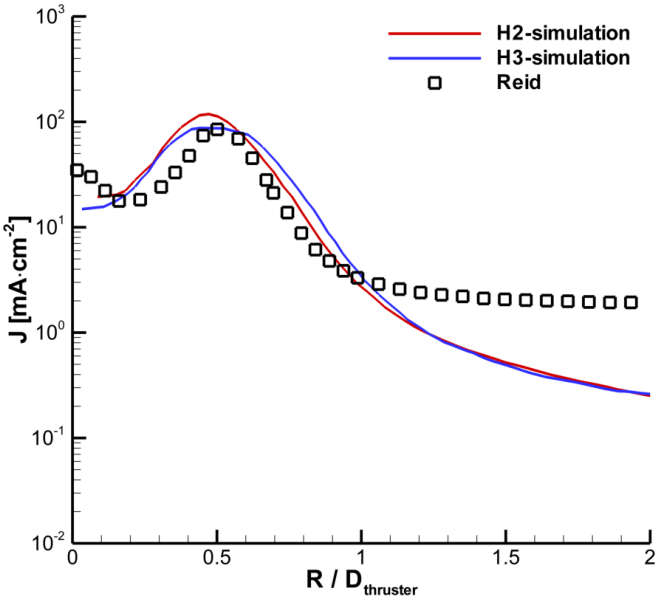

Figure 4.21: Comparison between MPIC1-H2, MPIC1-H3, and experimental measurements: radial ion current density variation along $Z/D_{thruster} = 0.48$.

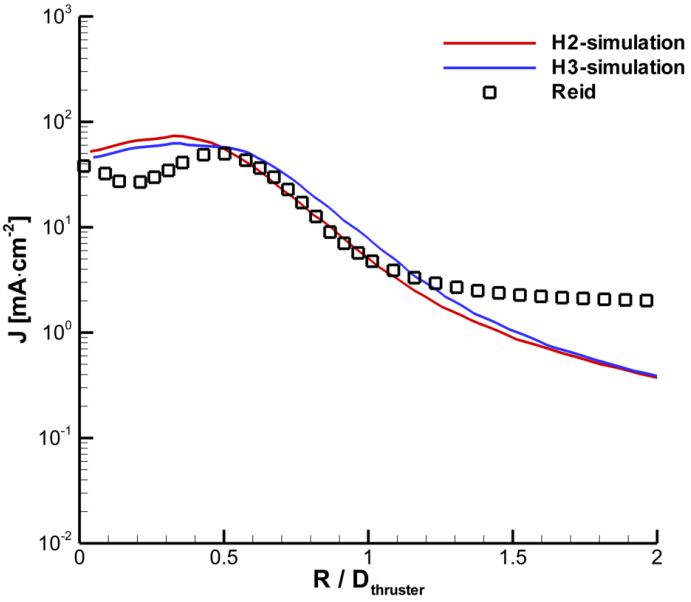

Figure 4.22: Comparison between MPIC1-H2, MPIC1-H3, and experimental measurements: radial ion current density variation along $Z/D_{thruster} = 0.88$.

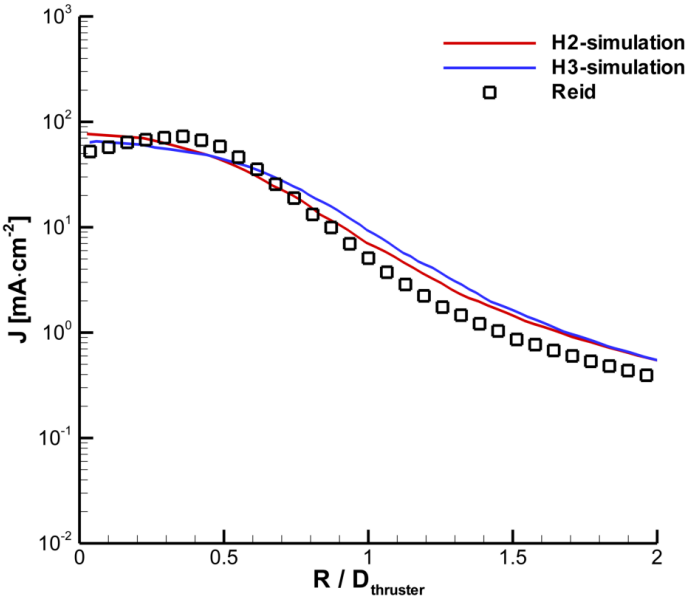

Figure 4.23: Comparison between MPIC1-H2, MPIC1-H3, and experimental measurements: radial ion current density variation along $Z/D_{thruster} = 1.28$.

underpredict the magnitude of the centerline spike by approximately 30%. There are two possible explanations for this. First, the plasma potential field calculated by MPIC1-H2 and MPIC1-H3 ignores $\vec{B}$ field effects, which are important in the near-field plume. Second, the current boundary condition assumed at the cathode injects solely neutral atoms into the simulation domain. This assumption is made for the sake of theoretical clarity, but may not accurately reflect the physical situation. The second quantitative discrepancy between the measured and simulated profiles is the magnitude of the main beam ion current density, which was discussed above. In this case, MPIC1-H3 shows better agreement with measured data than MPIC1-H2: MPIC1-H3 overpredicts the main beam peak ion current density by approximately 12%, whereas MPIC1-H2 overpredicts by approximately 23%. The third discrepancy is the profile behavior at $R/D_{thruster} > 0.8$: both MPIC1-H2 and MPIC1-H3 calculate steady decay of ion current density in this region, whereas the measured ion current density remains nearly constant at around 1.9 $\frac{mA}{cm^2}$. As noted above, the ion current density measurements in the near-field were made with a Faraday probe that did not have a guard ring. As a result, the probe is susceptible to collecting a non-trivial amount of CEX ions at far off-axis locations [75]. Since the measured data were not corrected for edge effects, the plateau in measured ion current density at far off-axis locations is not solely a measure of the beam current.

Figures 4.21- 4.23 show the behavior of radial profiles of ion current density as $Z/D_{thruster}$ increases. These figures show moderate qualitative agreement between simulation and measurements, although significant plume structures are resolved differently when comparing simulated results to the measured data. Due to the underprediction of the centerline spike in ion current density, MPIC1-H2 and MPIC1-H3 calculate a coalescence of the centerline beam into the main ion beam at just over $Z/D_{thruster} = 0.48$, whereas measurements indicate two distinct beams as far downstream as $Z/D_{thruster} = 0.88$. Other qualitative features show better agreement

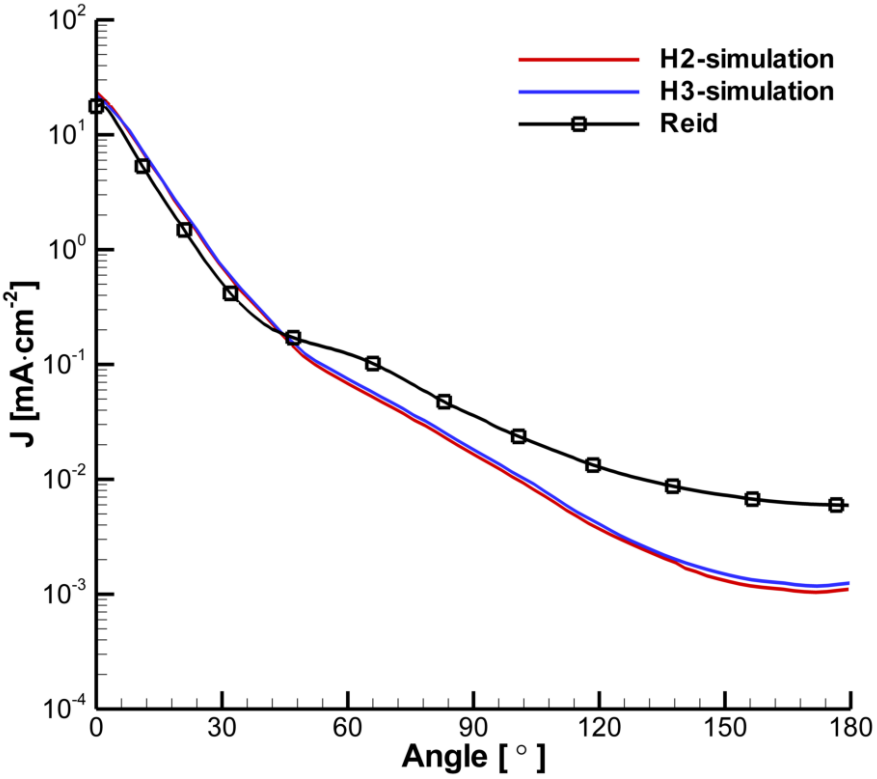

Figure 4.24: Comparison between MPIC1-H2, MPIC1-H3, and experimental measurements: angular variation of far-field ion current density along a 1 m circular arc.

between simulation and measurements: the measured magnitude of the main beam ion current density shows good agreement with MPIC1-H2 and MPIC1-H3 results equally. Again, at far off-axis locations, the ion current density measurements at $Z/D_{thruster} = 0.48$ and $Z/D_{thruster} = 0.88$ exhibit a plateau at around 1.9 $\frac{mA}{cm^2}$.

Figure 4.24 shows comparisons of angularly resolved far-field ion current density. The measured data shown here were acquired with the far-field Faraday probe outlined in Section 1.1.2.4. Qualitative agreement between simulation and experiment is good between 0°-30°, although MPIC1-H2 and MPIC1-H3 overpredict the measured ion current density by nearly 50% at some angles in that range. The measurements show an inflection point near 30°, near the calculated inflection point of 45°; however,

the measurements also show a second inflection point near 60°, such that the exponential decay of current density occurs at different rates in these three regions: 5°-30°, 40°-60°, and 60°-150°. Between 150°-180°, the measurements show CEX wings, which agree with the simulated profiles. The measured decay rate in the low-angle region shows good agreement with the calculated decay rate, whereas the decay rates measured in the other two regions are lower than the calculated rates. This results in simulated data overpredicting ion current density between 0°-90° and significantly underpredicting between 90°-180°, relative to measured data. For example, relative to the measured data, MPIC1-H2 and MPIC1-H3 underpredict ion current density by as much as 80% at 150°.

The integrated ion beam currents based on the profiles in Figure 4.24 are as follows: integrating the MPIC1-H2 and MPIC1-H3 profiles results in an ion beam current of 18.0 A in each case; integrating experimental measurements results in an ion beam current of 21 A. The uncertainty associated with the integrated ion beam current ranges between $0 - 50\%$, which the calculated beam currents are both well within. The total discharge current for the nominal operating condition is 20 A, lower than the measured integrated ion beam current and higher than the simulated integrated current. In fact, the integrated ion beam current from the measurements should be lower than the discharge current of the thruster. The difference between the total discharge current and the measured integrated ion beam current could be due to facility back-pressure affecting the diagnostics.

4.2.2.2 Plasma Potential

Experimental measurements of plasma potential were performed by Jameson [11]. The plasma potential measurements were taken using the emissive probe outlined in Section 1.1.2.4 in an investigation window spanning $Z/D_{thruster} = 0.05 - 1.25$ and $R/D_{thruster} = 0 - 0.85$. The uncertainty associated with these measurements

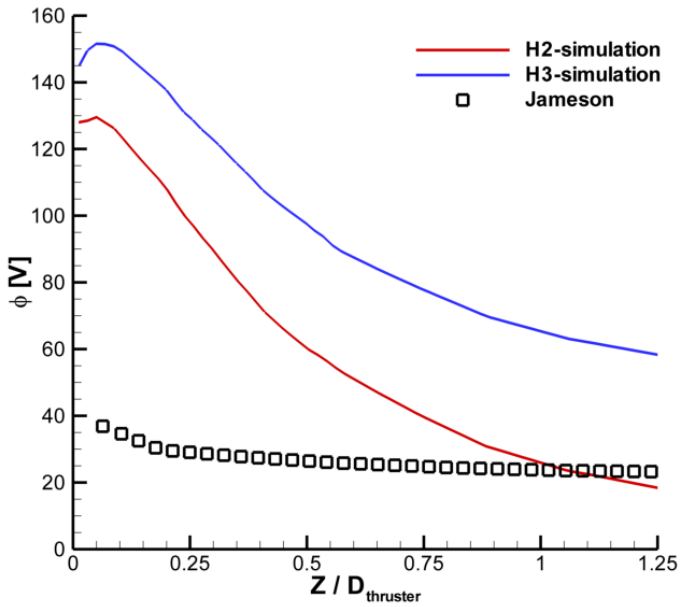

Figure 4.25: Comparison between MPIC1-H2, MPIC1-H3, and experimental measurements: axial plasma potential variation along $R/D_{thruster} = 0.5$.

is $+3/-1V$.

No field data comparisons of plasma potential are presented as the calculated plasma potential results are larger than the measured potential to the degree that meaningful comparisons cannot be made. Figures 4.25- 4.29 illustrate qualitative differences between the plume simulations and measured data. Figure 4.25 shows the axial variation of plasma potential along the thruster's acceleration channel CL. In the near-field, both MPIC1-H2 and MPIC1-H3 calculate plasma potentials well above the measured data: between $Z/D_{thruster} = 0 - 0.25$, calculated potential overpredicts the measured data by between 100-225%. Figure 4.25 shows the measured plasma potential varies over a smaller dynamic range than the range calculated by MPIC1-H2 and MPIC1-H3: the range of measured values of plasma potential is approximately 14 V, whereas the range of simulated values is approximately 100 V.

Figures 4.26- 4.29 show radial variations of plasma potential at different axial stations. In the near-field, there is reasonable qualitative agreement between sim-

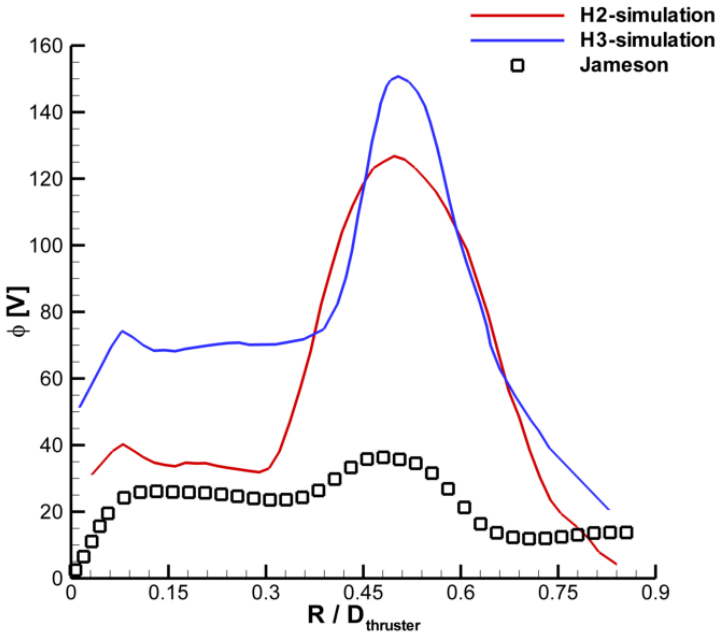

Figure 4.26: Comparison between MPIC1-H2, MPIC1-H3, and experimental measurements: radial plasma potential variation along $Z/D_{thruster} = 0.08$.

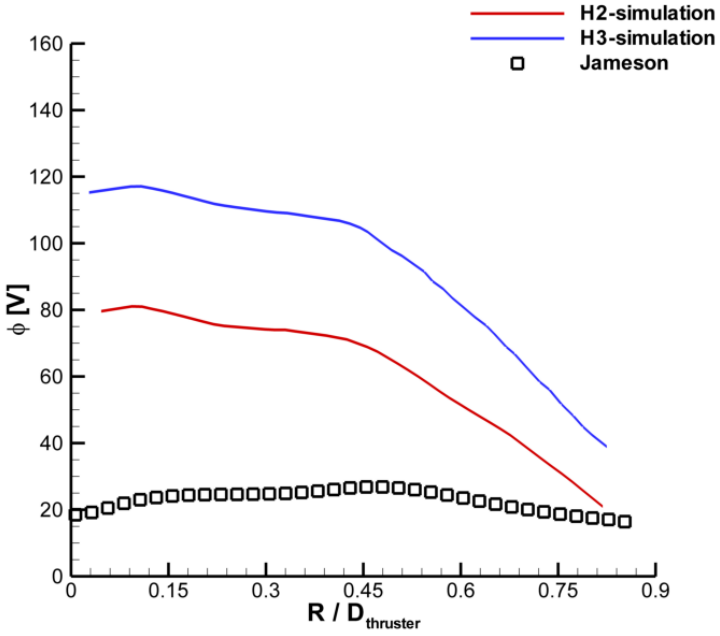

Figure 4.27: Comparison between MPIC1-H2, MPIC1-H3, and experimental measurements: radial plasma potential variation along $Z/D_{thruster} = 0.48$.

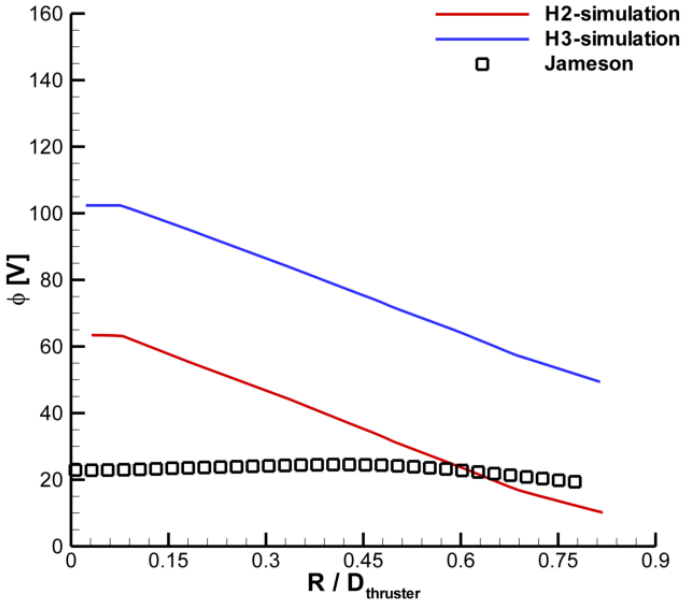

Figure 4.28: Comparison between MPIC1-H2, MPIC1-H3, and experimental measurements: radial plasma potential variation along $Z/D_{thruster} = 0.88$.

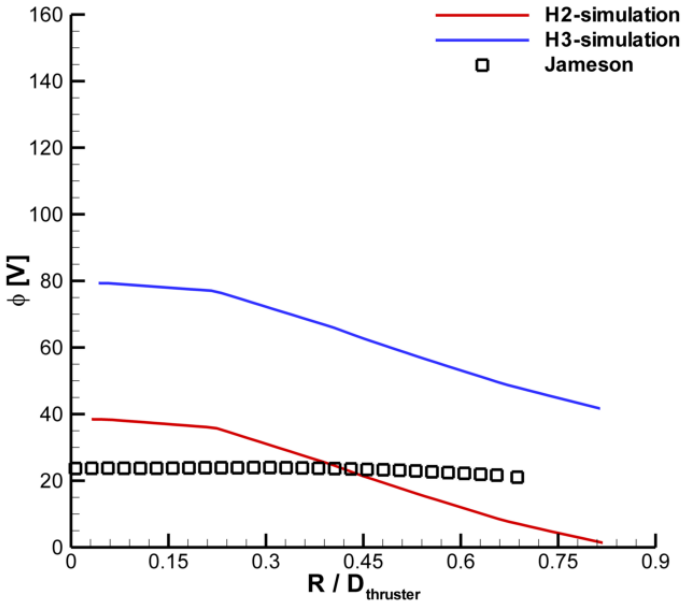

Figure 4.29: Comparison between MPIC1-H2, MPIC1-H3, and experimental measurements: radial plasma potential variation along $Z/D_{thruster} = 1.28$.

ulations and measurements regarding plasma potential behavior: a clear peak near the TE plane is observed, with plasma potential sharply decreasing near the cathode. However, at axial stations further downstream, MPIC1-H2 and MPIC1-H3 calculate a uniform decay with increasing $R/D_{thruster}$, whereas the measured profiles show decreasing amounts of radial variation, eventually reaching a constant value of about 25 V. Quantitative trends are similar to those seen in Figure 4.25: in the near-field, calculated profiles of plasma potential significantly overpredict the measured profiles; as $Z/D_{thruster}$ increases, these differences diminish due to the decay in the radial direction which MPIC1-H2 and MPIC1-H3 calculate but is not observed in the measurements.

4.2.2.3 Discussion

Comparisons between MPIC1-H2 and MPIC1-H3 and measured data show moderate to good agreement regarding ion current density, but poor agreement regarding plasma potential. In the near-field, the magnitude of MPIC1-H3 ion current density calculations showed better agreement with measured ion current density magnitudes than MPIC1-H2, particularly for main beam ions. Based on MPIC1-H3's better agreement with measurements, both internal to the thruster and in the near-field plume, inflow conditions extracted from H3 are used exclusively for the remaining plume simulations in this dissertation.

Significant differences remain between the simulations and measurements regarding the magnitude of the centerline spike in ion current density: near the TE plane, MPIC1-H2 and MPIC1-H3 underpredict the centerline ion current density by approximately 30%. However, as $Z/D_{thruster}$ increases, the differences between MPIC1-H2 and MPIC1-H3 diminish, with both simulations showing better agreement with measured ion current densities. Comparisons of far-field ion current density show good agreement between simulations and measurements between 0°-30°, whereas at higher angles, MPIC1-H2 and MPIC1-H3 significantly underpredict the measurements. Since

high-angle ion current density is a primary metric in the present study, the next section will examine collision models that are expected to calculate high-angle ion current densities that are in better agreement with measurements.

Both MPIC1-H2 and MPIC1-H3 showed poor agreement with measured plasma potential data. Figures 4.25 and 4.26 show the largest discrepancies occurring at the TE plane and subsequently propagating throughout the domain. The primary reason for the discrepancies is due to the fact that the plume simulations ignore magnetic field effects. Physically, the magnetic field (in conjunction with the electric field) confines electrons to an azimuthal drift, effectively shortening the ionization/acceleration zone and increasing the magnitude of the gradient in plasma potential. Since the magnetic field is not modeled, gradients in plasma potential calculated in strong magnetic field regions are smaller in magnitude. This results in comparisons of plasma potential between simulations and measurements that are disparate in the near-field plume. Chapter 5 investigates a method of calculating plasma potential that shows better agreement with measured data.

4.3 Evaluating Post-collision Scattering Models

The plume simulations presented in this section use either the MPIC1 or MPIC2 heavy species submodel as outlined in Section 2.2.4.2 and the detailed fluid electron submodel as outlined in Section 2.3.2.2. Plume simulations utilizing the MPIC1 heavy species submodel are dubbed "MPIC1-simulation(s)," and those utilizing the MPIC2 submodel are dubbed "MPIC2-simulation(s)," where the main difference between the two is in the method of calculating post-collision scattering angles. The numerical details are identical to those in detailed in Section 4.2: simulation runs for 350,000 timesteps to reach a steady state and then for another 100,000 timesteps to sample macroscopic data, resulting in a total of approximately 2.5 million particles at steady state. The same computational domain of 3,191 triangular cells is used. The timestep size is 1×10^{-7} seconds, resulting in a total sampling time of 0.01 seconds. All simulations are run in parallel on the Nyx cluster, utilizing 32 processors. Computational wall time for MPIC1-simulations is around 12 hours, whereas wall time for MPIC2-simulations is around 15 hours. The primary difference between MPIC1- and MPIC2-simulation is in the heavy species submodel that each utilize, therefore comparisons between the plume simulations are made through examining heavy species properties, namely: particle velocity, number density, and ion current density.

4.3.1 Ion Velocity

In this section, velocity data for the ionized heavy species particles are presented for MPIC1- and MPIC2-simulation. Field contours of axial velocity of Xe^{+} and Xe^{2+} are shown in Figures 4.30 and 4.31, whereas contours of radial velocity are shown in Figures 4.32 and 4.33. Subsequent figures present data that are extracted from this field data. The primary difference between MPIC1-simulations and MPIC2-simulations is in the magnitude of the peak axial and peak radial velocity of both species. The peak axial velocity of Xe^{+} calculated by MPIC2-simulation is 8% higher

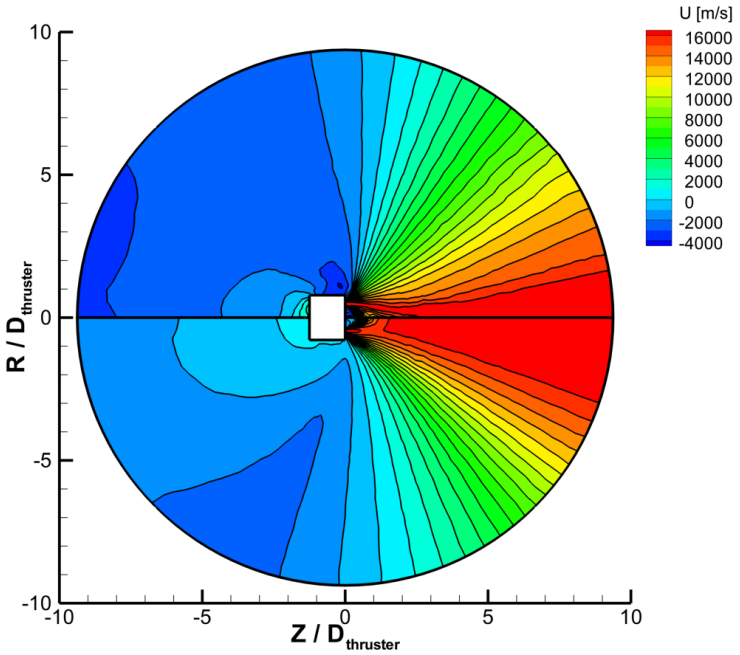

Figure 4.30: Comparison between MPIC1-simulation (bottom) and MPIC2-simulation (top): axial velocity contours of Xe^{+}.

than that calculated by MPIC1-simulation, relative to MPIC1, whereas the peak axial velocity of Xe^{2+} calculated by MPIC2-simulation is 6.5% higher than that calculated by MPIC1-simulation, relative to MPIC1. The peak radial velocity of Xe^{+} calculated by MPIC2-simulation is 9% higher than that calculated by MPIC1-simulation, relative to MPIC1, whereas the peak radial velocity of Xe^{2+} calculated by MPIC2-simulation is 4% higher than that calculated by MPIC1-simulation, relative to MPIC1.

The increase in the peak magnitude of velocity of Xe^{+} and Xe^{2+} ions is a direct effect of the difference in collision dynamics model between MPIC1 and MPIC2. In MEX collisions between atoms and ions, the post-collision scattering angle distribution that is sampled from in MPIC2-simulation is more heavily weighted toward low-angle scattering than the distribution used in MPIC1-simulation. This results in fewer high-angle scattering MEX collisions in MPIC2 relative to MPIC1, such that axial velocity of ions is not altered by MEX collisions in MPIC2 to the same degree it is affected in MPIC1: plume divergence is decreased in MPIC2 relative to MPIC1.

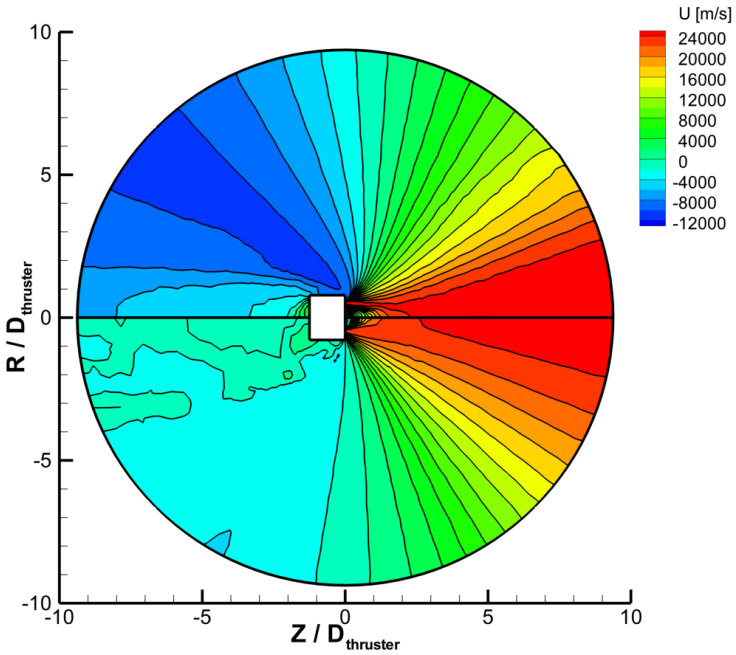

Figure 4.31: Comparison between MPIC1-simulation (bottom) and MPIC2-simulation (top): axial velocity contours of Xe^{2+}.

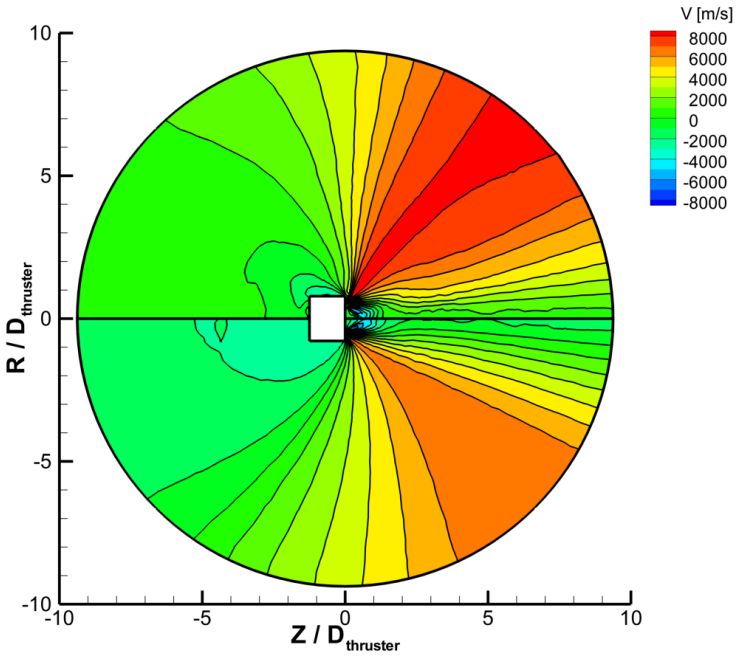

Figure 4.32: Comparison between MPIC1-simulation (bottom) and MPIC2-simulation (top): radial velocity contours of Xe^{+}.

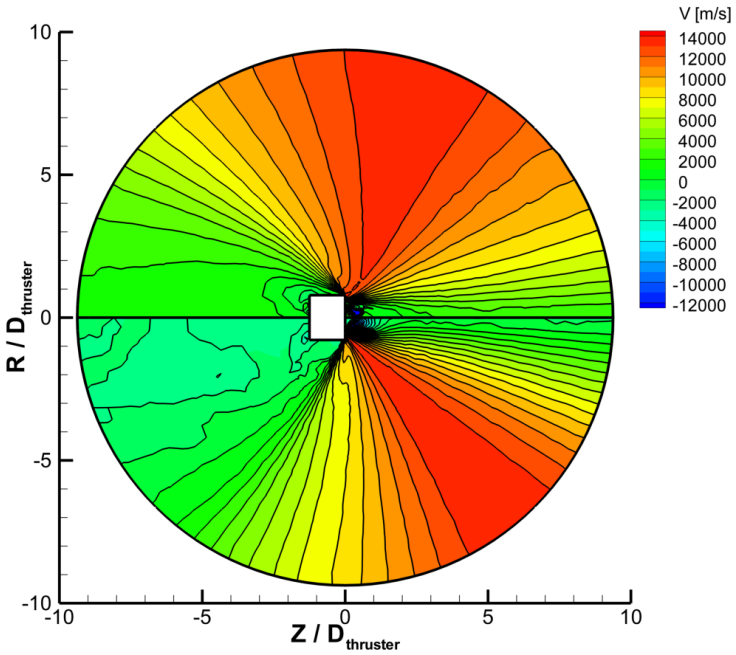

Figure 4.33: Comparison between MPIC1-simulation (bottom) and MPIC2-simulation (top): radial velocity contours of Xe^{2+}.

Thus, the main ion beam is more collimated as calculated by MPIC2-simulation than MPIC1-simulation.

Further, the magnitude of peak radial velocity is higher in MPIC2-simulation than MPIC1-simulation. The peak magnitude radial velocity is due primarily to CEX collisions in the near-field plume. MPIC2-simulation calculates post-scattering angles for CEX interactions utilizing a distribution that is more heavily weighted to low-angle scattering than the distribution used in MPIC1-simulation. Although the individual particles are scattered at low-angles in the center of mass (COM) frame, CEX collisions additionally swap particle charges. Thus, fast moving ions with low plume divergence angle as measured in the lab frame collide with slow moving background neutrals and scatter as fast moving neutrals moving at a low plume divergence angle; however, the background neutrals scatter as slow moving ions moving at a high plume divergence angle, as measured in the lab frame. This process is illustrated in Figure 4.34. Therefore, the peak radial velocity of Xe^{+} and

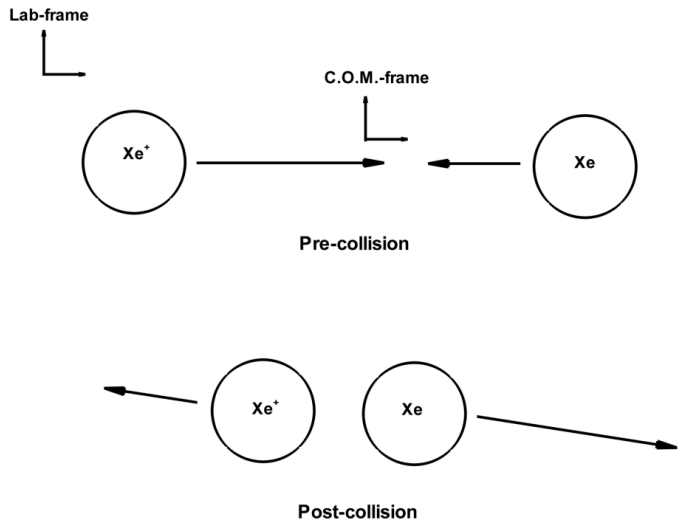

Figure 4.34: CEX collision schematic.

Xe^{2+} is increased in MPIC2-simulation relative to MPIC1-simulation, for the same reasons given above regarding the peak axial velocity.

Figures 4.35 and 4.36 illustrate angular distributions of axial and radial velocity along a 1 m arc for Xe^{+} and Xe^{2+}, respectively. Figures 4.35 and 4.36 show the same behavior described above: the peak magnitude of axial and radial velocity is increased in MPIC2-simulation relative to MPIC1-simulation.

4.3.2 Ion Number Density

In this section, number density data for the ionized heavy species particles are presented for MPIC1- and MPIC2-simulation. Field contours of Xe^{+} and Xe^{2+} number density are shown in Figures 4.37 and 4.38. Subsequent figures present data that are extracted from this field data. The primary difference between MPIC1-simulations and MPIC2-simulations is in the qualitative shape of the data. MPIC2-simulation calculates a number density field with a greater number of ions at higher plume divergence angles than MPIC1-simulation: the familiar CEX "wings" in MPIC2-simulation

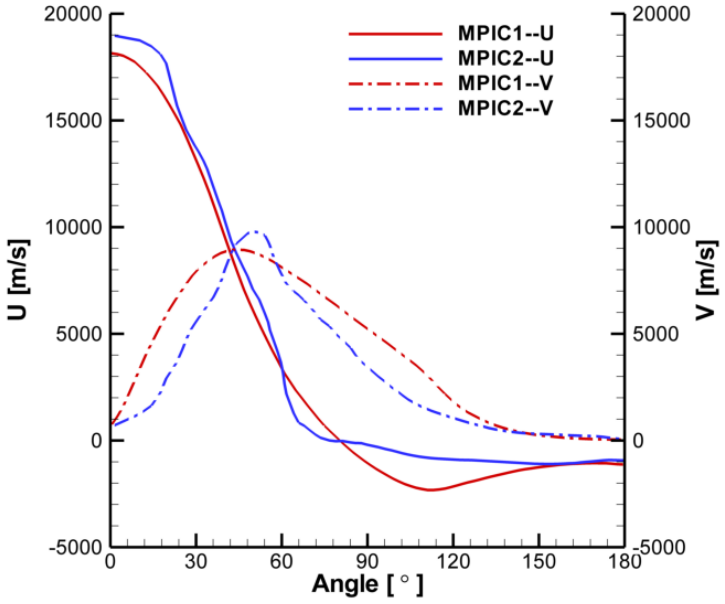

Figure 4.35: Comparison between MPIC1-simulation and MPIC2-simulation: axial and radial velocity distribution for Xe^{+}along a 1 m arc.

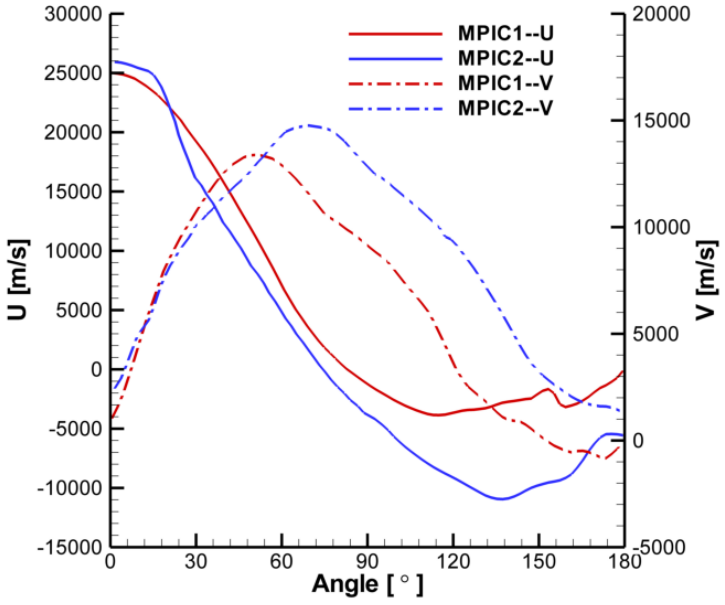

Figure 4.36: Comparison between MPIC1-simulation and MPIC2-simulation: angular axial and radial velocity profiles for Xe^{2+} along a 1 m arc .

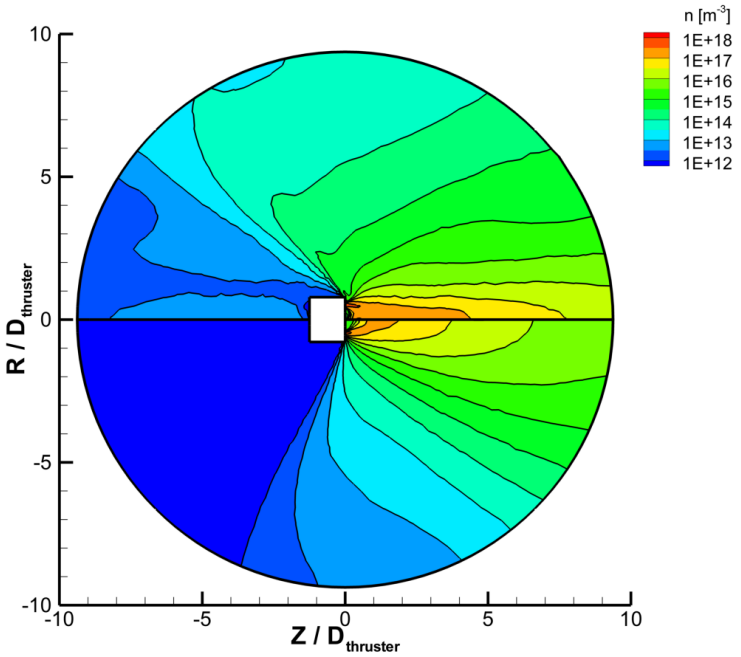

Figure 4.37: Comparison between MPIC1-simulation (bottom) and MPIC2-simulation (top): number density contours of Xe^+.

extend farther upstream of the TE plane than in MPIC1-simulation. This difference is due primarily to the difference in post-collision scattering angle distribution between MPIC1 and MPIC2, as explained in Section 4.3.1: MPIC2 utilizes a distribution that is weighted toward low-angle scattering more heavily than the MPIC1 distribution. The increased number density at high plume divergence angles is the effect of this difference in distribution, as shown in Figure 4.39.

4.3.3 Ion Current Density

In this section, ion current density data are presented for MPIC1- and MPIC2-simulation. Field contours of ion current density are shown in Figure 4.40. Subsequent far-field data are extracted from this field data. Note that axial and radial profiles of near-field ion current density calculated in MPIC2-simulation are very similar to those profiles calculated by MPIC1-simulation; as such, these profiles are shown in Section 4.4.1, alongside experimental data.

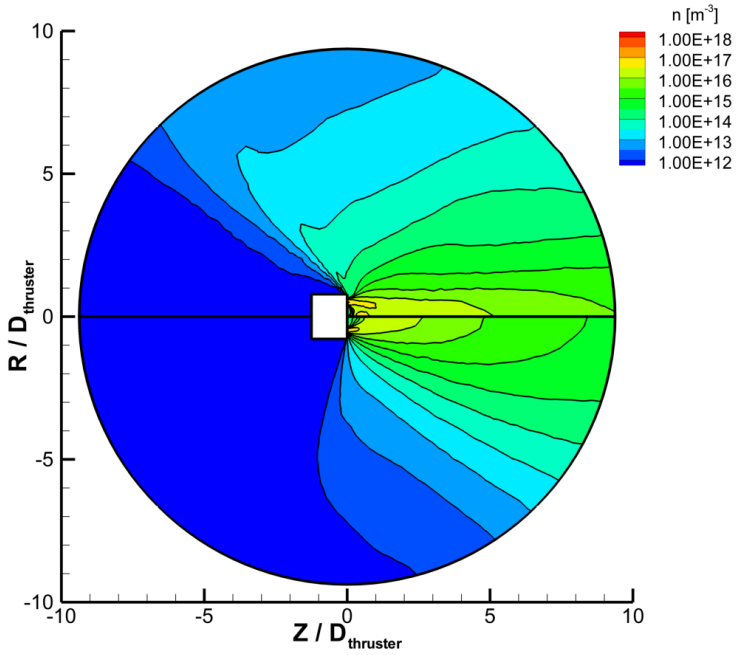

Figure 4.38: Comparison between MPIC1-simulation (bottom) and MPIC2-simulation (top): number density contours of Xe^{2+}.

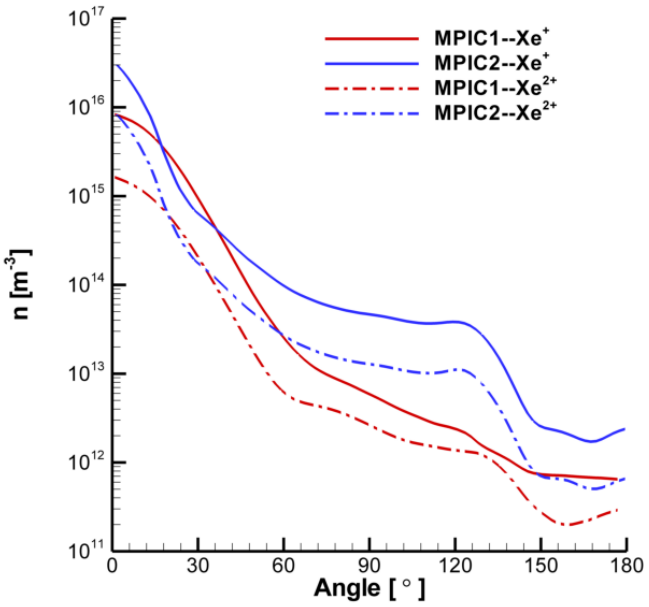

Figure 4.39: Comparison between MPIC1-simulation and MPIC2-simulation: angular ion number density profiles along a 1 m arc.

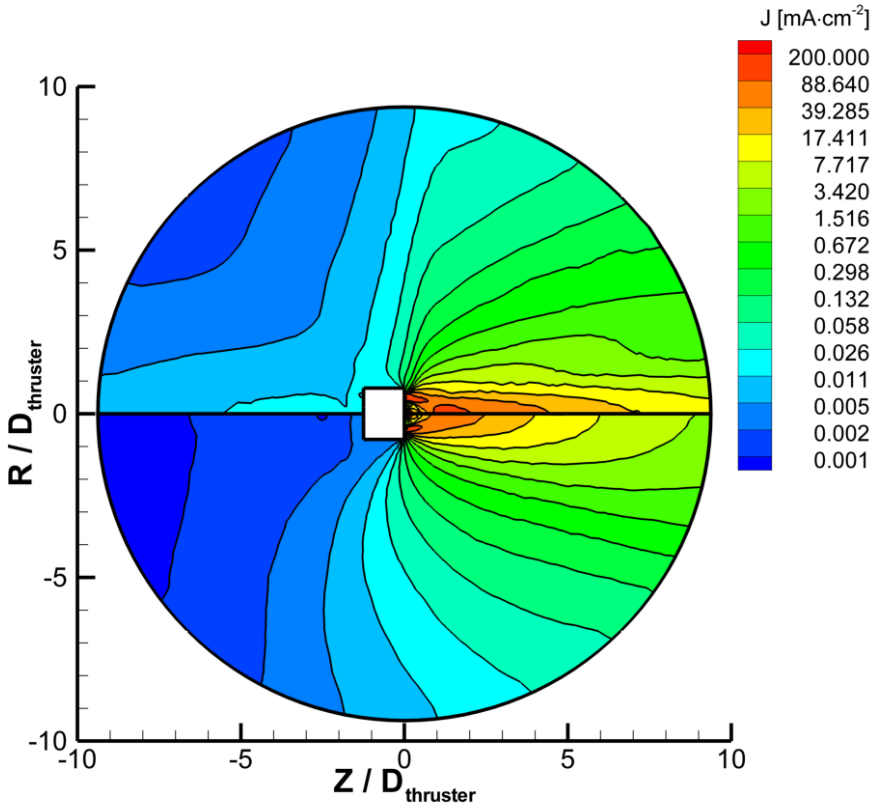

Figure 4.40: Comparison between MPIC1-simulation (bottom) and MPIC2-simulation (top): ion current density contours.

The main difference between MPIC1-simulations and MPIC2-simulations is exhibited in the far-field plume structure: at high plume divergence angles, MPIC2-simulation calculates an increased magnitude of ion current density relative to MPIC1-simulation. Additionally, MPIC2-simulation calculates a more collimated main beam of ions than MPIC1-simulation: MPIC2-simulation calculates a main ion beam which persists downstream farther than the beam calculated by MPIC1-simulation.

These two differences in plume structure correspond to the differences shown in Sections 4.3.1 and 4.3.2. The MPIC2 collision dynamics model effectively redistributes plume ions, focusing them more toward both lower and higher plume divergence angles and away from mid-range plume divergence angles, relative to MPIC1. Figure 4.41 illustrates this behavior: at angles less than 5°, MPIC2-simulation calculates an ion

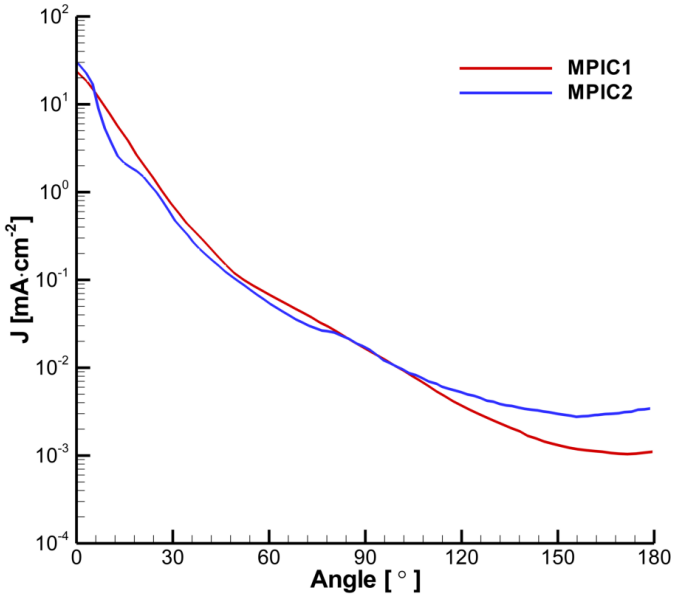

Figure 4.41: Comparison between MPIC1-simulation and MPIC2-simulation: angular ion current density profiles along a 1 m arc.

current density greater than that calculated by MPIC1-simulation; between 5°-80°, MPIC1-simulation calculates an ion current density greater than that calculated by MPIC2-simulation; and between 80°-150°, MPIC2-simulation again calculates an ion current density greater than MPIC1-simulation.

4.4 Comparing MPIC to Experimental Measurement

Experimental measurements of ion current density presented here are identical to those presented in Section 4.2.2. Ion current density measurements are acquired using the near- and far-field Faraday probe, as outlined in Section 1.1.2.4, where the uncertainty associated with the near-field probe measurements is ±10%, whereas the uncertainty associated with the far-field probe measurements is $\pm 0 - 50\%$ on the integrated beam current. The near-field data is presented first, followed by the far-field data.

4.4.1 Near-field Ion Current Density

Figure 4.42 shows comparison of the measurements to near-field ion current density calculations in MPIC2-simulation. The MPIC1-simulation results are identical to the MPIC1-H3 results shown in Section 4.2.2.1. MPIC2-simulation calculates near-field plume structure similar to that calculated by MPIC1-simulation: both simulations, as well as the experimental data, show the beam of ions at the TE plane to be highly collimated over the first mean thruster diameter. MPIC2-simulation generally overpredicts the magnitude of ion current density relative to MPIC1-simulation: at the location of peak measured ion current density in the main beam, $Z/D_{thruster} = 0.2$ and $R/D_{thruster} = 0.5$, the simulations calculate ion current densities of approximately 145 $\frac{mA}{cm^2}$ and 161 $\frac{mA}{cm^2}$ for MPIC1- and MPIC2-simulation respectively. The measured peak ion current density in the main beam is 128 $\frac{mA}{cm^2}$. As observed in Section 4.2.2.1, MPIC1-simulation calculates a higher peak ion current density than the measured peak, since MPIC2-simulation overpredicts ion current density relative to MPIC1-simulation in the near-field plume, MPIC2-simulation shows worse agreement with experimental data than MPIC1-simulation. Possible explanations of this general discrepancy are offered in Section 4.2.2.1, and are further applicable to MPIC2-simulation.

The axial profiles in Figure 4.43 show qualitative agreement between the measured data and the calculated ion current densities: for $Z/D_{thruster} > 0.3$, ion current density monotonically decreases. In general, MPIC1- and MPIC2-simulation show similar agreement with the measured data, although MPIC2-simulation overpredicts ion current density at $Z/D_{thruster} > 1.5$ to a greater degree than MPIC1, relative to the measured data. Typically, at $Z/D_{thruster} > 1.5$, the measurements show a higher rate of decay relative to either simulation. Additionally, between $Z/D_{thruster} = 0.05 - 0.2$, measured data actually shows an increase in ion current density, whereas both simulations calculate a decrease in ion current density due to the same limitations of the

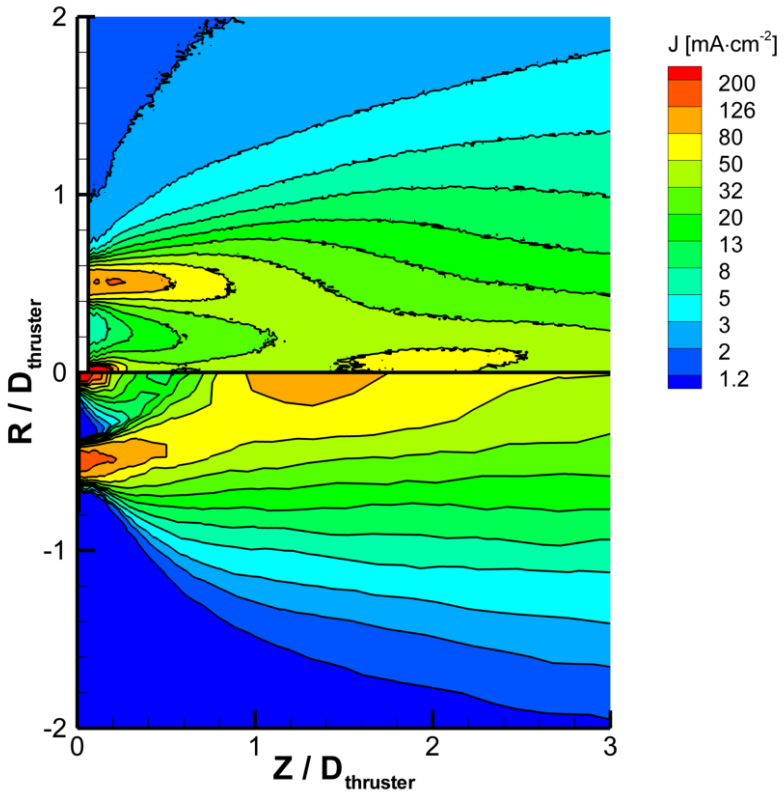

Figure 4.42: Comparison of ion current density between experimental measurements (top) and MPIC2-simulation (bottom).

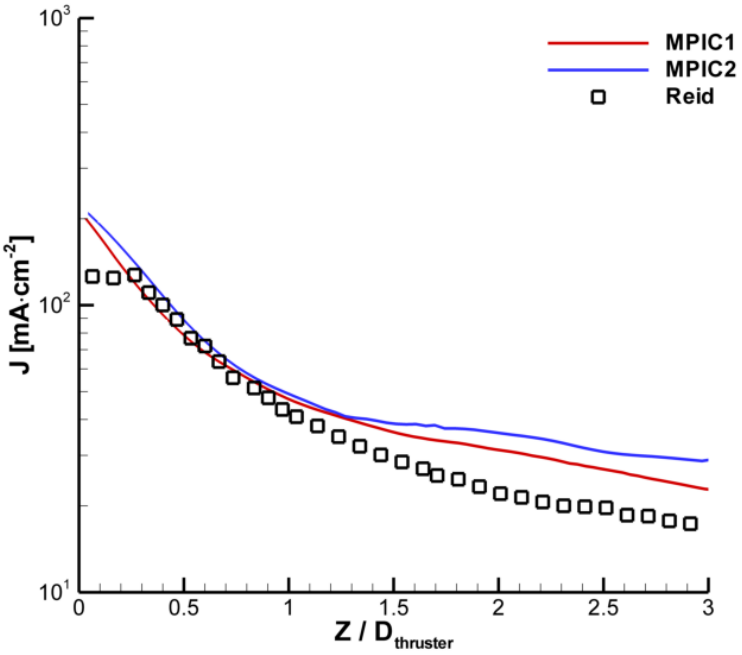

Figure 4.43: Comparison between MPIC1-simulation, MPIC2-simulation, and experimental measurements: axial ion current density variation along $R/D_{thruster} = 0.5$.

electron submodel discussed above.

Figures 4.44- 4.47 show radial profiles of ion current density as calculated by MPIC1- and MPIC2-simulation compared to measured data. Figure 4.20 shows radial profiles at an axial station of $Z/D_{thruster} = 0.08$. Agreement between the simulations and the measured data is similar to that discussed in Section 4.2.2.1. Both MPIC1- and MPIC2-simulation underpredict the centerline spike in ion current density in the near field plume, relative to the measured data. When compared to measured data, MPIC2-simulation underpredicts the magnitude of the centerline spike by approximately 28%. Possible explanations of this general discrepancy are offered in Section 4.2.2.1, and are further applicable to MPIC2-simulation. The second quantitative discrepancy between the measured and simulated profiles is the magnitude of the main beam ion current density, which was discussed above. Due to its collision model, MPIC2-simulation calculates a more highly collimated main ion beam

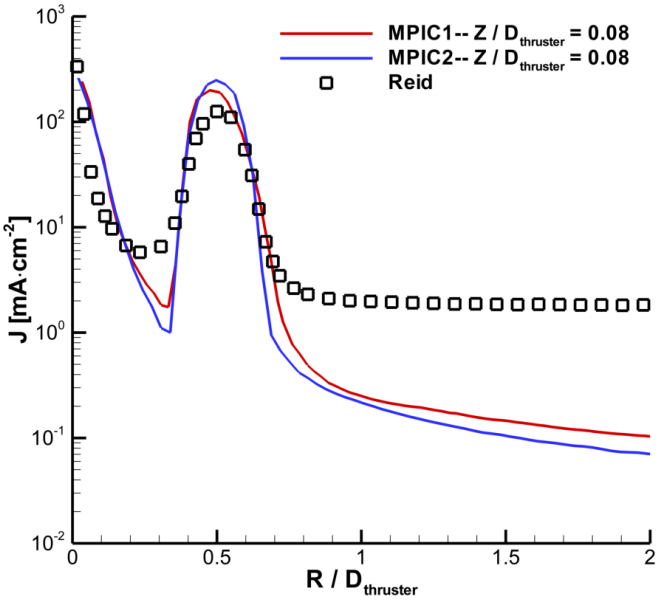

Figure 4.44: Comparison between MPIC1-simulation, MPIC2-simulation, and experimental measurements: radial ion current density variation along $Z/D_{thruster} = 0.08$.

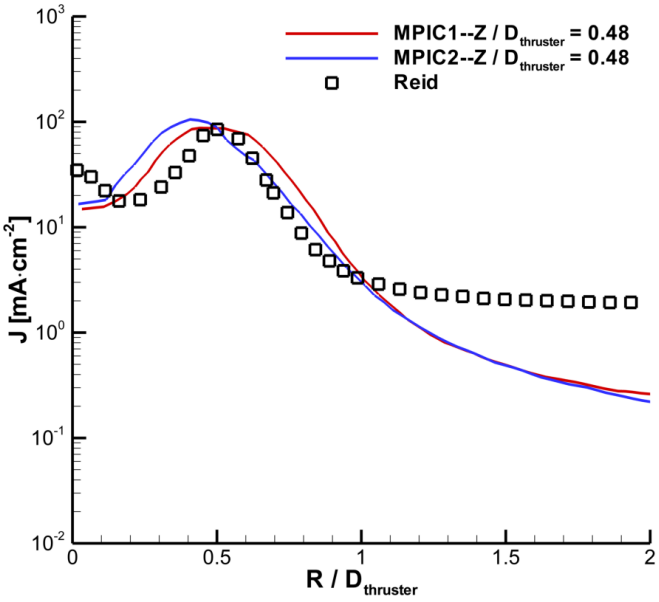

Figure 4.45: Comparison between MPIC1-simulation, MPIC2-simulation, and experimental measurements: radial ion current density variation along $Z/D_{thruster} = 0.48$.

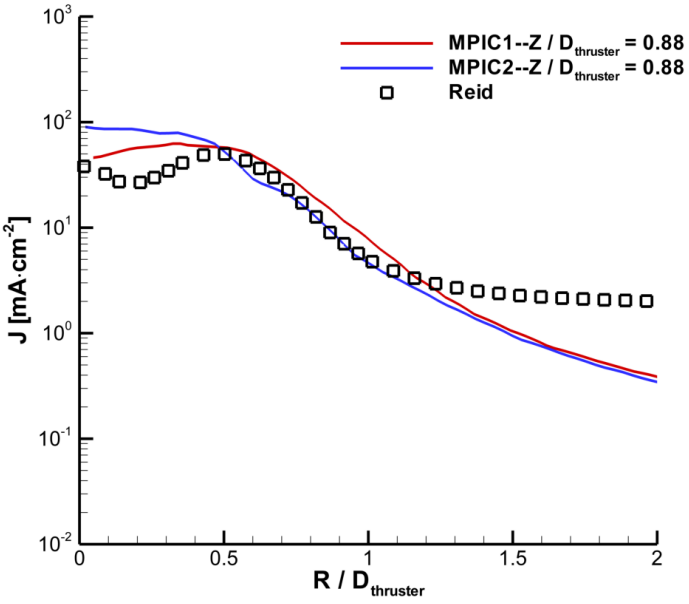

Figure 4.46: Comparison between MPIC1-H2, MPIC1-H3, and experimental measurements: radial ion current density variation along $Z/D_{thruster} = 0.88$.

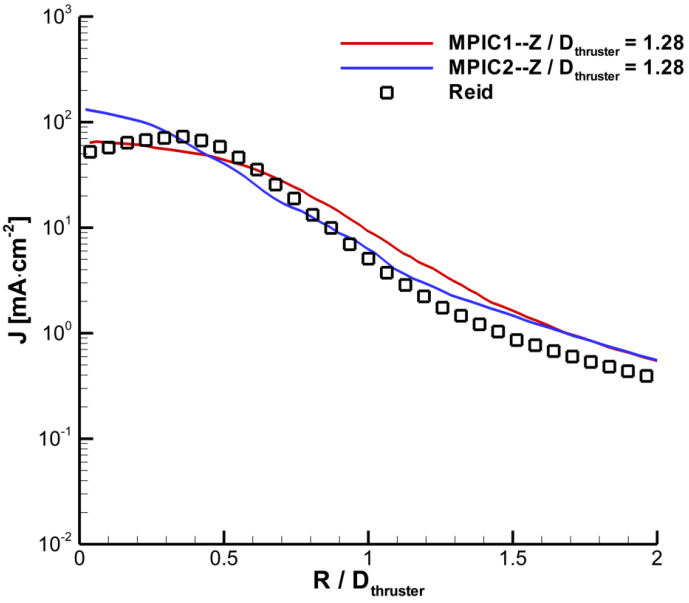

Figure 4.47: Comparison between MPIC1-simulation, MPIC2-simulation, and experimental measurements: radial ion current density variation along $Z/D_{thruster} = 1.28$.

than MPIC1-simulation, with the result that, in the near-field plume, agreement between MPIC2-simulation and measured data is not as good as agreement between MPIC1-simulation and measured data.

Figures 4.45- 4.47 show the behavior of radial profiles of ion current density as $Z/D_{thruster}$ increases. These figures show moderate qualitative agreement between simulation and measurements, similar to that discussed in Section 4.2.2.1. MPIC2-simulation does show better qualitative agreement with measured data than MPIC1-simulation as $Z/D_{thruster}$ increases.

4.4.2 Far-field Ion Current Density

Figure 4.48 shows comparisons of angularly resolved far-field ion current density. Qualitative agreement between MPIC1-simulation and experiment is as described in Section 4.2.2.1; MPIC2-simulation calculates larger ion current densities than MPIC1-simulation at low angles, i.e. plume divergence angles of 0°-10°. Between 10°-75°, MPIC2-simulation calculates a lower ion current density than MPIC1-simulation, and between 75°-150°, MPIC2-simulation again calculates a larger ion current density than MPIC1-simulation. MPIC2-simulation calculates an inflection point in ion current density variation at a lower angle than MPIC1: roughly 15°. This is in contrast to the measurements, which show an inflection point near 30°. The measurements also show a second inflection point near 60°, such that the exponential decay of current density occurs at three different rates as outlined above in Section 4.2.2.1. MPIC2-simulation calculates a second inflection point as well, at roughly 75°, such that ion current density exponentially decays at three different rates in the following ranges: 0°-15°, 20°-75°, and 80°-150°. Between 150°-180°, both the measured and the simulated profiles show CEX wings. The measured decay rate in the low-angle region shows better agreement with the decay rate calculated by MPIC1-simulation than the rate calculated by MPIC2-simulation, whereas the decay rates measured in the other

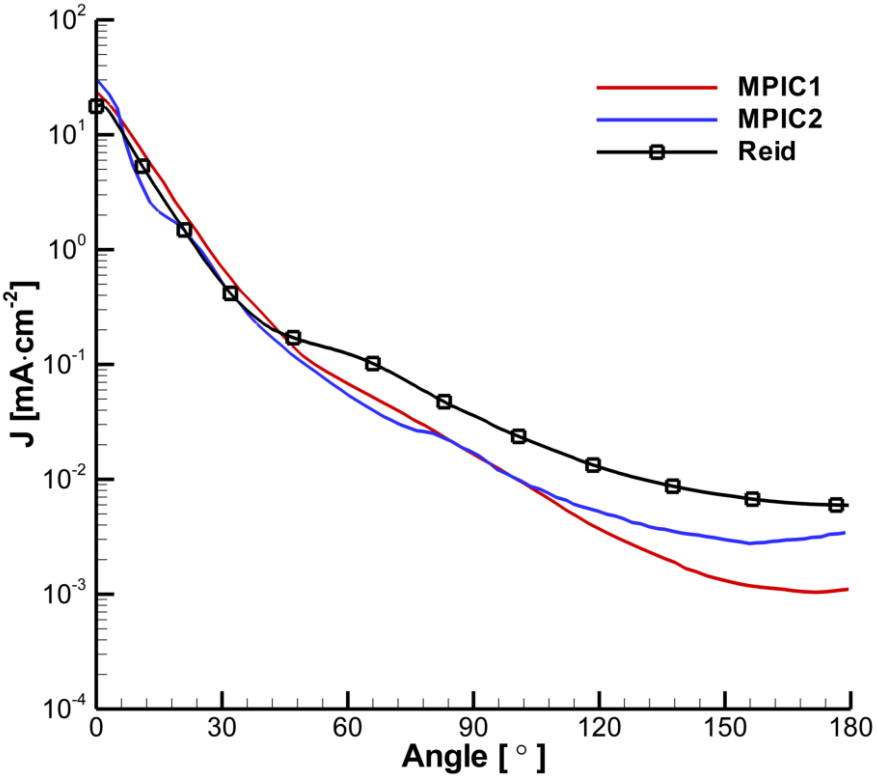

Figure 4.48: Comparison between MPIC1-simulation, MPIC2-simulation, and experimental measurements: angular variation of far-field ion current density along a 1 m circular arc.

two regions show better agreement with the rate calculated in MPIC2- rather than MPIC1-simulation. This results in MPIC2-simulation data overpredicting ion current density between 0°-15° and underpredicting between 60°-150°, relative to measured data. However, MPIC2-simulation shows two significant improvements over MPIC1-simulation: first, MPIC2-simulation shows excellent agreement with measured data between 15°-45°; second, although MPIC2-simulation underpredicts measured data at high divergence angles, MPIC2-simulation is in fact in much better agreement with the measurements than MPIC1: for example, relative to the measured data, MPIC1-simulation underpredicts ion current density approximately 81% at 150°, whereas MPIC2-simulation underpredicts measurements by approximately 52%.

The integrated ion beam currents based on the profiles in Figure 4.48 are as follows: integrating the MPIC1- and MPIC2-simulation profiles results in an ion beam current of approximately 18.0 A and 18.1 A, respectively; integrating experimental measurements results in an ion beam current of 21 A. The uncertainty associated with the integrated ion beam current ranges between $0 - 50\%$, which the calculated beam currents are both well within. Again, the total discharge current at the nominal operating condition is 20 A. Explanations for the differences between the total discharge current, measured integrated ion beam current, and simulated integrated ion beam current are suggested in Section 4.2.2.1.

4.4.3 Discussion

Comparisons between MPIC1- and MPIC2-simulation show moderate to good agreement with measured ion current density data. Near the TE plane, the magnitude of MPIC1-simulation ion current density calculations showed better agreement with measured ion current density magnitudes than MPIC2-simulation. However, MPIC2-simulation showed better agreement with measurements than MPIC1-simulation for the majority of the near-field plume. Further, MPIC2-simulation captured distinct trends in the far-field ion current density data, trends that are not resolved in MPIC1-simulation. Finally, MPIC2-simulation showed better agreement with ion current density measurements at high plume divergence angles, as shown in Figure 4.48, improving agreement with measured data by as much as 45%. Based on MPIC2-simulation's better agreement with measurements in these cases, the post-collision scattering model which MPIC2 utilizes more accurately characterizes the structure of the plume, especially at high divergence angles. However, although MPIC2-simulation provides results more accurate than MPIC1-simulation, significant differences still remain between the simulations and measurements regarding the overall plasma potential field, the magnitude of high divergence angle ion current density, and the

magnitude of the centerline spike in ion current density. An approach that investigates the first two items is considered in the next chapter.

CHAPTER V

Near-field Plume Characterization and Inflow Condition Mapping

In this chapter, further results of Hall thruster plume simulations are presented. The simulations are performed using the computer code MPIC in order to model the plasma plume of the 6 kW Hall thruster described in Chapter 3. In order to accurately predict plume structure while maintaining relatively low computational cost, MPIC neglects magnetic field effects. As shown in Chapter 4, this has a significant effect on plasma potential calculations in the near-field plume, such that agreement between simulated and measured plasma potential data is very poor. However, incorporating $\vec{B}$ field effects into MPIC significantly increases the computational wall time for each simulation [23]. Therefore, the present chapter investigates a method of mapping the TE plane of the Hall thruster under consideration onto a $\vec{B}$ field line that lies outside the strongest regions of the magnetic field. Mapping the inlet boundary onto a field line is performed using HPHall data, coupling HPHall and MPIC such that: *i*) the amount of computational wall time for MPIC simulation is not substantially increased, and *ii*) agreement between MPIC-simulated and measured plasma properties is improved, especially regarding plasma potential data.

This chapter is divided into three sections. First, simulation boundary conditions are detailed, with discussion centered on the mapping discussed above. Second, MPIC

results obtained using the empirically-based post-collision scattering angle distribution are compared: MPIC results that utilize the newly mapped inlet are compared to the results calculated using the previous domain. Third, these results are compared to experimental data in order to assess the accuracy of utilizing either domain. These comparisons are made by examining plasma properties in the near- and far-field of the plume. These comparisons are used in a detailed examination of the very near-field plume, where comparisons are made between MPIC, HPHall, and experimental data.

5.1 Inlet Mapping and Boundary Conditions

As outlined in Section 4.2.2.2, MPIC calculation of plasma potential shows poor agreement with measurements of plasma potential. This poor agreement is due to the fact that MPIC ignores the effect of magnetic fields. As a result, MPIC calculates gradients in plasma potential that are of a smaller magnitude than the gradients in the measured data. However, the strength of the magnetic field diminishes rapidly as distance from the TE plane increases. For the Hall thruster under consideration, the magnetic field strength diminishes by a factor of 8 between $Z/D_{thruster} = 1$, where the field strength is around 0.046 T, and $Z/D_{thruster} = 1.75$, where the field strength is around 0.006 T. Since HPHall does in fact account for the effect of magnetic field, accuracy in plume simulation can be gained by using HPHall to map the plume inflow boundary beyond the region of highest magnetic field strength: since the effect of the magnetic field is much smaller at the proposed inflow boundary, ignoring the magnetic field in plume simulations is more justifiable. Re-mapping the inflow boundary has one potential tradeoff in that additional time is spent producing the computational domain. However, this tradeoff is marginal: the increase in time required to produce the proposed domain is much smaller than the time required to incorporate magnetic field effects into MPIC plus the additional computational wall time.

Information from HPHall regarding the heavy species and the electron fluid is used

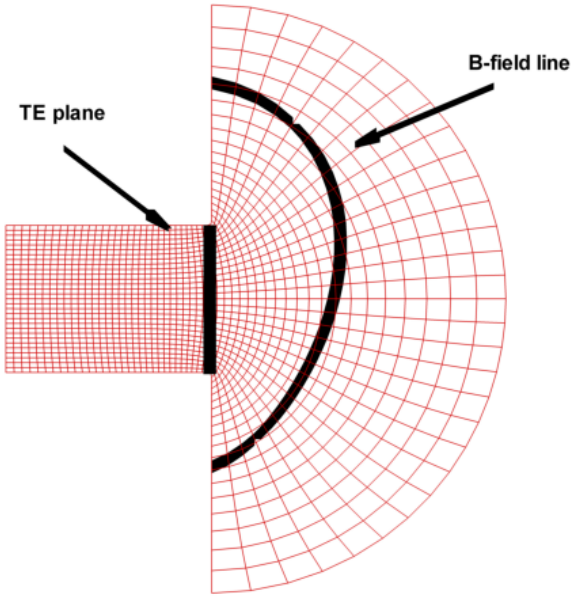

Figure 5.1: Magnetic field line in HPHall.

in order to map the inflow boundary to a region away from the peak magnetic field strength. Some possible mappings are eliminated straightaway due to the electron submodel HPHall utilizes: electron fluid information is only computed between the first and the last magnetic field lines. This eliminates, for example, a mapping of the inflow boundary in MPIC to the semi-circular outflow boundary in HPHall. Therefore, in order to map the inflow boundary as far away from the TE plane as possible while still providing the necessary information to MPIC, the MPIC inflow boundary is mapped to the farthest downstream magnetic field line in HPHall. Figure 5.1 shows the magnetic field line to which the MPIC inflow boundary is mapped, along which the magnetic field strength is around 10% of the maximum magnetic field strength; Figure 5.2 shows the proposed inflow boundary in MPIC, which has been mapped to the magnetic field line shown in Figure 5.1.

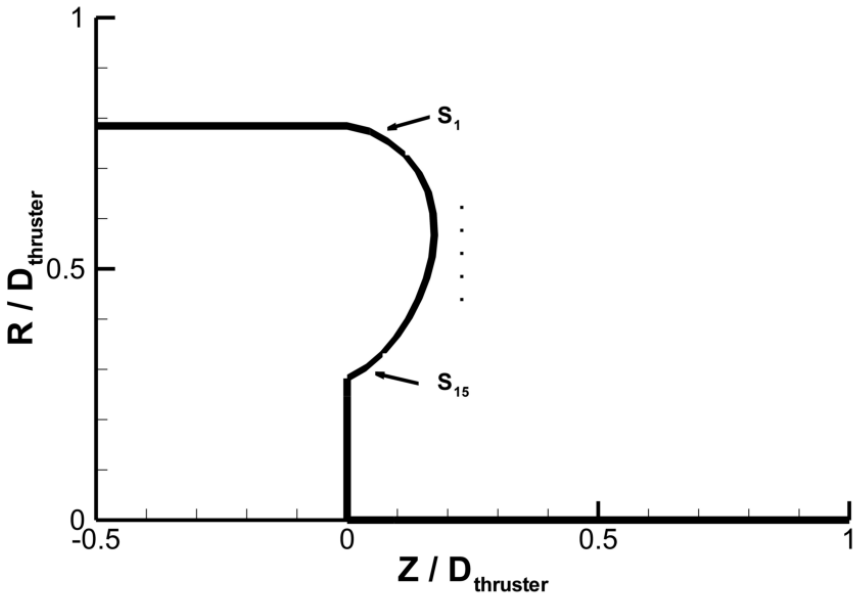

Figure 5.2: Proposed inflow boundary in MPIC.

Species	Location	U, m/s	V, m/s	T, K	n, m^{-3}
Xe	S_1	27	-33	440	2.88×10^{17}
	S_2	23	-31	450	2.81×10^{17}
	S_3	34	-9	650	2.91×10^{17}
	S_4	165	56	1500	3.89×10^{17}
	S_5	281	63	3100	4.40×10^{17}
	S_6	309	27	5400	3.94×10^{17}
	S_7	384	2	8250	3.58×10^{17}
	S_8	660	-6	10100	3.38×10^{17}
	S_9	449	-12	9700	3.44×10^{17}
	S_{10}	430	-25	7700	3.80×10^{17}
	S_{11}	411	-62	5450	4.47×10^{17}
	S_{12}	352	-104	3150	4.58×10^{17}
	S_{13}	67	-12	1250	2.39×10^{17}
	S_{14}	47	17	680	2.45×10^{17}
	S_{15}	59	23	550	2.71×10^{17}
	Cathode	320	0	1300	1.78×10^{20}

Table 5.1: Xe inflow conditions at the proposed inflow geometry.

The proposed inflow boundary is constituted by 15 line segments, S_1-S_{15}, in order to closely map onto the magnetic field line extracted from HPHall. As outlined in Section 4.1, simulation of the thruster under consideration requires specifying boundary conditions at the inflow boundary, outflow surfaces, the chamber centerline, cathode, and along the thruster wall, for both the heavy species submodel and the electron submodel. Inflow boundary conditions for the heavy species submodel are presented first, followed by those for the electron submodel. All other boundary conditions are handled in the same manner as described in Section 4.1.

The macroscopic plasma properties required at the inflow boundary are the number density, bulk velocity components, and the temperature of each heavy species in the simulation. The proposed inflow boundary is discretized into fifteen segments as shown in Figure 5.2. The tabulated inflow properties listed in Tables 5.1-5.3 are extracted from H3 for the proposed geometry.

The boundary conditions for the detailed-fluid model must be determined in order to solve the conservation equations shown in Section 2.3.2.2. Since each equation is

Species	Location	U, m/s	V, m/s	T, K	n, m^{-3}
Xe^{+}	S_1	-1310	4250	71700	4.46×10^{15}
	S_2	830	6020	162000	6.48×10^{15}
	S_3	4620	7100	257000	1.17×10^{16}
	S_4	9480	6510	284000	2.21×10^{16}
	S_5	14200	4440	216000	5.35×10^{16}
	S_6	16400	1930	146000	1.33×10^{17}
	S_7	17300	160	122000	2.58×10^{17}
	S_8	18000	-660	85800	3.27×10^{17}
	S_9	17900	-1080	87400	3.39×10^{17}
	S_{10}	17000	-1730	119000	2.99×10^{16}
	S_{11}	15800	-3330	170000	1.51×10^{17}
	S_{12}	12200	-5520	251000	6.30×10^{16}
	S_{13}	6980	-7420	256000	2.47×10^{16}
	S_{14}	530	-5810	87900	1.06×10^{16}
	S_{15}	-1940	-4340	21000	7.35×10^{15}
	Cathode	0	0	0	0

Table 5.2: Xe^{+} inflow conditions at the proposed inflow geometry.

Species	Location	U, m/s	V, m/s	T, K	n, m^{-3}
Xe^{2+}	S_1	-1790	8340	110000	3.76×10^{14}
	S_2	1030	9980	190000	5.62×10^{14}
	S_3	5240	10330	301550	9.47×10^{14}
	S_4	11200	9300	422270	1.87×10^{15}
	S_5	17200	6440	447100	4.59×10^{15}
	S_6	21200	2950	346030	1.29×10^{16}
	S_7	22900	300	273260	3.14×10^{16}
	S_8	23700	-930	216760	4.82×10^{16}
	S_9	23500	-1660	223260	4.87×10^{16}
	S_{10}	22000	-2630	312250	6.40×10^{16}
	S_{11}	19300	-4640	423540	1.43×10^{16}
	S_{12}	14000	-7610	491670	5.47×10^{15}
	S_{13}	6780	-9670	386650	2.34×10^{15}
	S_{14}	470	-8800	216860	1.25×10^{15}
	S_{15}	-2960	-6810	140330	9.10×10^{14}
	Cathode	0	0	0	0

Table 5.3: Xe^{2+} inflow conditions at the proposed inflow geometry.

Species	Location	ϕ, V	$\nabla\psi$, $m^{-2}\,s^{-1}$	T_e, eV
e^-	S_1	5.1	-4.114×10^{20}	6.05
	S_2	6.1	-8.425×10^{20}	6.12
	S_3	8.5	-1.818×10^{21}	6.08
	S_4	12.3	-1.815×10^{21}	6.07
	S_5	17.6	-2.789×10^{21}	6.08
	S_6	23.3	-2.720×10^{20}	6.04
	S_7	27.3	5.553×10^{21}	6.09
	S_8	29.1	1.487×10^{22}	6.04
	S_9	29.5	1.005×10^{22}	6.13
	S_{10}	27.5	6.261×10^{21}	6.21
	S_{11}	23.5	9.088×10^{19}	6.11
	S_{12}	18.2	-1.639×10^{21}	6.04
	S_{13}	13.2	-1.010×10^{21}	6.01
	S_{14}	8.1	-7.972×10^{20}	6.07
	S_{15}	6.2	-3.144×10^{20}	5.94
	$Cathode$	4	3.251×10^{24}	3.0
	$Wall$	0	0	0
	$Symmetry$	0	0	0
	$Outflow$	0	0	3.0

Table 5.4: Electron submodel inflow conditions at the proposed inflow geometry.

Laplace-like, each one requires specification of either a Dirichlet (direct) value, or a von Neumann (gradient) value. Thus the plasma potential, the electron temperature, and the quantity $\nabla\psi$, i.e. $n_e v_{e,\hat{n}}$, are specified as either direct or gradient values at each boundary in the simulation. All boundary condition types are determined as specified in Section 4.1. The value to which each is set for the proposed inflow geometry is specified in Table 5.4.

5.2 Plume Simulations Utilizing the Proposed Inflow Geometry

The plume simulations presented in this section use both the MPIC1 and MPIC2 heavy species submodels as outlined in Section 2.2.4.2 and the detailed fluid electron submodel as outlined in Section 2.3.2.2. Naming conventions are identical to those

detailed in Chapter 4 regarding MPIC1- and MPIC2-simulation; plume simulations utilizing the MPIC2 heavy species submodel in conjunction with the proposed inflow boundary based on magnetic field lines are dubbed "MPIC3-simulation(s)." The numerical details are identical to those described in Sections 4.2 and 4.3: simulations run for 350,000 timesteps to reach a steady state and then for another 100,000 timesteps to sample macroscopic data, resulting in a total of approximately 2.5 million particles at steady state. The new computational domain consists of 3,012 triangular cells. The timestep size is 1×10^{-7} seconds, resulting in a total sampling time of 0.01 seconds. All simulations are run in parallel on the Nyx cluster, utilizing 32 processors. Computational wall time for MPIC1-simulation is around 12 hours; wall time for MPIC2- and MPIC3-simulations is around 15 hours.

As in Chapters 3 and 4, all results in this chapter use spatial coordinates that are normalized by a characteristic length associated with the thruster, in this case, the mean thruster diameter. Comparisons between the plume simulations are made through examining the following macroscopic plasma properties: ion current density, plasma potential, and electron temperature. The comparisons focus primarily on the near-field plume region, between 0-3 mean thruster diameters downstream of the TE plane, and between 0-2.5 mean thruster diameters radially from the thruster centerline. There is an additional comparison made using far-field plume data taken in a 180° circular arc with a radius of approximately 1 m and an origin near the TE plane. All comparisons are depicted in Figure 4.2.

5.2.1 Ion Current Density

In this section, ion current density results are presented. Field contours of ion current density are shown in Figure 5.3. Subsequent figures present data that are extracted from this field data. There are two significant differences between MPIC2- and MPIC3-simulations: the magnitude of the peak ion current density, and far-field

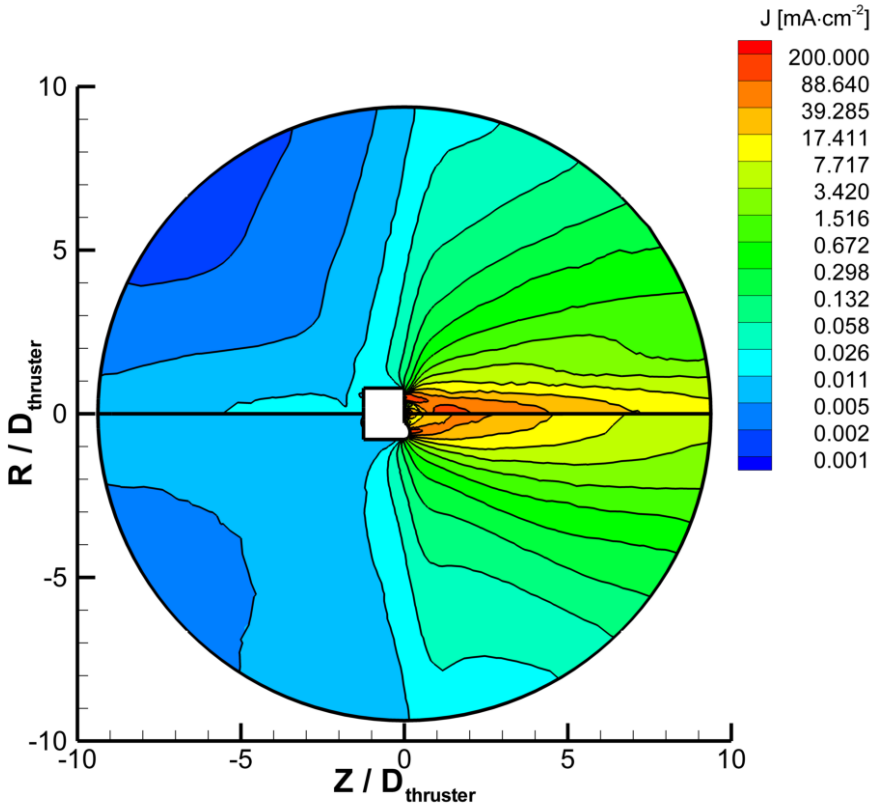

Figure 5.3: Comparison between MPIC2- (top) and MPIC3-simulation (bottom): ion current density contours.

ion current density structure. MPIC3-simulation calculates a peak ion current density 4.5% lower than MPIC2-simulation, relative to MPIC2. However, the difference in peak ion current density is somewhat artificial: the location of peak ion current density in MPIC2-simulation is 0.05 mean thruster diameters downstream of the TE plane, along the acceleration channel centerline. The domain of the MPIC3-simulations is mapped such that, along the acceleration channel centerline, the domain begins at approximately 0.15 mean thruster diameters downstream of the TE plane. Thus, the region of peak ion current density in MPIC2-simulation is effectively passed over in MPIC3-simulation.

The second significant difference between MPIC2- and MPIC3-simulation is in the structure of the far-field ion current density contours. In general, the magnitude of ion

current density at high plume divergence angles is larger in MPIC3-simulation than in MPIC2-simulation. This is due to the inflow conditions mapped onto the proposed geometry: these conditions are determined by particle information extracted from H3. Since H3 accounts for magnetic field effects, a larger gradient in plasma potential is calculated in H3 in the region between the TE plane and the final magnetic field line than is calculated in MPIC2. Therefore, H3 macroparticles traveling between the TE plane and the magnetic field line are overaccelerated relative to MPIC macroparticles traversing the same region, resulting in an increase in initial plume divergence calculated in MPIC3-simulation relative to MPIC2-simulation.

Figures 5.4- 5.7 illustrate quantitative differences between the MPIC1-, MPIC2-, and MPIC3-simulations. Figure 5.4 shows the axial variation of ion current density along the thruster's acceleration channel CL. The MPIC3-simulation calculates a lower ion current density near the TE plane relative to MPIC1- and MPIC2-simulation. In all simulations, the ion current density monotonically decreases as $Z/D_{thruster}$ increases. Between $Z/D_{thruster} = 0.5 - 1$, MPIC3-simulation calculates a slower decay in ion current density than MPIC1- and MPIC2-simulation; however, at $Z/D_{thruster} > 1.5$, MPIC3-simulation calculates a decay similar to MPIC1- and MPIC2-simulation.

Figures 5.5- 5.7 show radial variations of ion current density at different axial stations. Trends are similar between MPIC1-, MPIC2-, and MPIC3-simulation, with MPIC3-simulation typically calculating ion current densities that are lower in magnitude than MPIC1- and MPIC2-simulation. Further, MPIC3-simulation typically calculates narrower profiles than either MPIC1 or MPIC2. This is likely due to the calculated plasma potential in MPIC3: the plasma potential has a dynamic range of around 15 V, as opposed to MPIC1- and MPIC2-simulation, which calculate a dynamic range of around 100 V for plasma potential. The smaller dynamic range in MPIC3-simulation results in typically smaller gradients in plasma potential and

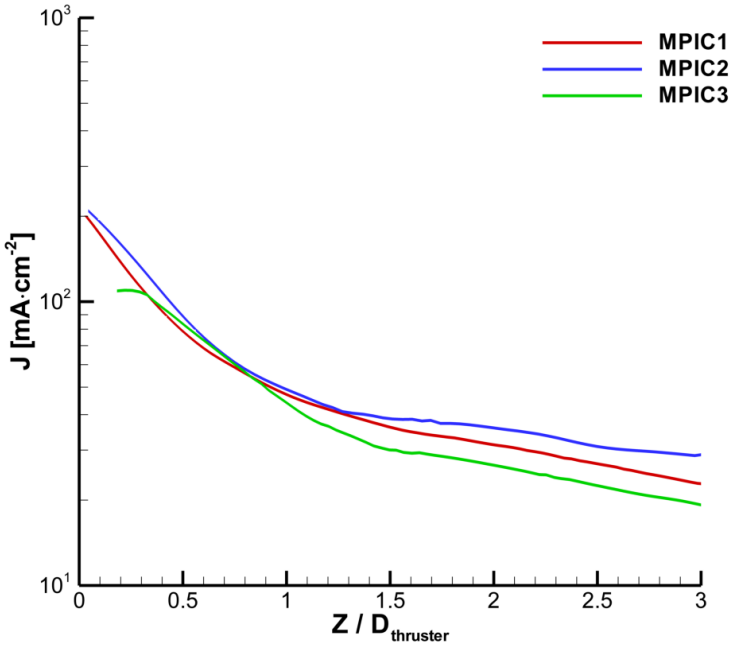

Figure 5.4: Comparison between MPIC1-, MPIC2-, and MPIC3-simulation: axial ion current density variation along $R/D_{thruster} = 0.5$.

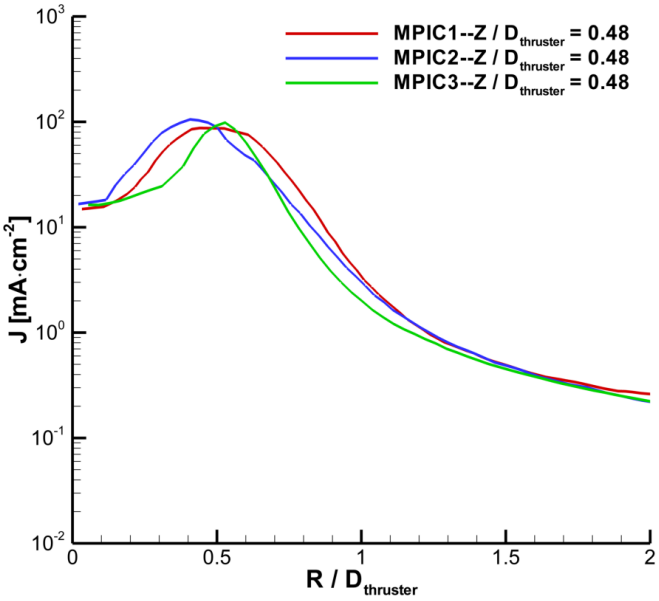

Figure 5.5: Comparison between MPIC1-, MPIC2-, and MPIC3-simulation: radial ion current density variation along $Z/D_{thruster} = 0.48$.

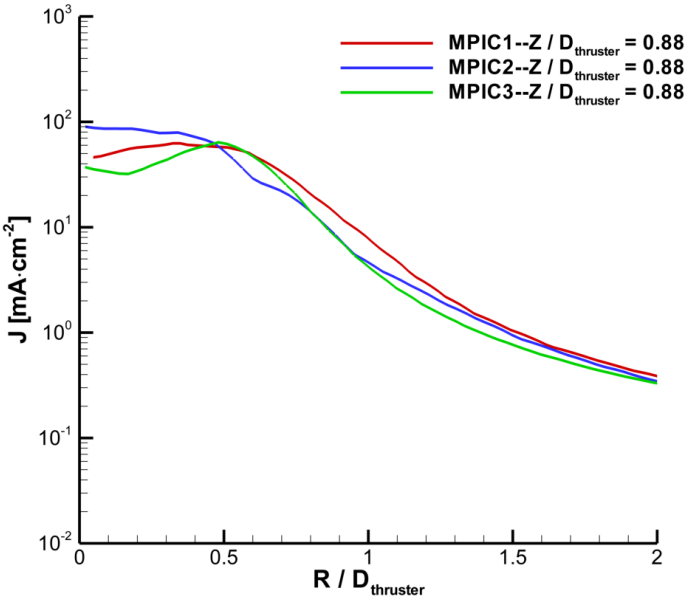

Figure 5.6: Comparison between MPIC1-, MPIC2-, and MPIC3-simulation: radial ion current density variation along $Z/D_{thruster} = 0.88$.

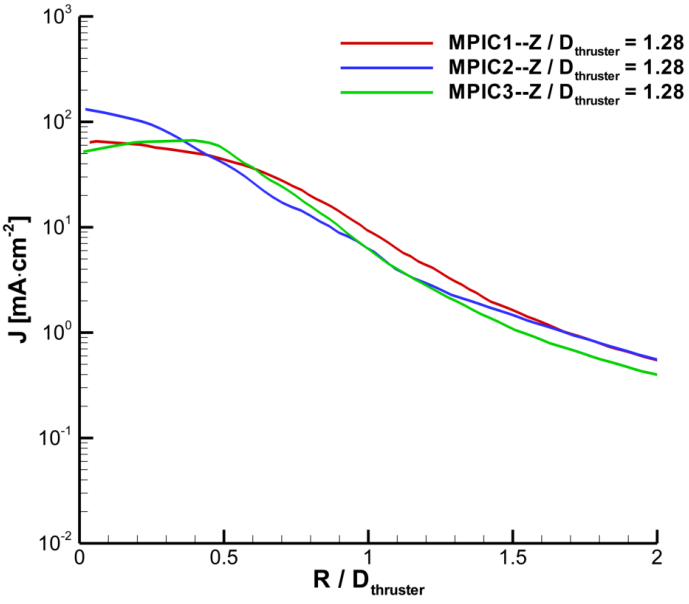

Figure 5.7: Comparison between MPIC1-, MPIC2-, and MPIC3-simulation: radial ion current density variation along $Z/D_{thruster} = 1.28$.

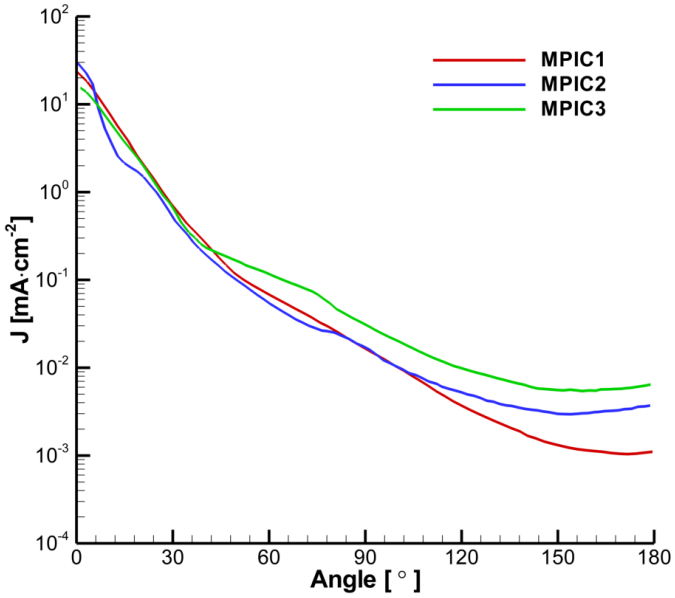

Figure 5.8: Comparison between MPIC1-, MPIC2-, and MPIC3-simulation: far-field ion current density angular variation along a 1 m circular arc.

less plume divergence downstream of the inflow boundary, relative to MPIC1- and MPIC2-simulation.

Figure 5.8 shows angularly resolved ion current density data along a 1 m circular arc. MPIC3-simulation calculates a profile most similar to the MPIC2-simulation profile: between 0°-30°, ion current density decays exponentially. There is an inflection point around 35° such that the profile transitions to an exponential decay at a different rate between 40°-70°. MPIC3-simulation calculates a second inflection point, similar to MPIC2-simulation, at roughly 70°, such that ion current density exponentially decays at three different rates in the following ranges: 0°-35°, 45°-70°, and 75°-150°. At angles greater than 150°, CEX wings constitute the bulk of the ion current density for each simulation.

At low angles, MPIC3-simulation calculates a lower ion current density than either MPIC1 or MPIC2; however, at angles larger than 45°, MPIC3 calculates a larger ion current density than either MPIC1 or MPIC2. This is consistent with the explanation

given above regarding the initial plume divergence at inflow boundaries: MPIC3-simulation calculates a larger initial plume divergence than MPIC2, resulting in lower ion current densities at low angles and larger ion current densities at higher angles, relative to MPIC2.

5.2.2 Plasma Potential

In this section, plasma potential results are presented. No field data comparisons of plasma potential are presented as the plasma potential data calculated by MPIC1- and MPIC2-simulation are larger than the plasma potential data calculated by MPIC3 to the degree that meaningful comparisons cannot be made. Figures 5.9- 5.12 illustrate qualitative differences between the plume simulations. Figure 5.9 shows the axial variation of plasma potential along the thruster's acceleration channel CL. The primary difference between simulations is in the magnitude of the plasma potential in the near-field. As stated in Chapter 4, both MPIC1- and MPIC2-simulation calculate plasma potentials well above the measured data, primarily due to the fact that magnetic field effects are ignored. However, based on HPHall results, MPIC3-simulation utilizes plasma potential data nearly an order of magnitude smaller than MPIC1 or MPIC2: Figure 5.9 shows the uniform axial profile calculated by MPIC3-simulation. Since MPIC3-simulation utilizes a domain outside of the regions of highest magnetic field strength, the magnitude of calculated plasma potential, as well as gradients in plasma potential, is lower in MPIC3 than in MPIC1 or MPIC2.

Figures 5.10- 5.12 show radial variations of plasma potential at different axial stations. In all cases, MPIC3-simulation calculates profiles that are disparate with those calculated by MPIC1 and MPIC2. For example, at axial stations of $Z/D_{thruster} = 0.88$ and $Z/D_{thruster} = 1.28$, MPIC1- and MPIC2-simulation calculate a uniform decay with increasing $R/D_{thruster}$, whereas the MPIC3 profiles show decreasing amounts of radial variation, eventually reaching a nearly constant value of

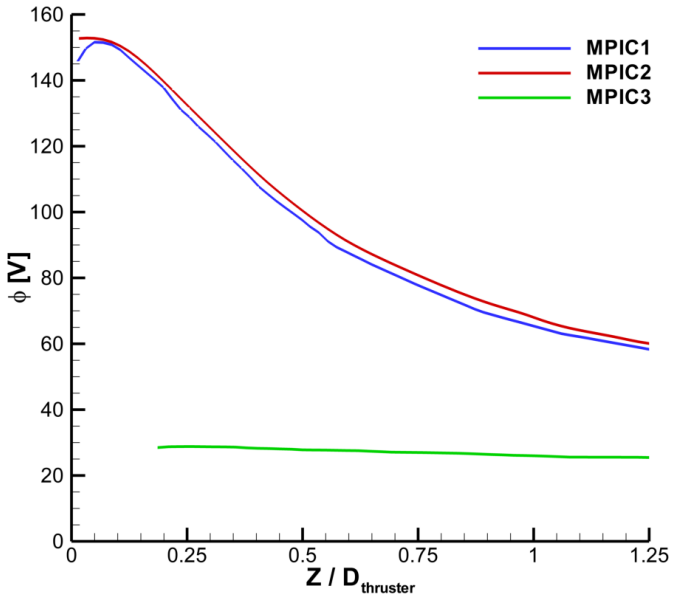

Figure 5.9: Comparison between MPIC1-, MPIC2-, and MPIC3-simulation: axial plasma potential variation along $R/D_{thruster} = 0.5$.

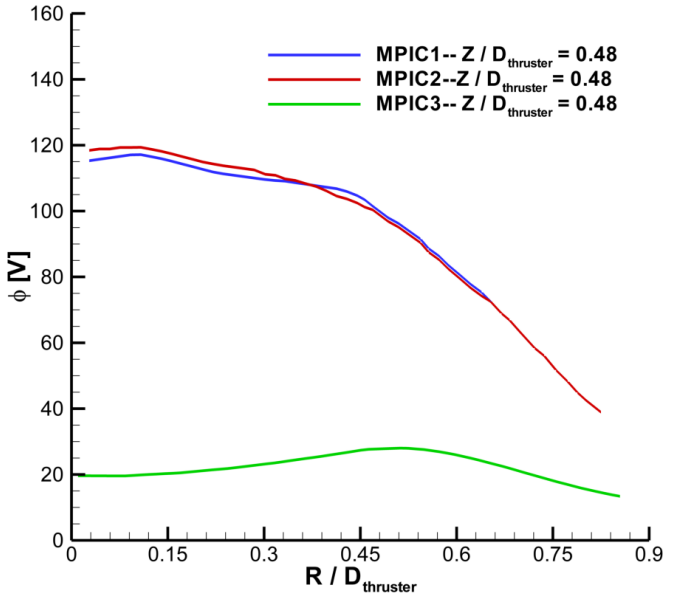

Figure 5.10: Comparison between MPIC1-, MPIC2-, and MPIC3-simulation: radial plasma potential variation along $Z/D_{thruster} = 0.48$.

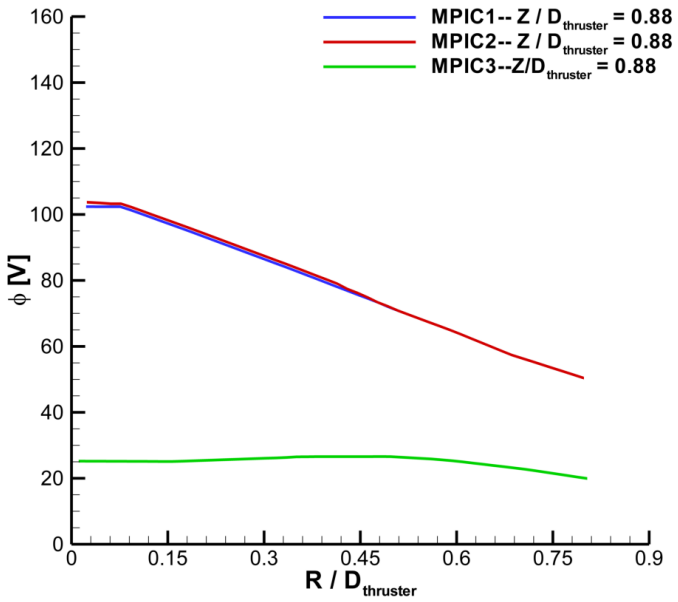

Figure 5.11: Comparison between MPIC1-, MPIC2-, and MPIC3-simulations: radial plasma potential variation along $Z/D_{thruster} = 0.88$.

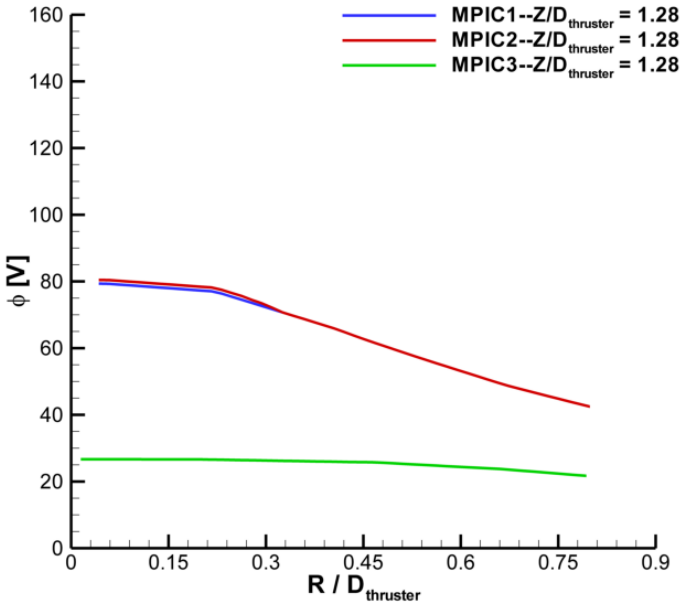

Figure 5.12: Comparison between MPIC1-, MPIC2-, and MPIC3-simulation: radial plasma potential variation along $Z/D_{thruster} = 1.28$.

about 27 V, similar to the trends in experimental data observed in Section 4.2.2.2. Quantitative trends are similar to those seen in Figure 5.9: in the near-field, profiles of plasma potential calculated by MPIC1 and MPIC2 significantly overpredict the profiles calculated by MPIC3; as $Z/D_{thruster}$ increases, these differences diminish due to the decay in the radial direction which MPIC1- and MPIC2-simulation calculate but is not observed in MPIC3-simulation.

5.2.3 Electron Temperature

In this section, electron temperature results are presented. No field data comparisons of electron temperature are presented as the electron temperature results calculated by MPIC1- and MPIC2-simulation are larger than the temperature calculated by MPIC3 to the degree that meaningful comparisons cannot be made. As shown in comparing Tables 4.1 and 5.1, the electron temperature at the inflow boundary as utilized in MPIC3-simulation is significantly lower than that utilized in MPIC1- and MPIC2-simulation. This results in similar trends between MPIC1, MPIC2-, and MPIC3-simulation, with the sole difference being the magnitude of the calculated temperature.

Figures 5.13, 5.14, and 5.15 illustrate quantitative differences between the two plume simulations. Figure 5.13 shows the axial variation of electron temperature along the thruster's acceleration channel CL. The MPIC1- and MPIC2-simulation calculate a higher electron temperature in the near-field relative to MPIC3-simulation. The constant $R/D_{thruster} = 0.5$ results show similar behavior in all simulations: the electron temperature monotonically decreases as $Z/D_{thruster}$ increases.

Figures 5.14 and 5.15 show radial variations of electron temperature at different axial stations. General trends correspond with results presented in Section 4.2.1.3: a significantly larger electron temperature is calculated in MPIC1- and MPIC2-simulation relative to MPIC3-simulation, and temperature uniformly decreases as

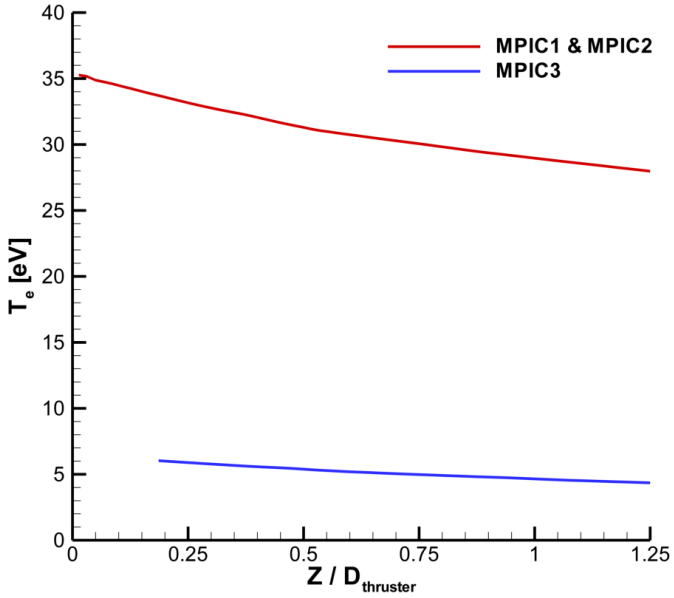

Figure 5.13: Comparison between MPIC1-, MPIC2-, and MPIC3-simulation: axial electron temperature variation along $R/D_{thruster} = 0.5$.

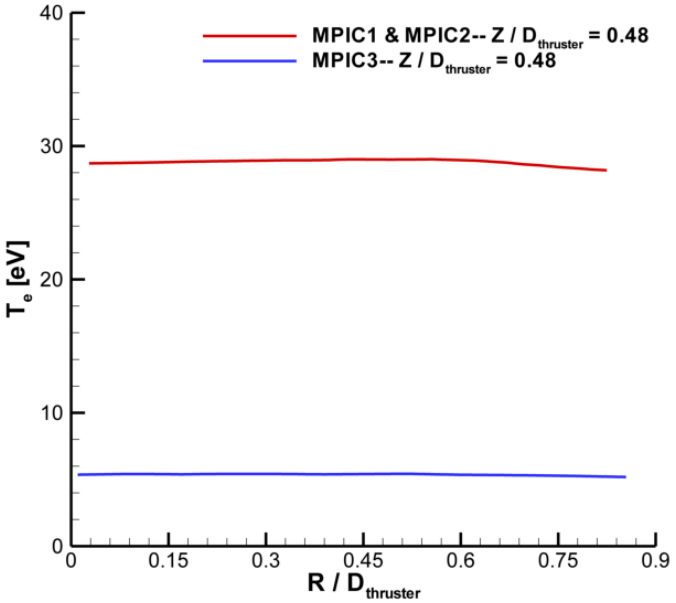

Figure 5.14: Comparison between between MPIC1-, MPIC2-, and MPIC3-simulation: radial electron temperature variation along $Z/D_{thruster} = 0.48$.

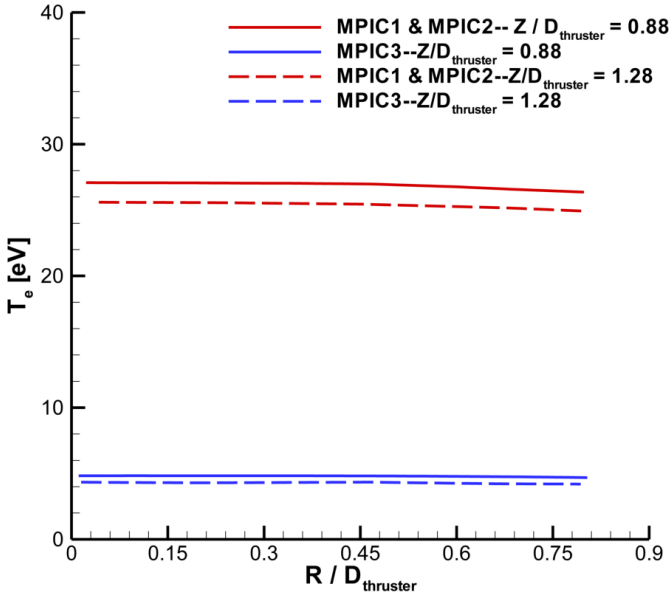

Figure 5.15: Comparison between MPIC1-, MPIC2-, and MPIC3-simulation: radial electron temperature variation along $Z/D_{thruster} = 0.88$ and $Z/D_{thruster} = 1.28$.

axial and radial distance from the inflow boundary increases.

5.2.4 Discussion

In general, MPIC3-simulation calculates results that are qualitatively different from MPIC2-simulation. The primary differences between the two simulations is in the initial plume divergence and the plasma potential magnitude at the inflow boundary. First, the proposed inflow boundary initializes the MPIC3-simulation with a larger degree of plume divergence than is utilized in MPIC2. Second, the higher magnitude potential in MPIC2-simulation produces larger gradients in the plasma potential field, relative to MPIC3-simulation. These larger gradients increase plume divergence as the plume develops. These two differences are competing effects: MPIC3-simulation typically calculates lower magnitude ion current densities in the near-field, relative to MPIC2, due to the first effect, whereas MPIC3-simulation typically calculates smaller gradients in ion current density, relative to MPIC2, due to

the second effect. In the next section, simulated results are compared to experimental measurements in order to evaluate these differences.

5.3 Comparing Plume Simulations to Experimental Measurement

In this section, MPIC1-, MPIC2-, and MPIC3-simulation calculations of ion current density and plasma potential are compared to experimental measurements. The ion current density measurements that are compared against were provided by PEPL, whereas the plasma potential comparisons were provided by JPL.

5.3.1 Ion Current Density

Experimental measurements of ion current density were performed by B. Reid [8]. The ion current density measurements were taken using the two Faraday cup probes outlined in Section 1.1.2.4. The uncertainty associated with the near-field probe measurements is $\pm 10\%$, whereas the uncertainty associated with the far-field probe measurements is $\pm 0 - 50\%$ on the integrated beam current. The near-field data is presented first, followed by the far-field data.

As outlined in Section 4.2.2.1, the near-field ion current density contours reported here are formed from over 64,000 individual measurements [8], with subsequent comparisons of ion current density profiles having been extracted from this experimental data set. Figure 5.16 shows a comparison of these measurements to near-field ion current density calculations in MPIC3-simulation. Both MPIC3-simulation and the experimental data show the beam of ions in the near-field to be highly collimated over the first mean thruster diameter. Both MPIC3-simulation generally overpredicts the magnitude of ion current density relative to the measured data; however, relative to the measured data, it typically does not overpredict to the degree that

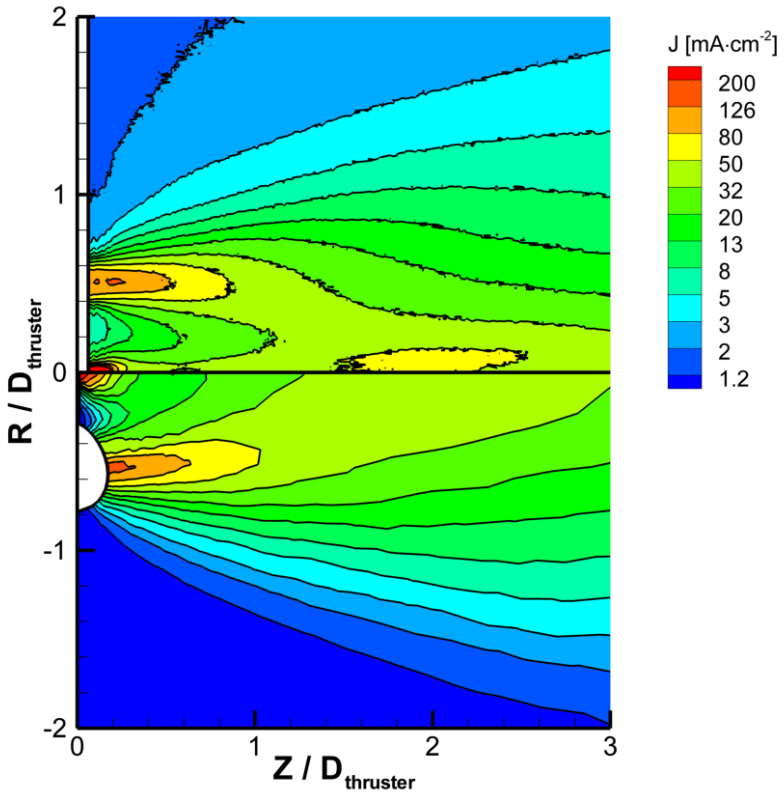

Figure 5.16: Comparison of ion current density between experimental measurements (top) and MPIC3-simulation (bottom).

MPIC2-simulation does. The measured peak ion current density for the main beam is 128 $\frac{mA}{cm^2}$ and occurs at $Z/D_{thruster} = 0.2$ and $R/D_{thruster} = 0.5$, whereas MPIC3-simulation calculates an ion current density of approximately 140 $\frac{mA}{cm^2}$ at the same location. This represents better agreement with the measured data than MPIC1- or MPIC2-simulation, which calculate ion current densities of approximately 159 $\frac{mA}{cm^2}$ and 145 $\frac{mA}{cm^2}$ at the same location. Although MPIC3-simulation calculates a higher peak ion current density than the measured peak, the discrepancy between the two is within experimental uncertainty.

Figures 5.17- 5.20 show ion current density profiles as calculated by MPIC1-, MPIC2-, and MPIC3-simulation compared to experimental data. The axial profiles in Figure 5.17 show qualitative agreement between the measured data and the

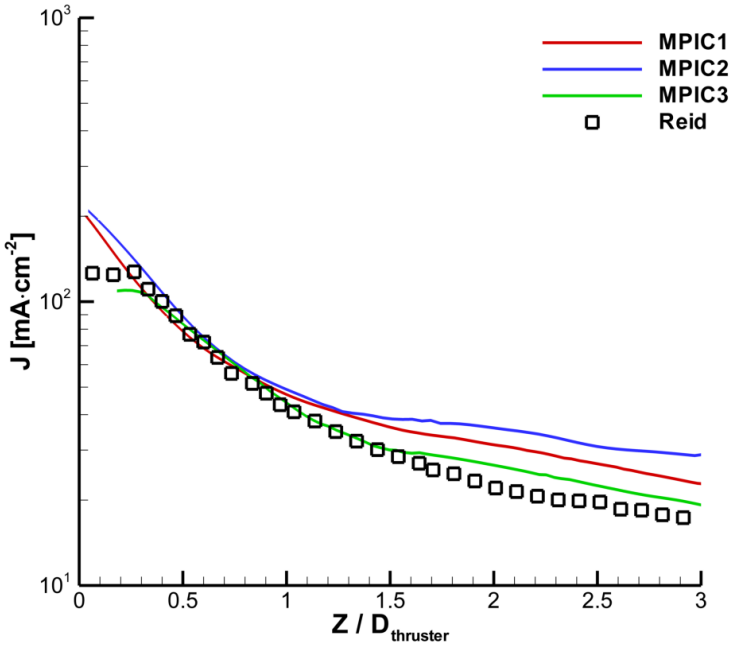

Figure 5.17: Comparison between MPIC1-, MPIC2-, MPIC3-simulation, and experimental measurements: axial ion current density variation along $R/D_{thruster} = 0.5$.

calculated ion current densities: for $Z/D_{thruster} > 0.3$, ion current density monotonically decreases. In general, MPIC3-simulation shows good agreement with measured data over a wider range than MPIC2-simulation: MPIC2-simulation shows good agreement with measured data between $Z/D_{thruster} = 0.5 - 1.2$, whereas MPIC3-simulation shows good agreement with measured data between $Z/D_{thruster} = 0.5 - 3$. Additionally, between $Z/D_{thruster} = 0.05 - 0.2$, measured data actually shows an increase in ion current density. Both MPIC1- and MPIC2-simulations calculate a decrease in ion current density due to the same limitations of the electron submodel discussed above, whereas MPIC3-simulation does calculate a small increase in ion current density in the same region due to the proposed inflow boundary. However, all simulations typically calculate profiles that are larger in magnitude than the profile of measured data, even after accounting for measurement uncertainty.

Figures 5.18- 5.20 show the behavior of radial profiles of ion current density as

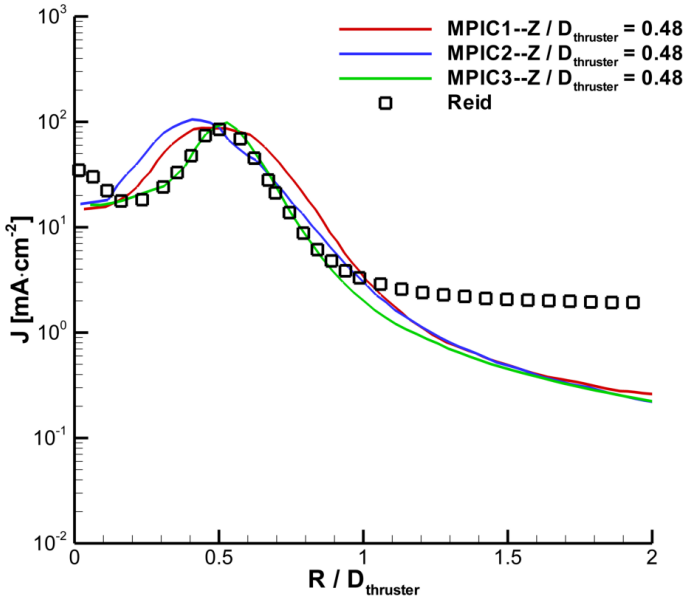

Figure 5.18: Comparison between MPIC1-, MPIC2-, MPIC3-simulation, and experimental measurements: radial ion current density variation along $Z/D_{thruster} = 0.48$.

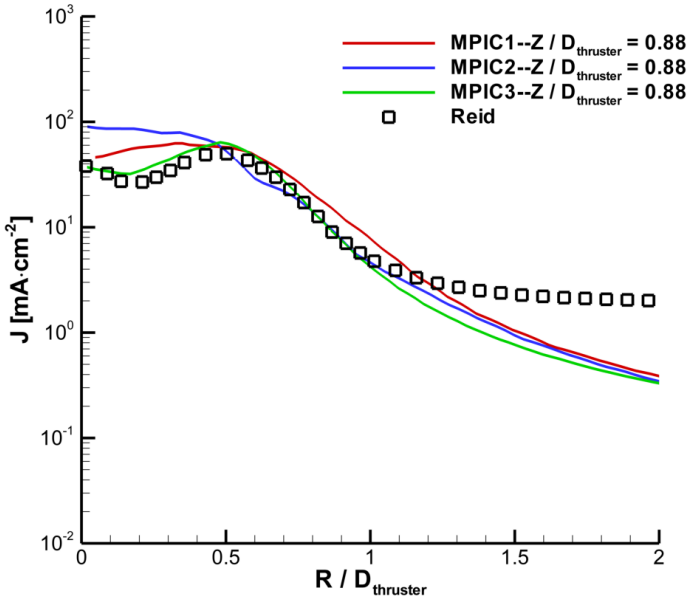

Figure 5.19: Comparison between MPIC1-, MPIC2-, MPIC3-simulation, and experimental measurements: radial ion current density variation along $Z/D_{thruster} = 0.88$.

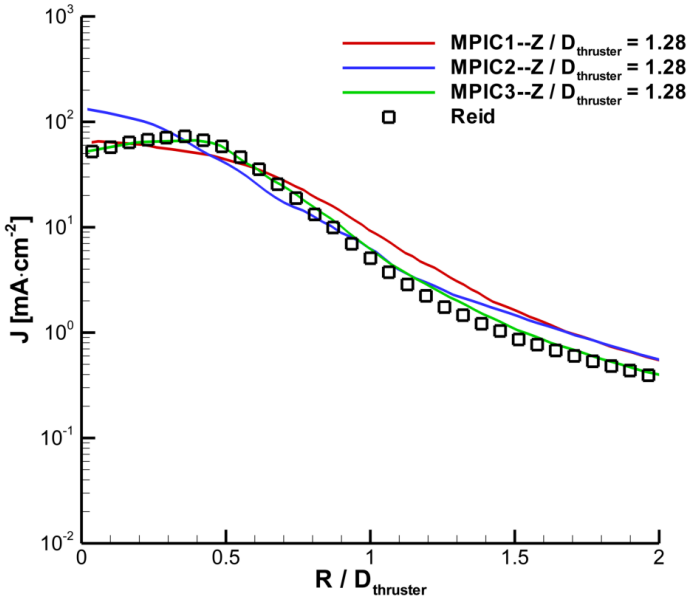

Figure 5.20: Comparison between MPIC1-, MPIC2-, MPIC3-simulation, and experimental measurements: radial ion current density variation along $Z/D_{thruster} = 1.28$.

$Z/D_{thruster}$ increases. These figures show excellent qualitative agreement between MPIC3-simulation and measurements. Although MPIC3-simulation underpredicts the centerline spike in ion current density by approximately 28% relative to the measured data, it calculates a coalescence of the centerline beam into the main ion beam that corresponds well with the coalescence exhibited in the measured data. Other qualitative features show good agreement between all simulations and the measured data: the measured magnitude of the main beam ion current density shows good agreement with MPIC1-, MPIC2- , and MPIC3-simulation results equally. Again, at far off-axis locations, the ion current density measurements at $Z/D_{thruster} = 0.48$ and $Z/D_{thruster} = 0.88$ exhibit a plateau at around 1.9 $\frac{mA}{cm^2}$.

Figure 5.21 shows comparisons of angularly resolved far-field ion current density. The measured data shown here were acquired with the far-field Faraday probe outlined in Section 1.1.2.4. Qualitative agreement between MPIC3-simulation and experiment is very good between 0°-90°, although at angles between 90°-150°, MPIC3-simulation

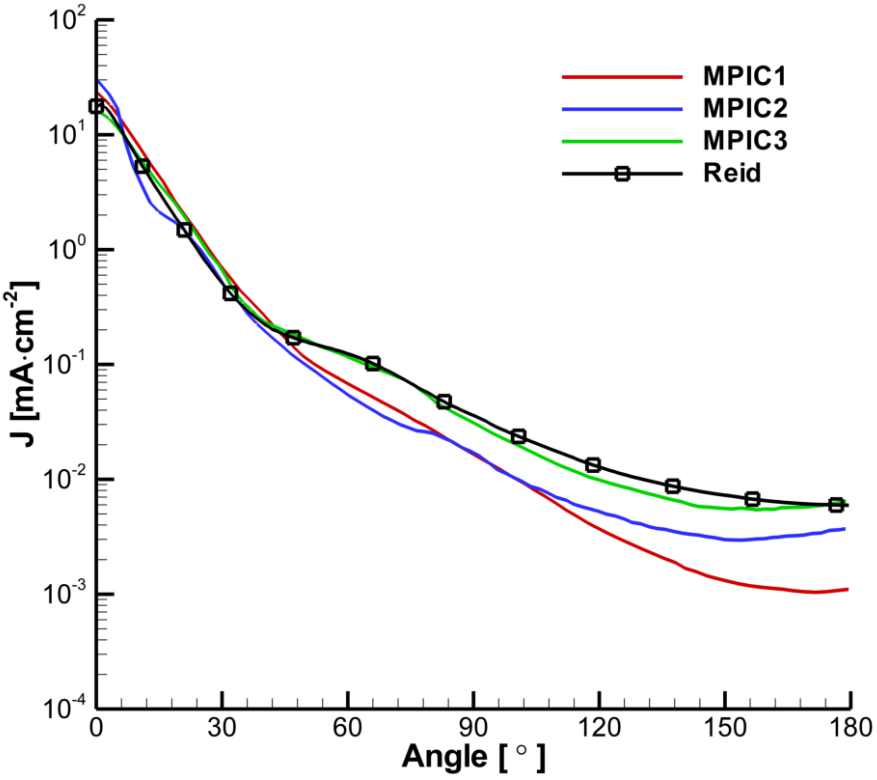

Figure 5.21: Comparison between MPIC1-, MPIC2-, MPIC3-simulation, and experimental measurements: angular variation of far-field ion current density along a 1 m circular arc.

underpredicts the measured data by 20-25%. The measurements show an inflection point near 30°, near the inflection point of 35° as calculated by MPIC3. The measurements show a second inflection point near 60°, near the inflection point of 70° as calculated by MPIC3. Between 150°-180°, the measurements show CEX wings, which agrees qualitatively with the simulated profiles. The measured decay rates in the low-angle and mid-angle regions show good agreement with the decay rates calculated by MPIC3, whereas the decay rate measured in high-angle region is lower than the calculated rates. This results in simulated data underpredicting ion current density between 90°-180°, relative to measured data. However, this shows marked improvement over MPIC2-simulation: relative to the measured data, MPIC2-simulation underpredicts ion current density approximately 52% at 150°, whereas MPIC3-simulation underpredicts measurements by approximately 22%.

The integrated ion beam currents based on the profiles in Figure 5.21 are as follows: integrating the MPIC1-, MPIC2-, and MPIC3-simulation profiles results in ion beam currents of approximately 18.0 A, 18.1 A, and 19.0 A, respectively; integrating experimental measurements results in an ion beam current of 21 A. The uncertainty associated with the integrated ion beam current ranges between $+0/-50\%$, which the calculated ion beam currents are both well within. Again, the total discharge current at the nominal operating condition is 20 A. Explanations for the differences between the total discharge current, measured integrated ion beam current, and simulated integrated ion beam current are suggested in Section 4.2.2.1.

5.3.2 Plasma Potential

Experimental measurements of plasma potential were performed by Jameson [11]. The plasma potential measurements were taken using the emissive probe outlined in Section 1.1.2.4 in an investigation window spanning $Z/D_{thruster} = 0.05 - 1.25$ and $R/D_{thruster} = 0 - 0.85$. The uncertainty associated with these measurements

is $+3/-1V$.

The near-field plasma potential contours reported here are formed from the measured data in Ref. [11], with subsequent comparisons of plasma potential profiles having been extracted from this experimental data set. Note that some measured values near the edge of the investigation window are removed from the experimental data set, though no reason is reported for doing so in Ref. [11]. Figure 5.22 shows a comparison of these measurements to near-field plasma potential calculations in MPIC3-simulation. MPIC3-simulation shows qualitative agreement with the measured data in the main ion beam: along a line of constant $\mathrm{R/D_{thruster}} = 0.5$, the calculated and measured voltage drop is similar. However, MPIC3-simulation does not show the same depression in plasma potential near the cathode as is exhibited in the experimental data. Further, outside the regions in the immediate vicinity of the TE plane and cathode, measured data shows a nearly constant field potential of around 23 V, whereas MPIC3-simulation typically calculates uniform gradients in plasma potential throughout the near-field.

Figures 5.23- 5.26 illustrate quantitative comparisons between the plume simulations and measured data. Figure 5.23 shows the axial variation of plasma potential along the thruster's acceleration channel CL. In the near-field, both MPIC1- and MPIC2-simulation calculate plasma potentials well above the measured data: between $\mathrm{Z/D_{thruster}} = 0 - 0.25$, calculated potential overpredicts the measured data by between 100-225%. However, MPIC3-simulation calculates a plasma potential profile that is on the same order of magnitude as the measured data. Further, MPIC3-simulation captures the same trends that MPIC1, MPIC2, and measured data exhibit: Figure 5.23 shows that for $\mathrm{Z/D_{thruster}} > 0.2$, plasma potential monotonically decreases with increasing $\mathrm{Z/D_{thruster}}$. Further, MPIC3-simulation calculates a plasma potential that varies over a dynamic range similar to that observed in the measured profile: the range of measured values of plasma potential is approximately 14 V,

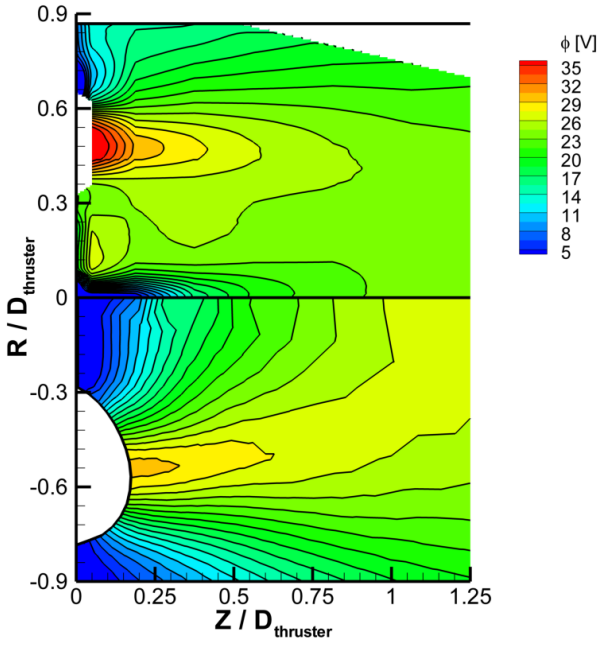

Figure 5.22: Comparison of plasma potential between experimental measurements (top) and MPIC3-simulation (bottom).

whereas the range of the MPIC3-simulation profile is approximately 15 V. Comparing the dynamic range of plasma potential between MPIC3-simulation and measured data is not entirely consistent since the domain for MPIC3 does not encompass regions of high magnitude potential. Assuming a conservative correction of approximately 10 V to account for this discrepancy, the dynamic range for plasma potential calculated by MPIC3 is approximately 25 V, which is still in better agreement with the measrements than MPIC1 or MPIC2 calculations.

Figures 5.24- 5.26 show the behavior of radial profiles of plasma potential as $Z/D_{thruster}$ increases. These figures show excellent qualitative agreement between MPIC3-simulation and measurements. Although MPIC3-simulation typically overpredicts the plasma potential by approximately 8-10% relative to the measured data, agreement between MPIC3 and the measured data is better than that between MPIC1 or MPIC2 and the measurements. Other qualitative features show good agree-

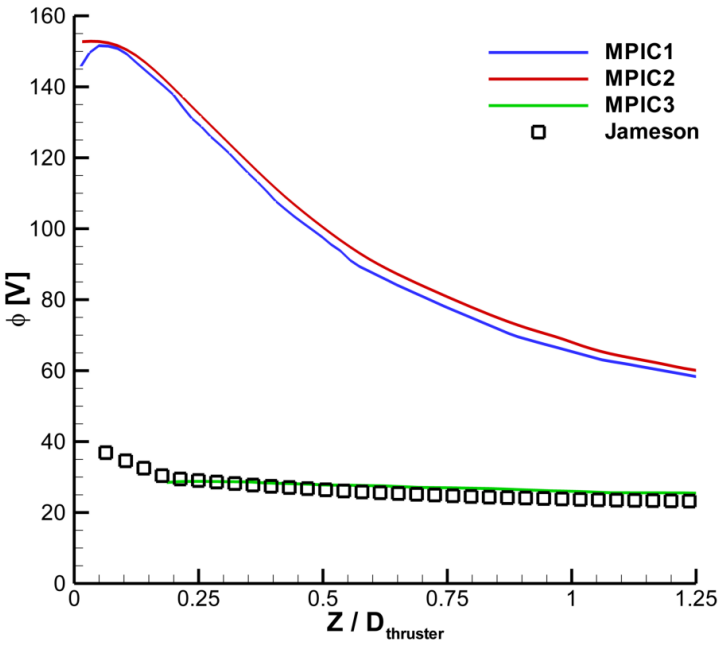

Figure 5.23: Comparison between MPIC1-, MPIC2-, MPIC3-simulation, and experimental measurements: axial plasma potential variation along $R/D_{thruster} = 0.5$.

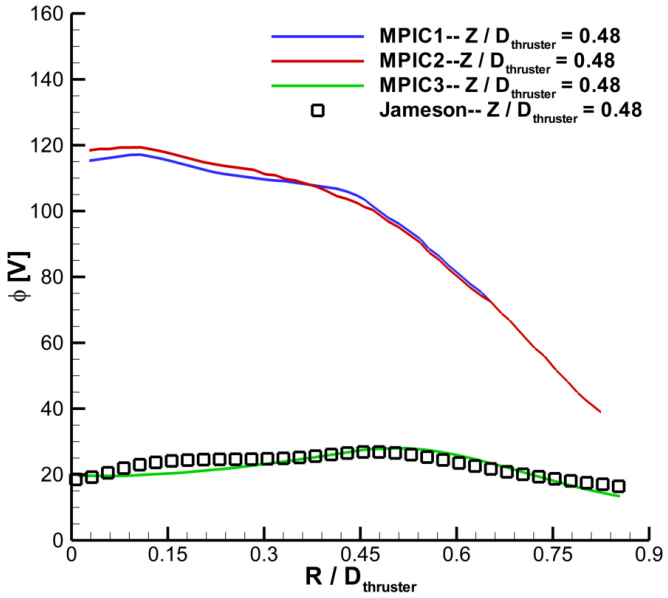

Figure 5.24: Comparison between MPIC1-, MPIC2-, MPIC3-simulation, and experimental measurements: radial plasma potential variation along $Z/D_{thruster} = 0.48$.

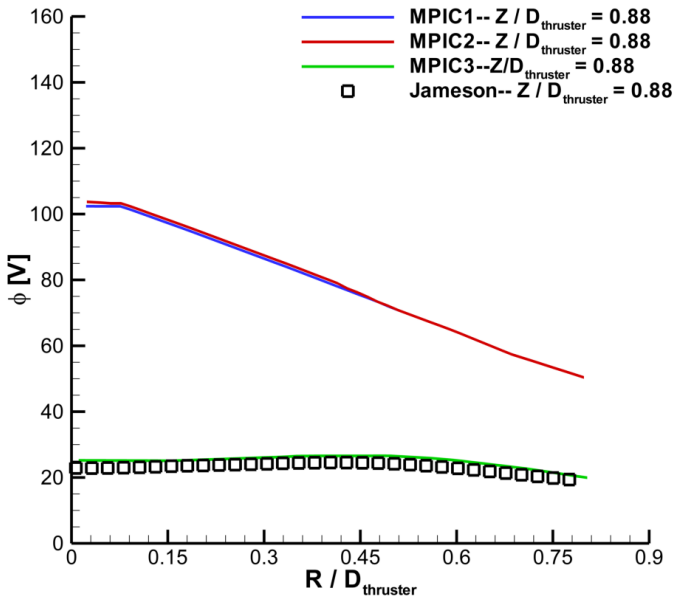

Figure 5.25: Comparison between MPIC1-, MPIC2-, MPIC3-simulation, and experimental measurements: radial plasma potential variation along $Z/D_{thruster} = 0.88$.

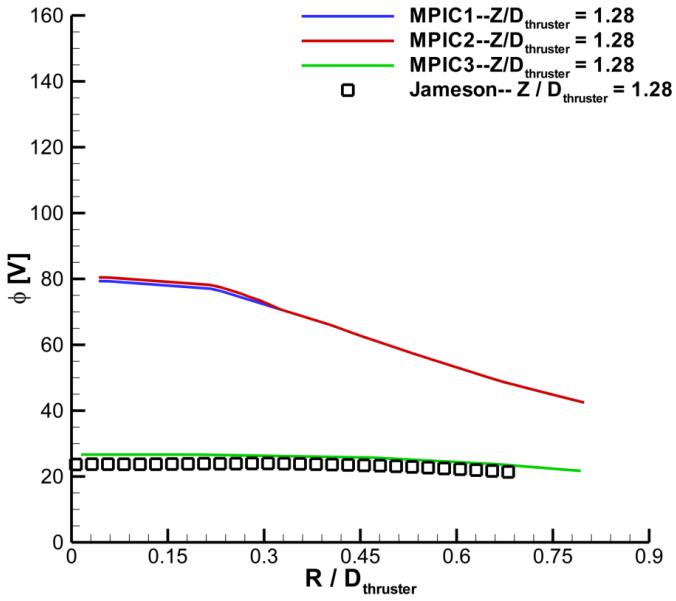

Figure 5.26: Comparison between MPIC1-, MPIC2-, MPIC3-simulation, and experimental measurements: radial plasma potential variation along $Z/D_{thruster} = 1.28$.

ment between MPIC3-simulation and the measured data: the measured profile at $Z/D_{thruster} = 0.48$ shows a small peak in plasma potential around $R/D_{thruster} = 0.45$, which corresponds to the peak calculated by MPIC3. As $Z/D_{thruster}$ increases, measurements show this peak gradually decreasing in magnitude to the background field potential. This trend also corresponds with MPIC3-simulation results.

5.3.3 Very Near-field Plume Comparisons

As outlined in Section 1.1.2.5, there are a variety of methods for modeling a Hall thruster plasma from the anode into the plume, including both hybrid models and uniform models (e.g. fully fluid and fully kinetic models). There are a number of current attempts to model a Hall thruster plasma from the anode into the plume using uniform models, using either fluid approaches [26, 27] or kinetic [29]. The plume simulations performed for the present study utilize inputs based on an internal thruster plasma simulation, resulting in a very loose coupling between the two computer codes. This section examines plasma properties in the very near-field plume in order to assess the efficacy of this coupling approach: as discussed in Section 1.1.2.5 and illustrated in Figures 5.1 and 5.2, the computational domains for HPHall and MPIC overlap , allowing direct comparison of plasma properties in the very near-field region.

In this section, H3-, MPIC1-, MPIC2-, and MPIC3-simulation calculations of ion current density and plasma potential are compared to experimental measurements. The ion current density measurements that are compared against were provided by PEPL, whereas the plasma potential comparisons were provided by JPL. Note that, with the exception of ion current density as calculated by H3, all of the results shown here have been presented previously: see Sections 3.2.2 and 5.3.

Figure 5.27 show axial ion current density profiles as calculated by H3-, MPIC1-, MPIC2-, and MPIC3-simulation compared to experimental data. The profiles in Fig-

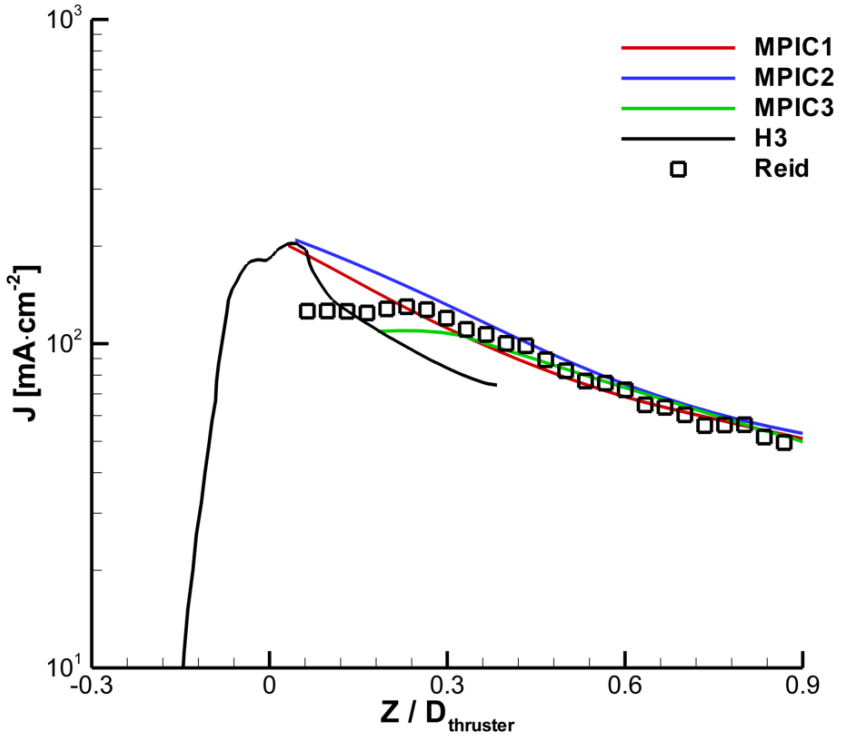

Figure 5.27: Comparison between H3, MPIC1-, MPIC2-, MPIC3-simulation, and experimental measurements: axial ion current density variation along $R/D_{thruster} = 0.5$ in the very near-field. Note that negative $Z/D_{thruster}$ corresponds to axial stations inside the thruster acceleration channel.

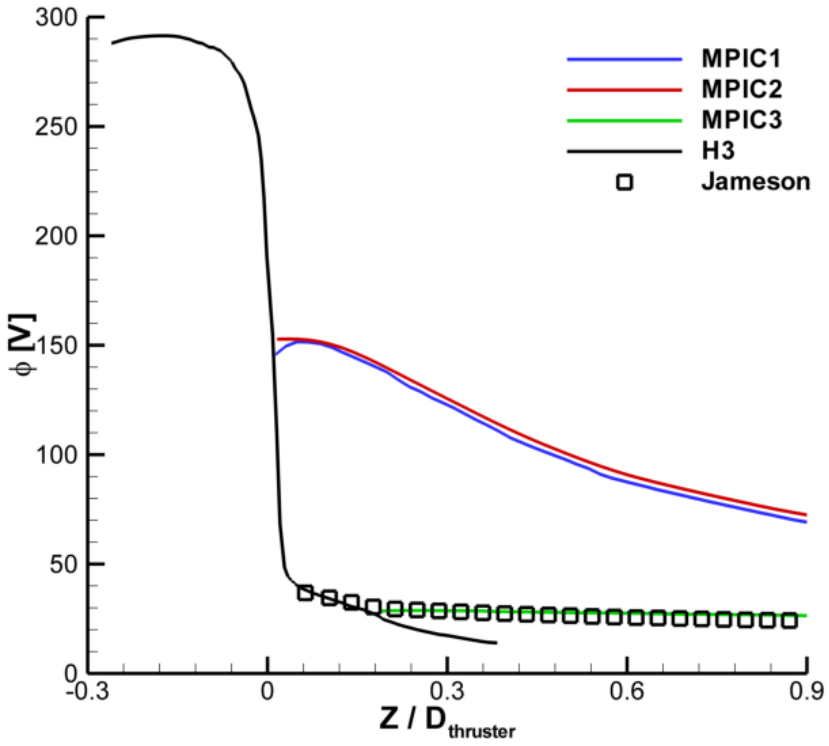

Figure 5.28: Comparison between H3-, MPIC1-, MPIC2-, MPIC3-simulation, and experimental measurements: axial plasma potential variation along $R/D_{thruster} = 0.5$. Note that negative $Z/D_{thruster}$ corresponds to axial stations inside the thruster acceleration channel.

ure 5.27 show good qualitative agreement between the measured data and the calculated ion current densities, as reported in Section 4.2.2.1; however, in the very near-field, approximately $Z/D_{thruster} = 0 - 0.4$, MPIC3-simulation shows better agreement with measured data than H3-simulation. MPIC3-simulation qualitatively agrees with the measured gradient of ion current density, whereas H3-simulation calculates a much larger gradient. One possible explanation for this is the electron fluid submodel that H3 uses: the model assumes the electron behavior is quasi-1D, an assumption that becomes less justifiable in the very near-field than in the acceleration channel itself. Since the plasma potential is calculated using the electron fluid submodel, it is possible that the gradient in plasma potential is overpredicted in the very near-field plume region, relative to the measured data. This would in turn overaccelerate ions, leading to a sharper decrease in ion current density than the decrease exhibited in the measured data.

Figure 5.28 show axial plasma potential profiles as calculated by H3-, MPIC1-, MPIC2-, and MPIC3-simulation compared to experimental data. The MPIC3-simulation profile shown in Figure 5.28 shows marked improvement over MPIC1- and MPIC2-simulation results regarding qualitative agreement with the measured data, as reported in Section 4.2.2.2. However, at $Z/D_{thruster} > 0.2$, MPIC3-simulation shows better agreement with measured data than H3-simulation, where H3-simulation overpredicts the gradient in plasma potential relative to the measured data. This seems to corroborate the explanation given above regarding the decrease in ion current density. As reported in Section 3.2.2, H3-simulation shows good qualitative agreement with measured data inside the thruster acceleration channel. However, the quasi-1D assumption is less justifiable as $Z/D_{thruster}$ increases into the plume. This leads to the observed overprediction in the gradient in plasma potential.

5.3.4 Discussion

Comparisons between MPIC3-simulation and measured data show excellent agreement regarding ion current density data, as well as moderate agreement with measured plasma potential data. In the near-field, the magnitude of MPIC3-simulation ion current density calculations shows better agreement with measured ion current density magnitudes than that of MPIC1- or MPIC2-simulation, particularly for the main ion beam. MPIC3-simulation also shows better agreement with measured data regarding the near-field evolution of the main ion beam than either MPIC1- or MPIC2-simulation. However, in all simulations the magnitude of the centerline spike in ion current density is underpredicted by 28-30%, relative to the measured data.

Comparisons of far-field ion current density show good agreement between MPIC3-simulation and measurements between 0°-90°, whereas at higher angles, MPIC3 underpredicts the measured data by around 22%, relative to the measured data. However, this underprediction represents significantly better agreement between high plume divergence angle ion current density measurements and simulated results than either MPIC1- or MPIC2-simulation.

Further, MPIC3-simulation shows good agreement with measured plasma potential data, whereas both MPIC1 and MPIC2 calculate plasma potential data that is incommensurate with measured data. The primary reason for the success of MPIC3 is due to the proposed computational domain. As shown in Chapter 4, ignoring magnetic field effects can significantly affect plasma potential calculations. However, since MPIC3 utilizes a domain that maps the inflow boundary to a region away from the regions of greatest magnetic field strength, magnetic field effects become much less significant. Thus, neglecting magnetic field effects has less impact on plasma potential calculation in MPIC3-simulation than in MPIC1 or MPIC2, resulting in significantly improved agreement between simulated and measured data for no additional compu-

tational cost.

Due to the physical models it utilizes, H3-simulation provides MPIC3-simulation with the inflow conditions and computational geometry to accurately resolve overall plume structure. However, the examination of the very near-field plume shows that, as $Z/D_{thruster}$ increases past 0.2, MPIC3-simulation agrees with measured data better than H3-simulation. This highlights the fact that accurate characterization of a Hall thruster plasma from the anode into the plume is difficult when using a single model. The discharge plasma within a Hall thruster is in a different flow-regime than the plasma in the plume, therefore different physical and computational models are appropriate for each region.

CHAPTER VI

Conclusions

The purpose of this chapter is threefold: first, to provide a summary of the work included in this thesis; second, to outline the original contributions of this work; third, to provide an outline of recommendations for future work in simulation of Hall thruster plumes.

6.1 Summary

The present study began with two objectives: first, to improve plume simulation accuracy by developing and examining a new collision dynamics model in MPIC; second, to improve plume simulation accuracy by coupling MPIC to an internal Hall thruster simulation code, HPHall. Chapter 1 provided important background information and motivation for the problem under consideration, namely characterizing Hall thruster plasma plumes. Different approaches to characterizing these plumes were considered, including elaboration of pertinent experimental and numerical methods. Specifically, a particle-fluid hybrid simulation method was shown to combine computational efficiency and accuracy benefits when compared to particle or fluid methods alone. Finally, the scope of the dissertation was set by its major objectives: development of a physical model and coupling two state-of-the-art hybrid method computer codes, HPHall and MPIC.

In Chapter 2, detailed information regarding the hybrid simulation method was outlined. Since each computer code that was utilized in the present work is a particle-fluid hybrid code, the two submodels that constitute each code were described. Both HPHall and MPIC utilize particle submodels in order to simulate the behavior of the heavy species in a plasma, with the primary difference between the two being two-fold: first, HPHall calculates unsteady plasma behavior, whereas MPIC assumes steady-state behavior. Second, although HPHall and MPIC both utilize fluid submodels in order to simulate the behavior of the electrons in a plasma, the differences between the two electron submodels are significant: HPHall implements a quasi-1D fluid model that includes magnetic field information in order to simulate electron behavior, whereas MPIC utilizes a conservation-law-style description of the electrons as a fluid that does not include magnetic field information. Finally, several numerical issues were discussed.

In Chapter 3, results from HPHall internal thruster simulations were presented in order to assess effects of two different post-collision scattering models, one based on an MCC model (H2), and one based on a DSMC model (H3). These results were subsequently compared to experimental data by examining internal plasma properties as well as velocimetry data. Finally, MPIC inlet boundary conditions were extracted from the internal plasma simulations for implementation into plume simulations, since plume simulations provide a further tool for assessing the accuracy of the two methods. Based on results in Sections 3.1 and 3.2, there were moderate differences between the simulations, and these differences were traced back to the heavy species submodels they utilize. Due to the DSMC algorithm that constitutes the heavy species submodel in H3, H3 calculates velocimetry and plasma properties that agree with measurements more closely than the H2 counterparts. Utilizing DMSC collision modeling results in VDF calculations for neutral xenon that resolve the high velocity tail that is seen in LIF measurements, a VDF feature that is absent in MCC

calculations. This difference in collision modeling has a traceable effect on various plasma properties that generally improved agreement between simulations and measured data. Typically, H3 calculations were found to agree with measured data more closely than H2 calculations.

In Chapter 4, plume simulation boundary conditions were detailed. Baseline MPIC results that utilized the inflow conditions calculated by H2- and H3-simulations were presented and compared to experimental data taken in order to assess viability of the two different internal plasma models. Comparisons between H2- and H3-simulation and measured data showed moderate to good agreement regarding ion current density, but poor agreement regarding plasma potential. Based on H3-simulation's better agreement with measurements, both internal to the thruster and in the near-field plume, subsequent plume simulations relied exclusively on H3 calculated results. Results from MPIC simulations were compared in order to characterize the differences between two post-collision scattering angle models, one based on a combination of isotropic and analytic scattering distributions (MPIC1), and the other based on empirical scattering distributions (MPIC2). The differences between these two models are found in Table 2.1. These plume simulations were subsequently compared to experimental data in order to assess the accuracy of the two models. These comparisons were made by examining heavy species properties in the near- and far-field. The comparisons illustrated moderate to good agreement with measured ion current density data. For the majority of the near-field plume, simulations utilizing the empirical scattering distributions showed better agreement with measurements than simulations utilizing isotropic and analytic distributions. Furthermore, simulations utilizing the empirical scattering angle distributions captured distinct trends in the far-field ion current density data, trends that are not resolved in simulations utilizing the isotropic and analytic distributions. Finally, the empirical scattering model showed better agreement with ion current density measurements at

high plume divergence angles than the previous model. Based on the empirical scattering model's better agreement with measurements in these cases, the post-collision scattering model which MPIC2 utilizes more accurately characterizes the structure of the plume, especially at high divergence angles.

In Chapter 5, plume simulation boundary conditions were detailed, with discussion centered on the re-mapping of inflow boundaries. MPIC results that utilized the empirical scattering model and the newly mapped inlet were presented and compared to the MPIC results calculated using the empirical scattering model and the previous computational domain. Simulations that utilized the empirical scattering model and the new domain (MPIC3) calculated results that were qualitatively different from simulations that used the same scattering model and the previous domain, with the primary differences between the two simulations being the initial plume divergence and the plasma potential magnitude at the inflow boundary. In comparing these results to experimental data, MPIC3-simulation showed excellent agreement with measured data regarding ion current density, as well as greatly improved agreement with measured plasma potential data. In the near-field, the magnitude of MPIC3-simulation ion current density calculations showed better agreement with measured ion current density magnitudes than that of either simulation using the previous computational domain (MPIC1 and MPIC2), particularly for the main ion beam. MPIC3-simulation also showed better agreement with measured data regarding the near-field evolution of the main ion beam than either MPIC1- or MPIC2-simulation. Comparisons of far-field ion current density showed good agreement between MPIC3-simulation and measurements between 0°-90°, whereas at higher angles, MPIC3 underpredicted the measured data by around 22%, relative to the measured data. However, this underprediction represented better agreement between high plume divergence angle ion current density measurements and simulated results than either MPIC1- or MPIC2-simulation. MPIC3-simulation showed good agreement with measured plasma poten-

tial data, whereas both MPIC1 and MPIC2 calculated plasma potential data that was incommensurate with measured data. The primary reason for the success of MPIC3 was due to the proposed computational domain: since the effect of the magnetic field is much smaller at the re-mapped inflow boundary, ignoring the magnetic field in MPIC is more justifiable in the new domain. Finally, comparisons were made between calculated and measured plasma properties in the very near-field plume region. In these comparisons, MPIC3 shows better agreement with very near-field measurements than H3, illustrating the need for utilizing different models for different regions of the Hall thruster plasma.

6.2 Contributions

As outlined in Section 1.1.2.6, the present work represents several contributions to the field of Hall thruster plasma modeling.

1. Verification of an updated model for internal thruster simulation. Currently there are no published reports verifying the HPHall3 computer code. The present work represents a step in the validation process by comparing results between HPHall3 and HPHall2, where HPHall2 has been extensively assessed (see Section 1.1.2.5). The present work also shows H3 results agree with experimental measurements: H3 agrees with measured plasma properties to the same degree that H2 does, and H3 shows better agreement with velocimetry data than H2.

2. Implementation of a new collision dynamics model in a full-scale plume simulation. The collision model utilized in MPIC2 (see Section 2.2.4.2) is based on experimental measurements that characterize previously unknown aspects of collision modeling. Specifically, the present work implements a model for computing the post-collision scattering angle based on an empirical curve fit,

where previous models assume scattering to be either isotropic or follow an analytic distribution. The model implemented here has been tested previously on a simple computational domain [40], but the present work shows the first implementation in a full-scale plume simulation.

3. Coupling state-of-the-art Hall thruster plasma simulation codes. Recent studies that coupled Hall thruster internal plasma simulations codes to plume simulation codes relied on a variety of models. One approach coupled a hydrodynamic model for the internal plasma to a hybrid PIC-fluid model for the plasma plume [23]; another coupled a previous version of HPHall to a PIC model for the plasma plume [34]. However, the present work represents the first implementation in which a hybrid model for the internal plasma has been coupled to a hybrid PIC-fluid model for the plasma plume. Further, the procedure in which separate codes for the internal plasma and the plasma plume are coupled was validated at the end of Chapter 5: comparisons between plasma properties in the very near-field plume show the necessity for using different computational models for different regions of the Hall thruster plasma.

6.3 Recommendations for Future Work

The main objective of the present work was to improve the accuracy of Hall thruster plume simulation. To that end, several key areas were identified that can potentially improve simulation accuracy significantly.

6.3.1 Electron Mobility Modeling

Electron mobility modeling has been identified as a key area of future study for HPHall and similar computer codes [20, 77]. Typically, cross-field electron mobility is calculated as a function of electron collision frequency that includes a contribution

from anomalous Bohm diffusion. This contribution due to anomalous diffusion is adjustable such that the total collision frequency matches experimentally measured frequencies. The anomalous diffusion component typically varies over two or three regions of the simulation domain. Electron mobility has a significant influence on simulated results, but is not well-understood [70, 77]. Therefore, electron mobility modeling can improve HPHall-simulated results in two ways. First, the current numerical approach can be improved by increasing the number of regions over which the adjustable contribution to collision frequency varies. Ref. [20] suggests that current electron mobility models can be refined by increasing the number of regions that are fit to experimental data. Second, the current numerical approach can be improved by better understanding the fundamental processes involved in cross-field electron mobility [77].

6.3.2 Additional Thruster Operating Conditions

The present study focused on simulating the plume of a 6 kW Hall thruster at the nominal operating condition. However, using data from other operating conditions, further comparisons can be made to assess both the internal thruster simulation and the plume simulation. Refs. [9, 10] report measurements made at off-nominal conditions which can be used to verify the new model in HPHall, whereas Ref. [8] reports further experimental data pertaining to the plume that is available for off-nominal operating conditions. Ref. [8] also reports HPHall2 simulations that have been performed for additional operating conditions that span a range of discharge voltages and mass flow rates.

6.3.3 Cathode Modeling

The current plume model makes strong assumptions about the makeup of the cathode mass flow. Currently, the only heavy particles injected at the cathode are

xenon neutrals. This assumption is made for two reasons. First, it allows for a clear calculation of boundary conditions for the fluid electron model, as injecting xenon ions from the cathode creates a current density which feeds back into determination of the fluid boundary conditions. Second, the assumption is made because there is no data available on the ion properties at the cathode outside of current density measurements. However, on comparing the computational predicted current density at the cathode with the measured current density, it is clear that the cathode flow also contains some xenon ions, as the measured current density is nearly twice that of the predicted current density. Further, previous work on cathode modeling also indicates the presence of xenon ions [76]. Therefore, it is suggested that the cathode boundary conditions be examined further, in order to more closely model the mass flow of the cathode.

6.3.4 Non-equilibrium Particle Injection

The current plume model injects computational particles at velocities determined by Maxwellian VDF's, as outlined in Section 2.2.3.1. Therefore, macroparticle injection for each species in plume simulations is currently determined by the bulk velocity, number density, and temperature that are extracted from HPHall. However, as shown in Section 3.1.2.1, the VDF's extracted from HPHall are, in fact, non-Maxwellian. Thus, the bulk properties extracted from HPHall are based on a non-equilibrium flow and are not well-defined when applied to a Maxwellian VDF. Since inflow conditions have a significant impact on the calculated plume structure, it is suggested that implementation of non-equilibrium inflow conditions be examined for this application.

6.3.5 Plasma Transport Properties

The current plume model requires calculation of plasma transport properties in order to solve the conservation law-style fluid model, including the electrical conductivity of the plasma as shown in Eqn. (2.29). However, recent work in aerodynamic control via plasma actuation has detailed the use of a Boltzmann style solver that calculates electrical conductivity using Eqn. (2.29) in conjunction with electron mobility models that affect the calculation of ν_e [78]. Application of the solver to the current problem would provide an improved level of accuracy for conductivity calculations, which could in turn improve the level of accuracy of the electron submodel.

APPENDICES

APPENDIX A

Nomenclature

Symbol	Description
A	Area
$\vec{B}$	Magnetic field vector
$\vec{c}$	Particle velocity vector
c_e	Mean electron thermal velocity
C_i	Ionization rate
d	Atomic diameter
e	Elementary charge
$\vec{E}$	Electric field vector
$f(c)$	Velocity distribution function
$\vec{F}$	General force vector
g	Relative velocity magnitude
$\vec{g}$	Relative velocity vector
g_o	Gravitational constant
I_{sp}	Specific impulse
$\vec{j}$	Current density vector
k	Boltzmann constant

L	Characteristic length
m	Atomic mass, or mean mass of exhaust products
m_c	Reduced mass
$\dot{m}$	Mass flow rate
M	Matrix
M_i, M_n	Macroparticle weight
n	Number density
N	Number of macroparticles per cell
$\overline{N}$	Average number of macroparticles per cell
p	Pressure
P	General probability
$P(x, y, z)$	Generalized Poisson equation variable
q	Heat flux
$Q(x, y, z)$	Generalized Poisson equation coefficients
R	Random number, gas constant
$\vec{R_o}$	Non-electromagnetic force vector
$S(x, y, z)$	Generalized Poisson equation source terms
Δt	Simulation timestep
T	Temperature
U, V, W	Mean velocity
V	Volume
$\vec{v}$	Velocity vector

Greek

α_{Dugan}	Dugan ionization cost factor
ϵ_i	Ionization energy for xenon, 12.7 eV
ϵ_o	Permittivity of free space
κ	Thermal conductivity

λ	Mean free path
$\mu_{e,\perp}$	Effective electron mobility parameter
ν	Wall accommodation coefficient
$\nu_e, \nu_{ei}, \nu_{en}$	Collision frequency
ω	Viscosity temperature exponent
ω_p	Plasma frequency
ϕ	Plasma potential
ψ	Electron velocity streamfunction
σ	Plasma conductivity
$\sigma_r, \sigma_{CEXorMEX}$	Collision cross section
θ	Post-collision scattering angle
ζ	General rate parameter

Subscripts and Superscripts

$+$, $2+$	Degree of ionization, single-charged and double-charged
cell	Cell-based
CEX	Charge-exchange
d	Discharge
e	Electron, exit
f	Final
i	Ion
MEX	Momentum-exchange
n	Neutral
$\hat{n}$	Normal direction
o	Initial value
r	Reference value

BIBLIOGRAPHY

BIBLIOGRAPHY

[1] Koppel, C. and Estublier, D., "The Smart-1 Hall Effect Thruster around the Moon: In Flight Experience," *29th International Electric Propulsion Conference*, 2005, IEPC-2005-119.

[2] Brophy, J., Marcucci, M., Ganapathi, G., and Gates, C., "Implementation of the Dawn Ion Propulsion System," *41st AIAA/ASME/SAE/ASEE Joint Propulsion Conference*, 2005, AIAA-2005-4071.

[3] Jahn, R. G., *Physics of Electric Propulsion*, McGraw-Hill, New York, 1968.

[4] Wilbur, P. J., "Electric Propulsion," *AccessScience, McGraw-Hill Companies*, 2002, http://www.accessscience.com.

[5] Peterson, T. T. and Curran, F. M., "Pulsed Plasma Thruster Technology Development and Flight Demonstration Program," Tech. rep., NASA Glenn Research and Technology Reports, 1998, http://www.grc.nasa.gov/WWW/RT/RT1997/6000/6910curran.htm.

[6] Zhurin, V. V., Kaufman, H. R., and Robinson, R. S., "Physics of Closed Drift Thrusters," *Plasma Sources Science and Technology*, Vol. 8, No. 1, 1999, pp. R1–R20.

[7] Choueiri, E. Y., "Fundamental Difference Between the Two Hall Thruster Variants," *Physics of Plasma*, Vol. 8, No. 11, 2001, pp. 5025–5033.

[8] Reid, B., *The Influence of Neutral Flow Rate in the Operation of Hall Thrusters*, Ph.D. Thesis, Dept. of Aerospace Engineering, University of Michigan, Ann Arbor, 2009.

[9] Huang, W., Gallimore, A., and Hofer, R., "Neutral Flow Evolution in a 6 kW Hall Thruster," *Journal of Propulsion and Power*, Vol. 27, No. 3, 2011, pp. 553–563.

[10] Huang, W., Gallimore, A., and Smith, T., "Two-Axis Laser-Induced Flouresscence of Singly-Charged Xenon inside a 6 kW Hall Thruster," *49th AIAA Aerospace Sciences Meeting*, 2011, AIAA-2011-1015.

[11] Jameson, K., *Investigation of Cathode Effects on Total Thruster Efficiency in a 6 kW Hall Thruster*, Ph.D. Thesis, Dept. of Aerospace Engineering, University of California, Los Angeles, Los Angeles, 2008.

[12] Linnell, J., *An Evaluation of Krypton Propellant in Hall Thrusters*, Ph.D. Thesis, Dept. of Aerospace Engineering, University of Michigan, Ann Arbor, 2007.

[13] Hargus, W. and Cappelli, M., "Interior and Exterior Laser-Induced Flourescence and Plasma Measurements with a Hall Thruster," *Journal of Propulsion and Power*, Vol. 18, No. 1, 2002, pp. 159–168.

[14] Haas, J., *Low-Perturbation Interrogation of the Plasma Structure of a Hall Thruster Using a High-Speed Probe Positioning System*, Ph.D. Thesis, Dept. of Aerospace Engineering, University of Michigan, Ann Arbor, 2001.

[15] Milne-Thomson, L., *Theoretical Aerodynamics*, D. Van Nostrand Co., 1947.

[16] Ahedo, E., Maqueda, A. A., Raitses, Y., and Fisch, N., "Numerical Simulation of a 2 kW Hall Thruster," *42nd AIAA/ASME/SAE/ASEE Joint Propulsion Conference*, 2006, AIAA-2006-4655.

[17] Fernandez, E., Cappelli, M., and Mahesh, K., "2D simulations of Hall thrusters," Ctr annual research briefs, 1998.

[18] Hagelaar, G. J. M., Bareilles, J., and Garrigues, L. B. J. P., "Two-dimensional model of a stationary plasma thruster," *Journal of Applied Physics*, Vol. 91, No. 9, 2002, pp. 5592–5598.

[19] Koo, J. W. and Boyd, I. D., "Computational Model of a Hall Thruster," *Physics Communications*, Vol. 164, No. 1-3, 2004, pp. 442–447.

[20] Giuliano, P. and Boyd, I., "Spectral analysis of simulated Hall thruster discharge current oscillations," IEPC Paper 2009-084, Sep 2009.

[21] Parra, F., Ahedo, E., Fife, J., and Martinez-Sanchez, M., "A two-dimensional hybrid model of the Hall thruster discharge," *Journal of Applied Physics*, Vol. 100, No. 023304, 2006.

[22] Cai, C., *Theoretical And Numerical Studies of Plume Flows in Vacuum Chambers*, Ph.D. Thesis, Dept. of Aerospace Engineering, University of Michigan, Ann Arbor, 2005.

[23] Choi, Y., *Modeling an Anode Layer Hall Thruster and Its Plume*, Ph.D. Thesis, Dept. of Aerospace Engineering, University of Michigan, Ann Arbor, 2008.

[24] Boerner, J., *Computational Simulation of Faraday Probe Measurements*, Ph.D. Thesis, Dept. of Aerospace Engineering, University of Michigan, Ann Arbor, 2008.

[25] Huismann, T. and Boyd, I., "Modeling of Virtual Diagnostics for Hall Thruster Plumes in a Vacuum-chamber," IEPC Paper 2009-089, Sep 2009.

[26] Mikellides, I., Katz, I., Hofer, R., and Goebel, D., "Hall-Effect Thruster Simulations with 2-D Electron Transport and Hydrodynamic Ions," IEPC paper 2009-114, September 2009.

[27] Mikellides, I., Katz, I., Hofer, R., Goebel, D., de Grys, K., and Mathers, A., "Magnetic shielding of the channel walls in a Hall plasma accelerator," *Physics of Plasmas*, Vol. 18, No. 3, 2011, pp. 033501–1–033501–18.

[28] Taccogna, F., Longo, S., and Capitelli, M., "Very-Near-Field Plume Simulation of a Stationary Plasma Thruster," *The European Physical Journal Applied Physics*, Vol. 28, No. 1, 2004, pp. 113–122.

[29] Taccogna, F., Schneider, R., Longo, S., and Capitelli, M., "Kinetic Simulations of a Plasma Thruster," *Plasma Sources Science and Technology*, Vol. 17, No. 024003, 2008.

[30] Boyd, I., "Review of Hall Thruster Plume Modeling," *Journal of Spacecraft and Rockets*, Vol. 38, 2001, pp. 381–387.

[31] Boyd, I., Garrigues, L., Koo, J., and Keidar, M., "Progress in Development of a Combined Device/Plume Model for Hall Thrusters," *36th AIAA/ASME/SAE/ASEE Joint Propulsion Conference*, 2000, AIAA-00-3520.

[32] Boyd, I. and Dressler, R., "Far field modeling of the plasma plume of a Hall thruster," *Journal of Applied Physics*, Vol. 92, No. 4, 2002, pp. 1764–1774.

[33] Cheng, S. and Martinez-Sanchez, M., "Comparison of Numerical Simulation to Hall Thruster Plume Shield Experiment," *40th AIAA/ASME/SAE/ASEE Joint Propulsion Conference*, 2004, pp. AIAA–2004–3635.

[34] Niemela, C., Brieda, L., Nakles, M., Ekholm, J., and Hargus, W., "Comparison of Hall Thruster Plume Expansion Model with Experimental Data," *42nd AIAA/ASME/SAE/ASEE Joint Propulsion Conference*, 2006, AIAA-2006-4480.

[35] Boyd, I., "Numerical Simulation of Hall Thruster Plasma Plumes in Space," *Plasma Science, IEEE Transactions on*, Vol. 34, No. 5, oct. 2006, pp. 2140 – 2147.

[36] Huismann, T. and Boyd, I., "Advanced Hybrid Modeling of Hall Thruster Plumes," *46th AIAA/ASME/SAE/ASEE Joint Propulsion Conference*, 2010, AIAA 2010-6525.

[37] Fife, J. M., *Hybrid-PIC Modeling and Electrostatic Probe Survey of Hall Thrusters*, Ph.D. Thesis, Department of Aeronautics and Astronautics, Massachusetts Institute of Technology, Cambridge, MA, 1998.

[38] Boeuf, J. P. and Garrigues, L., "Low Frequency Oscillations In a Stationary Plasma Thruster," *Journal of Applied Physics*, Vol. 84, No. 7, 1998, pp. 3541–3544.

[39] Azziz, Y., *Experimental and Theoretical Characterization of a Hall Thruster Plume*, Ph.D. Thesis, Department of Aeronautics and Astronautics, Massachusetts Institute of Technology, Cambridge, MA, 2007.

[40] Scharfe, M., Koo, J., and Azarnia, G., "DSMC Implementation of Experimentally-Based Xe-Xe+ Differential Cross Sections for Electric Propulsion Modeling," *Proceedings of the 27th International Symposium on Rarefied Gas Dynamics, Asilomar, CA*, Vol. 1333, 2010, pp. 1085–1090.

[41] Huismann, T. and Boyd, I., "Simulation of Hall Thruster Plumes in a Vacuum Chamber Using a Hybrid Method," *44th AIAA/ASME/SAE/ASEE Joint Propulsion Conference*, 2008, AIAA-2008-5103.

[42] Bird, G. A., *Molecular Gas Dynamics and the Direct Simulation of Gas Flows*, Oxford University Press, New York, 1994.

[43] Birdsall, C. K. and Langdon, A. B., *Plasma Physics Via Computer Simulation*, Adam Hilger, 1991.

[44] Roy, R. S., *Numerical Simulation of Ion Thruster Plume Backflow for Spacecraft Contamination Assessment*, Ph.D. Thesis, Massachusetts Institute of Technology, 1995.

[45] Roy, R. S., Hastings, D. E., and Taylor, S., "Three-Dimensional Plasma Particle-In-Cell Calculations of Ion Thruster Backflow Contamination," *Jorunal of Computational Physics*, Vol. 128, No. 1, 1996, pp. 6–18.

[46] Szabo Jr., J. J., *Fully Kinetic Modeling of a Hall Thruster*, Ph.D. Thesis, Department of Aeronautics and Astronautics, Massachusetts Institute of Technology, Cambridge, MA, 2001.

[47] Pullins, S. H., Chiu, Y., Levandier, D. J., and Dresseler, R. A., "Ion dynamics in Hall effect and ion thrusters - Xe(+) + Xe symmetric charge transfer," AIAA Paper 2000-0636, January 2000.

[48] Miller, S., Levandier, D. J., Chiu, Y., and Dresseler, R. A., "Xenon Charge Exchange Cross Sections for Electrostatic Thruster Models," *Journal of Applied Physics*, Vol. 19, No. 3, 2002, pp. 984–991.

[49] Bird, G. A., "Approach to translational equilbrium in a rigid sphere gas," *Physics of Fluids*, Vol. 6, No. 10, 1963, pp. 1518–1519.

[50] Bird, G. A., "Monte-Carlo Simulation in an Engineering Context," *Proceedings of the 12th International Symposium on Rarefied Gas Dynamics, Charlottesville, Virginia*, edited by S. S. Fisher, 1981, pp. 239–255.

[51] Bird, G. A., "Forty Years of DSMC," *Rarefied Gas Dynamics: 22nd International Symposium*, edited by T. J. Bartel and M. A. Gallis, 2001, pp. 372–380.

[52] Muntz, E. P., "Rarefied Gas Dynamics," *Annual Review of Fluid Mechanics*, Vol. 21, 1989, pp. 387–417.

[53] Oran, E. S., Oh, C. K., and Cybyk, B. Z., "Direct Simulation Monte Carlo: Recent Advances and Applications," *Annual Review of Fluid Mechanics*, Vol. 30, 1998, pp. 403–441.

[54] Ivanov, M. S. and Gimelshein, S. F., "Computational Hypersonic Rarefied Flows," *Annual Review of Fluid Mechanics*, Vol. 30, 1998, pp. 469–505.

[55] Bird, G. A., "Direct Simulation and the Boltzmann Equation," *Physics of Fluids*, Vol. 13, No. 11, Nov 1970, pp. 2676–2681.

[56] Mitchner, M. and Kruger, C. H., *Partially Ionized Gases*, Wiley, 1973.

[57] Oh, D. Y., Hastings, D. E., Marrese, C. M., Haas, J. M., and Gallimore, A. D., "Modeling of Stationary Plasma Thruster-100 Thruster Plumes and Implications for Satellite Design," *Journal of Propulsion and Power*, Vol. 15, No. 2, 1999, pp. 345–357.

[58] Domonkos, M. T., Marrese, C. M., Haas, J. M., and Gallimore, A. D., "Very Near-Field Plume Investigations of the D55," AIAA Paper 1997-3062, July 1997.

[59] Boyd, I. D. and Yim, J. T., "Modeling of the Near Field Plume of a Hall Thruster," *Journal of Applied Physics*, Vol. 95, No. 9, 2004, pp. 4575–4584.

[60] Ahedo, E., Martínez-Cerezo, P., and Martínez-Sánchez, M., "One-dimensional Model of the Plasma Flow in a Hall Thruster," *Physics of Plasmas*, Vol. 8, No. 6, 2001, pp. 3058–3068.

[61] Cohen-Zur, A. and Fruchtman, A., "Plume Divergence in the Hall Thruster Due to Pressure," IEPC Paper 2007-234, Sep 2007.

[62] Vichnevetsky, R., *Computer Methods for Partial Differenctial Equations*, Prentice-Hall, 1981.

[63] Press, W. H., Vetterling, S. A., Flannery, W. T., and Flannery, B. P., *Numerical Recipes in C*, Cambridge University Press, New York, 1994.

[64] Price, H. S., Varga, R. S., and Fitzgerald, R. M., "Recent numerical experiments comparing successive overrelaxation iterative methods with implicit alternative direction iterative methods," *Proceedings of the 1961 16th ACM national meeting*, ACM '61, ACM, New York, NY, USA, 1961, pp. 21.201–21.204.

[65] Peaceman, D. W. and Rachford Jr., H. H., "The numerical solution of parabolic and elliptic differential equations," *Journal of the Society for Industrial and Applied Mathematics*, Vol. 3, No. 1, 1955, pp. 28–41.

[66] Chen, J., Wang, Z., and Chen, Y., "Higher-order alternative direction implicit FDTD method," *Electronics Letters*, Vol. 38, No. 22, 2002, pp. 1321–1322.

[67] Hammel, J. R., *Development of An Unstructured 3-D Direct Simulation Monte Carlo/Particle-In-Cell Code and the Simulation of Microthruster Flows*, M. S. Dissertation, Mechanical Engineering Department, Worcester Polytechnic Institute, Worcester, MA, 2002.

[68] Ruyten, W. M., "Density-Conserving Shape Factors for Particle Simulations in Cylindrical and Spherical Coordinates," *Journal of Computational Physics*, Vol. 105, No. 2, 1993, pp. 224–232.

[69] Mazouffre, S., Echegut, P., and Dudeck, M., "A Calibrated Infrared Imaging Study on the Steady State Thermal Behaviour of Hall Effect Thrusters," *Plasma Sources Science and Technology*, Vol. 16, 2007, pp. 13–22.

[70] Cheng, S. Y.-M., *Modeling of Hall thruster lifetime and erosion mechanisms*, Ph.D. Thesis, Department of Aeronautics and Astronautics, Massachusetts Institute of Technology, Cambridge, MA, 2007.

[71] Lobbia, R., *A Time-resolved Investigation of the Hall Thruster Breathing Mode*, Ph.D. Thesis, Dept. of Aerospace Engineering, University of Michigan, Ann Arbor, 2010.

[72] Chiu, Y.-H., Dressler, R., Levandier, D., Houchins, C., and Ng, C., "Large-angle xenon ion scattering in Xe-propelled electrostatic thrusters: differential cross sections," *Journal of Physics D: Applied Physics*, Vol. 41, No. 165503, 2008.

[73] Scharfe, M., Private communication.

[74] Ngom, B., *Magnetic field simulation and mapping based on Zeeman-split laser-induced flourescence spectra of Xenon in the discharge channel of 5-6 kW coaxial stationary-plasma Hall thrusters*, Ph.D. Thesis, Dept. of Aerospace Engineering, University of Michigan, Ann Arbor, 2009.

[75] Shastry, R., *Experimental Characterization of the Near-Wall Region in Hall Thrusters and its Effects on Performance and Lifetime*, Ph.D. Thesis, Dept. of Aerospace Engineering, University of Michigan, Ann Arbor, 2011.

[76] Boyd, I. and Crofton, M., "Modeling the Plasma Plume of a Hollow Cathode," *Journal of Applied Physics*, Vol. 95, 2004, pp. 3285–3296.

[77] Hofer, R., Katz, I., Mikellides, I., Goebel, D., Jameson, K., Sullivan, R., and Johnson, L., "Efficacy of Electron Mobility Models in Hybrid-PIC Hall Thruster Simulations," *44th AIAA/ASME/SAE/ASEE Joint Propulsion Conference*, 2008, AIAA-2008-4924.

[78] Bisek, N., *Numerical Study of Plasma-Assisted Aerodynamic Control for Hypersonic Vehicles*, Ph.D. Thesis, Dept. of Aerospace Engineering, University of Michigan, Ann Arbor, 2010.